HARVARD UNIVERSITY
Graduate School of Arts and Sciences

THESIS ACCEPTANCE CERTIFICATE

The undersigned, appointed by the

Division of Engineering and Applied Sciences

Department

Committee

have examined a thesis entitled

"Imaging Coherent Electron Wave Flow in Two-Dimensional Electron Gas Nanostructures"

presented by Mark Allen Topinka

candidate for the degree of Doctor of Philosophy and hereby certify that it is worthy of acceptance.

Signature R. M. Westervelt

Typed name Professor R. Westervelt

Signature M. Tinkham

Typed name Professor M. Tinkham

Signature Frans Spaepen

Typed name Professor F. Spaepen

Signature Eric J. Heller

Typed name Professor E. Heller

Date December 18, 2001

Imaging Coherent Electron Wave Flow Through 2-D Electron Gas Nanostructures

A thesis presented

by

Mark Allen Topinka

to

The Division of Engineering and Applied Science

in partial fulfillment of the requirements

for the degree of

Doctor of Philosophy

in the subject of

Applied Physics

Harvard University

Cambridge, Massachusetts

January 2002

UMI Number: 3038491

ProQuest Information and Learning Company
300 North Zeeb Road
P.O. Box 1346
Ann Arbor, MI 48106-1346

Imaging Coherent Electron Wave Flow Through 2-D Electron Gas Nanostructures

Advisor: Prof. Robert M. Westervelt **Author: Mark Allen Topinka**

Abstract

This thesis presents the first published spatial images showing coherent electron flow through quantum point contacts (QPCs). The QPCs are defined in a high-mobility two-dimensional electron gas (2DEG) existing in a GaAs/$Al_{.3}Ga_{.7}As$ heterostructure. The images of electron flow were obtained using a new technique in which high-speed, low-noise transport measurements are taken at the same time that a charged atomic force microscope (AFM) tip is scanned or positioned directly above the 2DEG. The AFM tip creates a movable depletion disc in the 2DEG which can backscatter electron waves and hence change the conductance of the QPC (or other nanostructure device) when it is positioned in an area of high electron flow. By raster scanning the AFM tip and simultaneously monitoring the conductance of the device, an image of electron flow can be compiled.

The first series of measurements examines the angular current patterns for electron flow through the lowest transverse modes of a QPC. Very good agreement between theory and experiment is found - the number of lobes in the electron flow patterns are found to be equal to the mode number. Coherent interference fringes spaced by half the Fermi wavelength, λ_F, decorate the images of flow and can be blurred out by using high drain-source bias voltages, leaving behind the envelope of electron flow. The use of the

AFM tip as a positionable artificial impurity is also investigated, whereby it can selectively suppress individual conductance plateaus.

A second series of measurements reveals surprising features in electron flow from a quantum point contact at distances greater than about 500nm. The electron flow is found to develop strong branches which split and bend, but which remain narrow throughout the entire scan range. This unexpected feature of the flow has since been investigated theoretically by our collaborators and has been found to be due to the cumulative effects of many small angle scattering events - the branches are related to caustics which form downstream of focussing dips in the potential. Another surprising feature is found in this series of measurements - coherent fringes are found to persist throughout the entire scan range.

Table of Contents

Acknowledgements

I would like to thank, first and foremost, Bob Westervelt, for providing me a fantastic lab to work in, for recruiting an equally fantastic group of fellow students to journey through graduate school with, and for coming up with an wonderful project and many experimental suggestions and ideas both before and during my time here that have helped fuel my flight. Bob has struck a really good balance between giving me the freedom and space to make my own decisions (and learn from my own mistakes), and being there with advice and guidance when it was needed.

I would also like to thank the other members of my committee, Franz Spaepen, Michael Tinkham, and Rick Heller, for their interest in my research and for many helpful discussions and suggestions along the way. I would especially like to acknowledge how nice it has been to collaborate with Rick Heller and his group on a number of papers and research projects during the past few years. The high quantity and quality of communication that has existed between our two groups and the discussions I have had with Rick during my time here have deeply enriched my experience in graduate school.

I'm happy to have gotten to know and worked with the many other graduate students in Bob's lab who have overlapped with me during my time at Harvard. Without exception everyone in Bob's lab during my tenure has been smart, helpful, friendly, and fun to hang out with- it's hard to imagine asking for much more. My first few years in the lab were spent working with Marc Eriksson on the AFM. I very much appreciate and am impressed with the pioneering work he did in starting with an empty room and designing and setting up a first working low-T AFM in our lab, and I am grateful for his

patient, skillful mentorship during that time. Jordan Katine, Aram Adourian, Catherine Crouch, and Junmin Hu all helped to make my first years in the lab an enriching and positive experience. I was sad to see them go in a "stimulated emission" of graduate students during and after my second summer, but I was happy that many of them stayed around Boston for many years after that[1]. Carol Livermore and Rex Beck, both a year ahead of me, were great to work with as well, and were a lot of fun to chat with about quantum dots, FET-cantilevers, and all other things mesoscopic. It was great to get to know Carol and to have her as a member of the lab- a very good, patient, and engaged teacher, and an independent and bold experimentalist. She paved the road to more automated data collection in the Westervelt lab with her "fast data collector" that I have continued upon, and I was happy when she to stuck around Boston after graduation. I also enjoyed getting to know and working with Rex- I remember our collaboration on his scanned FET cantilevers and our times rooming together at APS conferences fondly and I wish him well.

The students I've seen join (and in some cases graduate from) the group have been equally central to my experience at Harvard. David Duncan and Marija Drndic both came to the lab a year after me, and we started our time together by sharing many late night problem sessions over Solid State Theory or E&M, and continued with many great conversations in lab about just about anything and everything. Marija occasionally disappeared into the depths of Jefferson or the Rues de Paris during her atom-bouncing days, but I was always happy to see her back in McKay- her addition just made the lab a fun-

---

1.Jordan left for Cornell, but we were to meet again at a later date at IBM Almaden when he had the kindness not to pay back my rookie-mistake of asking him a tough question in his oral exam.

nier and funner place to be, and her fresh perspectives, questions, and insights on the physics we dealt with were always a breath of fresh air. I had a great time working with David as well- I enjoyed my vicarious dilution-fridge experimenting with him on several of occasions, and I remember fondly the many conversations we had on subjects ranging from the details of Aharonov-Bohm in open cavities to the meaning of life (some conversations resulted in more conclusions than others). Lester Chen has been a pleasure to work and play with as well- I've been impressed and even, dare I say, positively influences by his organizational skills, and it's been fun talking physics, playing basketball, collaborating with, and otherwise getting to know him.

I've had the pleasure of working with a number of younger students on the AFM project during my time in Bob's lab as well. Brian LeRoy joined the group and the AFM project several years ago, and has been wonderful to work with and a lot of fun to get to know. It has been great to have somebody with a common interest in the details of the experiment to share both the agony of defeat (early on[2]), and thankfully more recently, the thrill of victory. Brian has been a great addition to both the lab and to the AFM project, and through his steady, hard work and strong and thoughtful experimental instincts, has contributed immensely to the success of the experiment. It has been a pleasure working with him, and I look forward to seeing what directions he takes the experiment in from here. More recently, Ania Bleszynski has joined the project, and I've had a great time getting to know her- talking about both physics and politics, getting beat at basketball, borrowing her Student Advantage card for trips to The Wrap. I also want to

2. Our first summer working together set several world-records for equipment breakage and freak experiment behavior. Fortunately we found the problem at the end of that summer and promptly disposed of the Pikachu toy that had been wreaking so much havoc on our experiment.

mention that I've really enjoyed her most excellent and insightful questions about the experiment, 2DEGs, QPCs, and quantum mechanical coherence, which have sparked great discussions and learning experiences for all of us. This past year Kathy Aidala has joined the lab and is currently working on the AFM project as well- I've enjoyed getting to know her and wish her luck with her future work in the lab.

There are also a number of students who have joined the lab in other projects since my start and who are still carrying on the excellent Westerveltian tradition - I wish all of them the best of luck during the rest of their time here. Ian Chan joined the lab after we had been hearing great things about him for a year from Bob and Charlie while he was in Singapore, and he's now become the lab expert in lithography, dilution-fridges, and he might share the title for electronics acumen- it's been great to have him around. Chungsok Lee done a great job pushing the electromagnets experiment into new territory, and has been a friendly and energetic addition to the lab and an invaluable addition to the Westervelt basketball dynasty. Hak-Ho Lee has been great to have around as well, and I've really enjoyed his contributions to discussions in the group as well as the especially memorable group talks he has given[3]. Parisa Fallahi joined the group last year and it has been really nice talking with and getting to know her- whether our conversation were about activism and politics or quantum mechanics and computation, they were always interesting (and often late at night). I've also enjoyed our occasional bike / car races down Kirkland Ave (which I always won, by the way). It is with great hesitance (ask my labmates!) that I finally leave the lab and all these fantastic people behind, but I

3.including a micro-computer controlled project which was able to read and display local weather information off the web, and another which accidentally measured the resistance through my hand by the changing the rate of blinking of two red LEDs

wish them all the best and I look forward to seeing them on future trips to Boston and at future physics conferences.

Many other friendly faces around McKay have made it a pleasure to come in to work each morning (or afternoon, as the case may be). All the Tinkhamites- Dolores Bozovic, Jeanie Lau, Marc Bockroth, Nina Markovic, Steve Shepard, as well as the old guard- Drago Davidovic, Alexey Bezryadin, Joe Oswald, and Sarah Pohlen, have really made the 2nd Floor what it is- an active, vibrant research center as well as a friendly, welcoming place to work. Steve Shepard has done a fantastic job of managing and running the cleanroom and has offered valuable advice, instruction, and tips on many occasions. Another group of people who I've really appreciated having around and enjoyed getting to know has been Charlie Marcus and his group - Sarah Cronenwett, Dominik Zumbuhl, Ron Potok, Leonardo Di Carlo, Josh Folk, Heather Lynch, Jeff Miller, Alex Johnson - they arrived just about two years ago, and gave the mesoscopics community at Harvard one sudden huge infusion of energy and cheer.

I would also like to acknowledge a number of other people outside the lab in the Harvard Physics Department and the Division of Engineering and Applied Sciences. Susan Wieczorek has been helpful and patient and has managed to keep a sense of humor about my many deadline and progress report transgressions. Ralph Generazzo in the purchasing department runs a simultaneously tight and friendly ship. Tomas Rosado is great to have running the stockroom downstairs, and I've enjoyed the Manchego and guava paste delicacy he clued me into. It's been nice to have David Lovler as a part of the lab the past few years - always friendly and helpful, he has done a good job in his part of keeping the lab a well oiled machine, and I'm still working on a multiple choice logic

puzzle he gave me a couple of years ago. Yuan Lu has done a good job of keeping the SEMs running smoothly, and often goes above and beyond the call of duty, coming in many Saturdays and Sundays to change burnt-out filaments. Bob Graham, in addition to being a mean volleyball player, has kept the entire Laboratory humming along at a very healthy level.

My friends deserve a huge chunk of credit for my making it through graduate school in one piece, and moreover, for helping me to enjoy myself and grow not just as a physicist but as a person during my time here. I've known Lisa Lawrence from my very first days here at Harvard, and I am very grateful for all the great times together, and for the support, friendship, and growth we've shared during our time here. Melora Crooker was another rock-solid friend for me while I was here- I'm grateful for her knack for listening and her amazingly good advice on just about everything, and for being a great friend. Oh, and for her having the world's cutest puppy. My conscripted apartment mates, Sahr Conway-Lanz, Dan Fitzgerald, and Jonathan Conant were wonderful to live with, Settle with, cross-country ski with, quote Star Wars with, clean coins with, and generally hang-out with during my last few months of thesis work. Fellow physicists Jonathan Weinstein, Dolores Bozovic, and Paul Evans have been good friends and lots of fun to share trips to Maine with, play Myth II against, battle problem set with, live in the dorms with, and explore Harvard and Boston with. John Davis is a great friend, (even if he did usually beat me at Twisted Metal 2 or whiffle baseball), and having him around Boston for the first half of my Ph.D. program was wonderful- I look forward to hopefully seeing him more now that we're both on the same coast again. Another friend I look forward to seeing more of on the West coast is Kehl Sink, who has been great to

visit and talk with over the past many years, and has been the mastermind for several fantastic trips during and before graduate school. I also feel very grateful to have gotten to be friends with David Goldhaber-Gordon towards the end of my time at Harvard, and I'm looking forward to hanging out with and working with him out at Stanford. Finally, it's been really amazing and wonderful getting to know Ishani L. Maitra here at the very tail end of my stay in Cambridge- thanks for giving me a very strong reason to come back and visit... often!

Finally, I would like to thank my family - my mom, my dad, and my brother, Rick. Their unconditional love and support has made all the difference. None of this would have been possible without you. I would like my mom and dad to know that all the time, energy, caring, and love that they have unselfishly poured into me during my childhood and since has allowed me to become who I am. My younger brother, Rick, has been a source of strength, perspective, and wisdom at many times- I am really grateful to have a brother with his independent outlook, his spirit of adventure, and his sense of humor.

Good luck to everyone I've mentioned here and to a thousand I haven't! I wish you all well and hope our paths will cross many times in the coming years.

Chapter 1

Introduction

1.1 Overview

Two dimensional electron gasses (2DEGs) and nanostructures fabricated in them have formed an exciting and dynamic area of research over the course of the past two decades[1,2]. Developments in two distinct sets of technologies - molecular beam epitaxy (MBE) and microfabrication - have allowed this to occur. MBE has allowed researchers to tailor the atomic structure of a crystal in one growth dimension with nearly single atomic-layer precision and to create designer crystals such as the high-mobility GaAs/$Al_xGa_{1-x}As$ 2DEG heterostructure shown in Figure 1.1[3]. These 2DEG heterostructures contain a quasi 2-D sheet of electrons at the buried

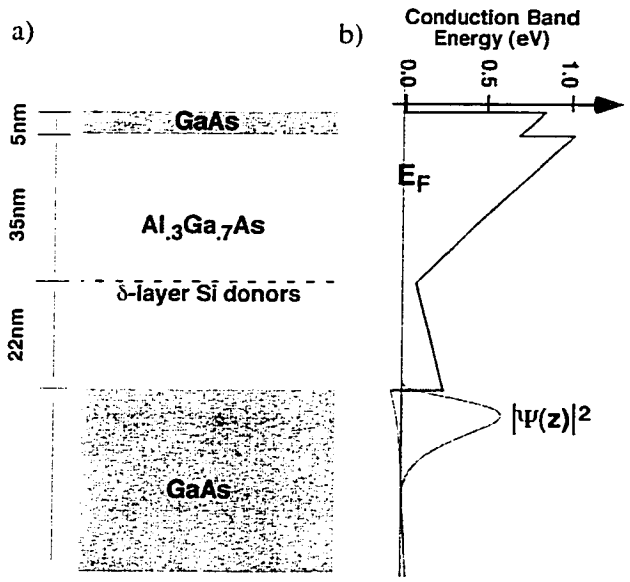

Figure 1.1 shows the 2DEG heterostructure used in our experiments and the resulting energy band diagram. (a) shows the material layers and dimensions of our heterostructure. (b) shows the conduction band edge and the resulting z-wavefunction for every electron in the 2DEG.

---

1. C. W. J. Beenakker, H. van Houten (1991). "Quantum Transport in semiconductor nanostructures," in *Solid State Physics* **44**, H. Ehrenreich and D. Turnbull, eds., Academic Press, San Diego.

2. L. L. Sohn, L. P. Kouwenhoven, G. Schon, eds., (1997). *Mesoscopic Electron Transport*, Kluwer Academic Publishers, Dordrecht, The Netherlands.

3. Self consistent Schroedinger-Poisson Calculation of conduction band and $|\Psi(z)|^2$ courtesy of Henrik Bruus, personal communications.

GaAs/AlGaAs interface where electrons are confined to their lowest energy z-subband, but are able to move as free electrons in the x and y directions. At the same time that advances in MBE have allowed such crystals to be grown, microfabrication has progressed to the point where nanostructures in and on these crystals with lateral features much smaller than 100nm are now straightforward to fabricate. The convergence of these two technologies has allowed researches to create 2DEG nanostructures with reduced dimensionality, and with precisely controllable and tunable shapes and sizes.

The size of the nanostructures that can be made in these 2DEGs have dimensions of a similar order as the electron wavelength, and much smaller than the electrons' mean free path and phase coherence length. The ability to create such devices has opened up an exciting new area of research known as mesoscopic physics. This is an area at the intersection of the microscopic and the macroscopic, where the quantum wave nature of electrons is critical to understanding the electrical behavior of the nanostructures, but where important deviations from microscopic, coherent quantum mechanical behavior occur because of connections to and interactions with the leads and the environment. The field of mesoscopics has exploded since with the advent of the advanced MBE and microfabrication techniques described in the paragraph above.

The amount of research using GaAs/$Al_xGa_{1-x}As$ two dimensional electron gasses (2DEGs) and nanostructures in the past two decade is impressive. Nobel prizes were awarded in 1985 for the discovery of the quantum Hall effect[4], and in 1999 for the fractional quantum Hall effect[5]. Nanostructures patterned in 2DEGs have been the subject

---

4. K. Von Klitzing, G. Dorda, M. Pepper, *Phys. Rev. Lett.* **45**, 494 (1980)

5. D. C. Tsui, H. L. Stormer, A. C. Gossard, *Phys. Rev. Lett.* **48**, 1559 (1982)

of intense investigation ever since the experimental discovery in 1988 of quantized conductance in quantum point contacts (QPCs)[6,7]. That discovery helped launch an explosion of research in 2DEG nanostructures and mesoscopic physics which continues to this day. Research based on 2DEG nanostructures in the past decade includes an incredible range of work. Investigations involving quantum dots alone have led to many experimental and theoretical discoveries: Coulumb blockade and single electron transistors[2,8], Kondo physics in dots[9,10], dots as highly sensitive charge sensors[11], dots as adiabatic charge pumps[12], dots as tunable artificial molecules[13], spin physics in dots[14,15], quantum computation involving dots[16], to name just the tip of the iceberg. 2DEG nanostructures more open than quantum dots have been used in an equally wide array of investigations and discoveries: electron optics in 2DEGs[17], high-frequency mixers using QPCs[18], investigations into quantum chaos[19], Fabry-Perot style resonators[20], weak localization and phase coherence measurements[21,22], Hanbury Brown and Twiss-type experiments with QPCs[23], dephasing experiments with which-path detectors[24], QPC "0.7 structure"[25,26], to mention but a few. The field of 2DEG nanostructures and mesoscopic physics has been an extremely exciting and robust field over the past decade.

---

6. B. J. van Wees et al., Phys. Rev. Lett. **60**, 848 (1988)

7. D. A. Wharam et al., J. Phys. C Solid State Phys. **21**, 209 (1988)

8. reviewed in M. A. Kastner, *Physics Today* **46**, 24 (1993)

9. D. Goldhaber-Gordon et al., *Nature* **391**, 156 (1998)

10. S. M. Cronenwett, T. H. Oosterkamp, L. P. Kouwenhoven, *Science* **281**, 540 (1998)

11.Duncan, D.S.; Livermore, C.; Westervelt, R.M.; Maranowski, K.D.; Gossard, A.C. *Appl. Phys. Lett.* **74**, 1045 (1999)

12. Switkes, M.; Marcus, C.M.; Campman, K.; Gossard, A.C., *Science* **283** 1905 (1999)

13.C.Livermore, C.H.Crouch, R.M.Westervelt, K.L.Campman, A.C.Gossard, *Science* **274**, 1332 (1996)

14. Folk, J.A. et al., *Phys. Rev. Lett.* **86** 2102 (2001)

The subject of this thesis is the development of a novel scanned probe microscope (SPM) tool with which to study 2DEG nanostructures which allows the collection of detailed spatial images of coherent electron flow. Our technique combines the strengths of traditional low-noise transport measurements with the ability to collect direct 2-d spatial information about the operation of the devices under study. Transport measurements alone over the past decade have yielded a wealth of information about the physics of these devices, as evidenced in the paragraphs above, but some very fundamental questions have been difficult to address - questions such as where are the electrons flowing through these nanostructures?, and how are the details of the electron flow related to the behavior and physics of these devices? This thesis presents the developement and application of a radical new tool which allows us, for the first time, to take direct spatial images of electron flow through these devices and to begin to answer some old questions as well as ask some new ones.

15.S. Luscher et al., Phys. Rev. Lett **86** 2118 (2001)

16. Imamoglu, A.; Awschalom, D.D.; Burkard, G.; DiVincenzo, D.P.; Loss, D.; Sherwin, M.; Small, A., *Phys. Rev. Lett.* **83**, 4204 (1999)

17. Spector, J.; Stormer, H.L.; Baldwin, K.W.; Pfeiffer, L.N.; West, K.W., *Appl. Phys. Lett.* **56**, 2433 (1990).

18. Haubrich, A.G.C.; Wharam, D.A.; Kriegelstein, H.; Manus, S.; Lorke, A.; Kotthaus, J.P.; Gossard, A.C., *Appl. Phys. Lett.* **70**, 3251 (1997)

19.Marcus, C.M.; Rimberg, A.J.; Westervelt, R.M.; Hopkins, P.F.; Gossard, A.C., *Phys. Rev. Lett.* **69** 506 (1992)

20.Katine, J.A. et al., *Phys. Rev. Lett.* **79** 4806 (1997)

21.Katine, J.A.; Berry, M.J.; Westervelt, R.M.; Gossard, A.C., *Phys. Rev. B* **57**, 1698 (1998)

22.A. Yacoby, U. Sivan, C.P. Umbach, J.M. Hong, *Phys. Rev. Lett* **66**, 1938 (1991)

The system we apply our technique to in this thesis is one that is at the heart of a large fraction of 2DEG nanostructure physics - the quantum point contact (QPC) (see Figure 1.2). After the initial experimental discovery that they show conductance quantization, QPCs have been and continue to be used in myriad investigations including almost every experiment mentioned in the paragraphs above. Electron flow through QPCs has been studied both theoretically and experimentally and the fundamental origins of conductance quantization through QPCs is well understood, but many questions crucial to understanding the operation of real-world QPCs (and other nanoscale devices) remain unanswered. Because they play such a central role in the operation of mesoscopic devices, QPCs make an ideal first system to study using our new SPM techniques.

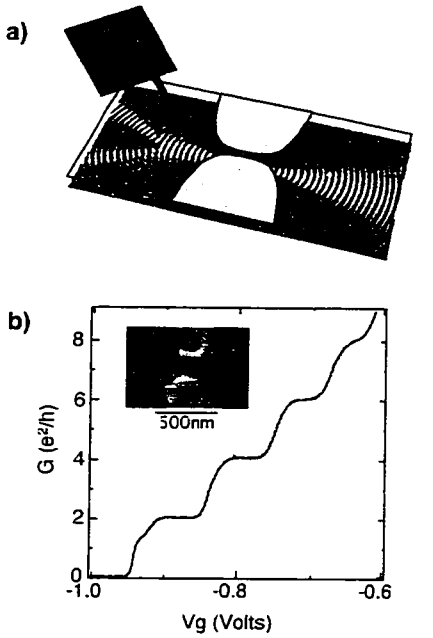

Figure 1.2 shows in (a) a schematic of the experimental setup used to image electron flow through a quantum point contact (QPC), and in (b) an experimentally measured QPC conductance trace with conductance quantization in steps of $2e^2/h$.

The basic experimental technique is shown in Figure 1.2a. A charged AFM tip is brought down over the QPC, creating a movable depletion disc in the 2DEG below. This depletion disc can backscatter electron flow through the QPC, modifying the QPC's con-

---

23.W.D.; Kim, J.; Liu, R.C.; Yamamoto, Y., Science 284, 299 (1999)

24.E.Buks, R.Schuster, M.Heiblum, D.Mahalu, V.Umansky, *Nature* **391**, 871 (1998)

25. A. Kristensen, et al., *Phys. Rev. B* **62**, 10950 (2000)

26.S. Cronenwett, et al., submitted to Science October 2001.

ductance. When the tip (and its depletion disc) are placed so as to block flow coming from the QPC, a relatively large change in conductance through the QPC will be measured. Conversely, when the tip is placed over an area where little current is flowing, it will have a correspondingly small effect on the QPC's conductance. By raster scanning the tip and simultaneously measuring the conductance through the QPC we can compile an image showing the electron flow pattern from the QPC.

A number of interesting, important, and often surprising facts about electron flow from a QPC were successfully measured using this technique. Figure 1.3 shows both theoretically calculated and experimentally measured flow through the third mode of a QPC.

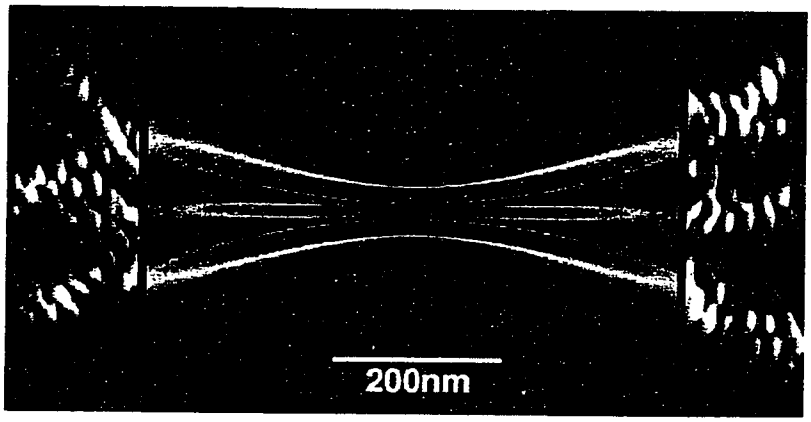

Figure 1.3 shows theoretical and experimentally measured electron flow patterns through the 3rd mode of a quantum point contact. The central region shows the gates (gray) and the theoretical flow (black indicates low flow regions, color corresponds to higher flow). The far left and right are actual experimental images of electron flow from the third mode of the QPC.

Excellent agreement between theory[27] and experiment can be seen in Figure 1.3. We confirm the theoretical prediction that flow through the Nth mode should in general contain N lobes of current flow. Three main lobes of electron flow can be seen on both sides

27. Theoretical calculation performed by Scot Shaw in Prof. Eric Heller's group.

of the QPC in this figure. Coherent fringes spaced by $\lambda_F/2$ decorate the experimental image of flow and confirm that we are imaging coherent quantum mechanical electron wave flow. Modal structure such as that seen in Figure 1.3 and other features of electron flow close to a QPC are the subject of Chapter 4.

Several very surprising features of the electron flow from a quantum point contact (QPC) were found when we looked further away from the QPC. Figure 1.4 shows an experimental image of flow from a QPC biased on the first conductance plateau.

Figure 1.4 shows electron flow through the 1st mode ($G = 2e^2/h$) of a QPC. The electron flow is constrained to a surprisingly narrow branch throughout the entire scan range, and coherent fringes decorate the flow out to the edge of the scan. The QPC gates and channel are located approximately 300nm to the left of this scan.

This image dramatically shows a very interesting and unexpected feature of electron flow from a QPC that was discovered in the course of these experiments- rather than spreading out into a smooth fan far from the QPC, the flow forms into narrow branches which stay surprisingly strong and narrow throughout the entire scan range. This was studied theoretically by Prof. Eric Heller's group, and an unexpected and elegant explanation was found. These branches are the results of classical electron trajectories forming caustics as they pass over many bumps and dips in the potential. These branches as well as other

features of the images of electron flow for distances between 1μm and 4μm from the QPC are the subject of Chapter 5.

1.2 Contents of the Thesis

The first half of this thesis (chapters 2 and 3) concentrates on the development and investigation of a new low-temperature scanned probe microscope (SPM) tool for the study of nanostructures. The second half of this thesis (chapters 4 and 5) presents results from applying this new tool to one of the central devices in 2DEG mesoscopic physics, the quantum point contact (QPC).

Chapter 2 presents a description of the elements that have gone in to making the experiment work. An overview of the entire experimental apparatus is presented, starting with a picture of the entire room containing the experiment and zooming in step by step down to the heart of the experiment, the atomic force microscope. After this overview, details of a number of important subsections are given including the cryogenics necessary to reliably cool the sample to 1.7K, vibration isolation techniques, control electronics, and details about the control software which was written to manage the experiment. An additional section details advanced cryogenic AFM techniques developed in the course of completing this work, and a last section details special lithographic techniques used in preparing samples.

Chapter 3 provides details of how the experimental technique we have developed to image coherent electron flow actually works. Electrostatic calculations were performed using a home-written 3-d Poisson solver in order to better understand the perturbation our tip was introducing to the 2DEG. Measurements were then performed to

experimentally measure the actual perturbation from the tip. Comparison between theoretical and measured tip perturbations shows excellent agreement, indicating that our simple model for understanding the effects of our tip is accurate. Next the tip is weakly coupled to the 2DEG and is used as a movable gate. A series of measurements in this mode of operation demonstrates a surprising resilience of conductance quantization in a QPC against non-depleting perturbations. In the final section of this chapter, the tip is strongly coupled to the 2DEG and the first images of electron flow are taken. Explanations for how our technique achieves a higher resolution than might be at first expected are included in this final section.

Chapter 4 discusses what we have discovered about electron flow from a QPC close in to the QPC. All the images presented in this chapter were taken within about 400nm of the QPC. In this region the flow through the Nth mode is found to have N main lobes, in good agreement with theory (see Figure 1.3). The appearance of coherent quantum mechanical fringes spaced by $\lambda_F/2$ is discussed and the fact that they can be washed out by applying a large drain-source bias is shown. Last, the use of the tip as a positionable artificial impurity is demonstrated by selectively scattering different modes from the QPC.

Chapter 5 presents images showing electron flow farther from the QPC - up to 4μm away. In this region the electron flow forms unexpected narrow branches which persist throughout the entire scan range (see Figure 1.4). These branches have been investigated theoretically by Prof. Eric Heller and his group, and the understanding arrived at from that work is presented here. Next, the surprising results that the fringes observed close in to the QPC in Chapter 4 are found to persist to the edge of our scan

range is presented. Finally, several other interesting, unexpected observations made while imaging flow far from the QPC are discussed.

Chapter 6 discusses the conclusions drawn from this work and mentions several exciting possible future directions.

Chapter 2

Experimental Techniques

2.1 Chapter Overview

A number of unique experimental techniques, tricks, and tools have been developed in the process of completing these experiments. In this chapter I cover solutions to challenges uniquely associated with building a low-temperature atomic force microscope (AFM), as well as some more general experimental techniques. The first half of this chapter deals with strategies that are most relevant to the issues surrounding successfully building and operating a cryogenic AFM. Section 2.2 provides an overview and description of the entire AFM experimental apparatus. Section 2.3 details some cryogenic techniques which are critical to the design and operation of the low-temperature AFM. Section 2.4 covers AFM sound and vibration isolation strategies. Section 2.5 covers other issues that have been important to successfully building and operating the AFM including making sure the AFM tip conducts at low-temperature and being able to align to a sample both at room-T and at liquid Helium temperatures. Section 2.6 covers the electronics that were developed to run the experiment. Section 2.7 details the software package that was written to run the experiment and also to perform specialized analysis and plotting of the data. Section 2.8 explains specialized lithography techniques that I have developed and used during sample fabrication.

2.2 Experimental Overview

This section provides an overview of the experimental setup used to image coherent electron wave flow. We will start with a "zoomed-out" view of the entire apparatus, and move in one step at a time until we are focussed on the sample and AFM tip. A schematic diagram and a digital photograph showing the entire experimental setup used are shown below in Figure 2.1:

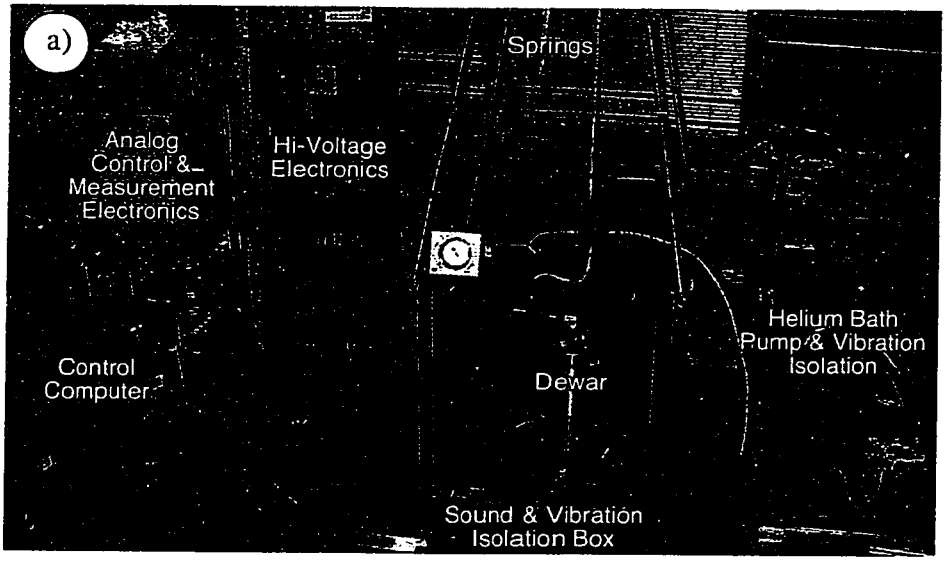

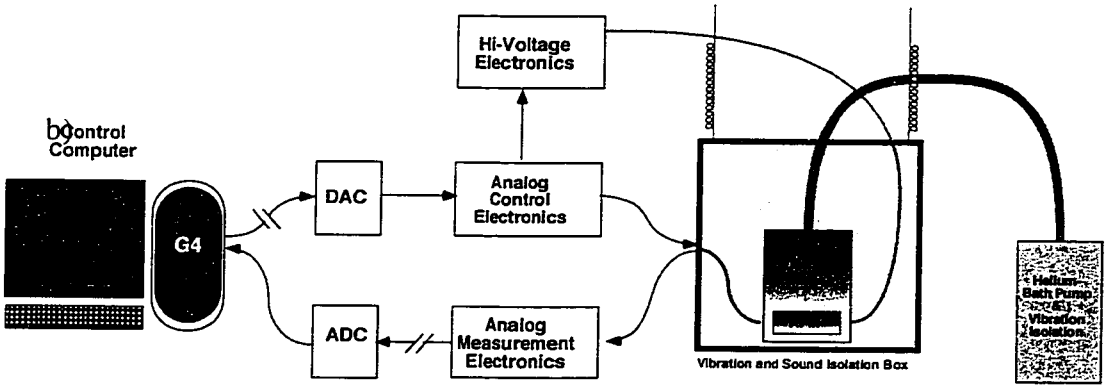

Figure 2.1a shows a photograph of the experimental setup. 2.1b shows a corresponding schematic of the setup with identically labelled components See next page for a detailed description of the setup.

The Macintosh "Control Computer" seen on the far left of Figures 2.1a & 2.1b is responsible for controlling all aspects of AFM operation as well as controlling and measuring the device being studied. A computer software package has been written for this purpose and is described in Section 2.7. The computer controls and monitors the AFM and the sample through home-built electronics, detailed in Section 2.6. The AFM itself is mounted to a cold plate inside of the vacuum space of the dewar, which is placed inside of a sound and vibration isolation box. Figure 2.2 is a close up of the dewar (containing the AFM) and the sound & vibration isolation box.

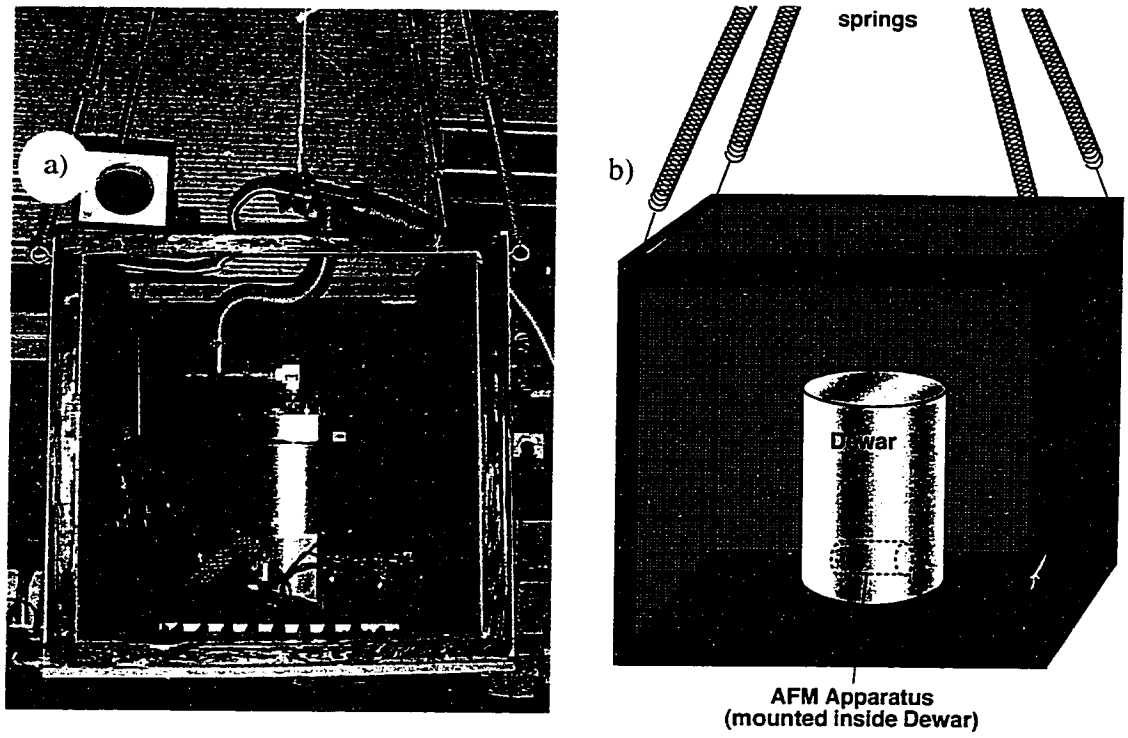

Figure 2.2 shows the vibration isolation box and cryogenic dewar. The box is about 1m x 1m x 1m, and the dewar is 0.5m tall, and 0.3m wide. Note that in actual operation the isolation box has an addition front and top lid to acoustically isolate the experiment.

The sound and vibration isolation box contains lead sheets and acoustic foam to dampen sound transmission from outside, and is hung from the ceiling by 6-foot long springs.

Previously surgical tubing was used, but was replaced by springs due to the possibility for catastrophic failure, i.e. oxidation and sudden snapping of the rubber tubing. In actual operation two additional lead and acoustic foam-lined lids are placed on the front and top of the box, further isolating the dewar and the AFM from outside vibrations and sound. A close-up of the dewar containing the AFM is shown below in Figure 2.3:

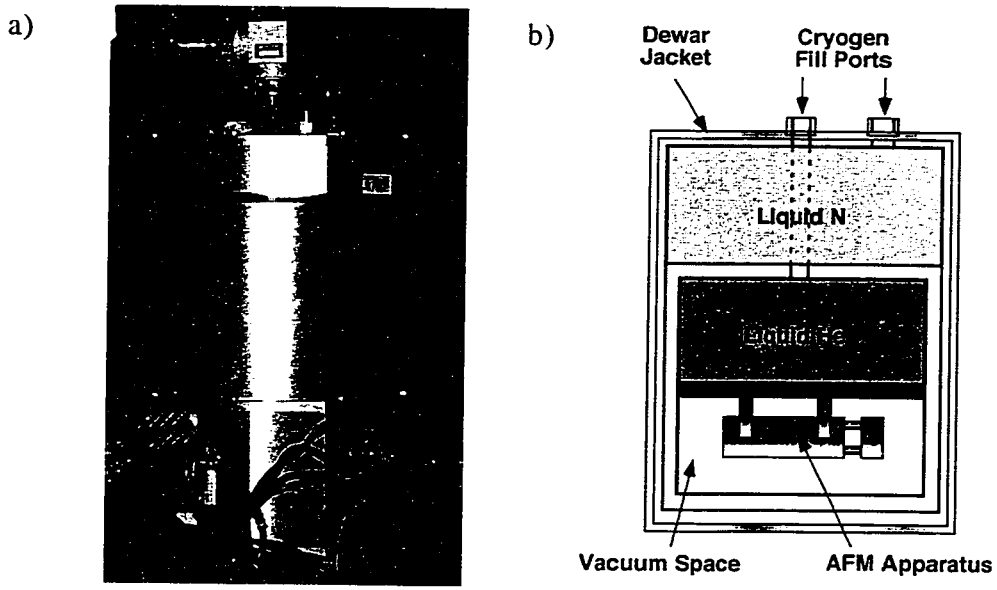

Figure 2.3 shows close-up views of the cryogenic dewar used to cool the AFM to low temperatures. (a) shows a digital photograph of the dewar resting inside the sound & vibration isolation box. (b) shows a schematic cutaway view of the insides of the dewar.

The AFM is mounted horizontally in a large vacuum space at the bottom of the dewar. The dewar is then closed up and evacuated with a turbo pump. Once a sufficiently low pressure in the vacuum space has been reached (about 10 Torr), cryogens are added to the dewar, the dewar vacuum space is valved off, and the turbo pump is disconnected (because cryopumping to the 4K and 77K shields is now more than sufficient to

maintain an extremely good vacuum). Close-up views of the AFM itself are shown below:

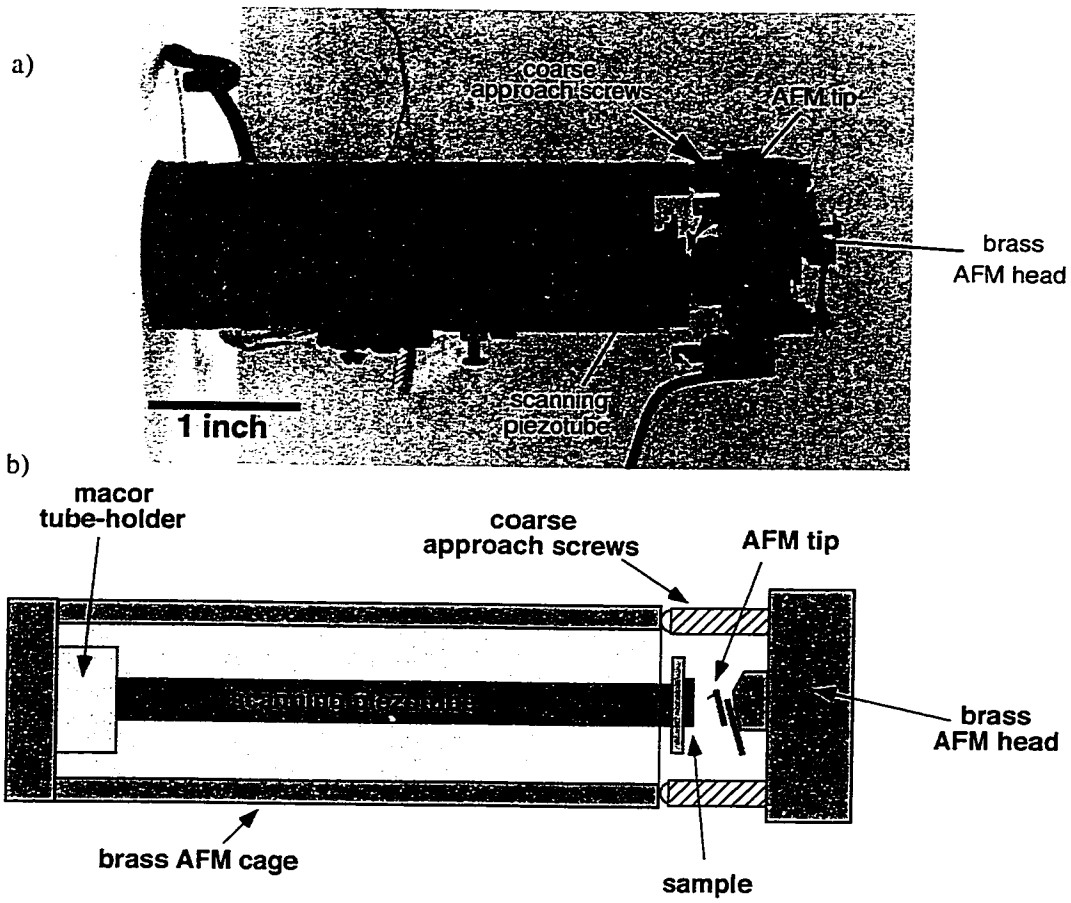

Figure 2.4 shows a cutaway sideview of the AFM itself. (a) is a digital photograph of the AFM, while (b) is a cutaway schematic showing the key pieces of the AFM. The sample is attached to the end of the piezotube which can scan in the X, Y, and Z directions. The tip is held above the sample, and the sample is scanned underneath. Coarse approach screws allow the AFM head to be adjusted to the proper Z-position at room temperature. The AFM head is held to the AFM cage by three springs (not shown in this figure).

The AFM is mounted in the vacuum space at the bottom of the dewar, and is cooled to temperatures as low as 1.7K by thermally anchoring it to the copper liquid-helium temperature base plate and pumping on the helium bath. The sample is attached to the end of a 3" long, 0.250" diam., 0.020" walled EBL#4 piezotube[1]. The tip is held to

the AFM head, which in turn is held rigidly on the AFM cage by springs. The height of the tip above the sample is adjustable by turning any one of the three coarse positioning screws (only two are shown in 2.4b). One of these three screws is accessible at low-T, and allows the tip to be moved safely away (about 0.5mm) from the surface during cooldown. Once the system stabilizes at 4.2K, the screw can then be turned via a mechanical feedthru on the dewar and the tip can be brought back into contact with the sample. The Z-coarse approach mechanism is explained in detail on page 31.

A close-up view of the top of the piezotube, sample, and tip is shown below:

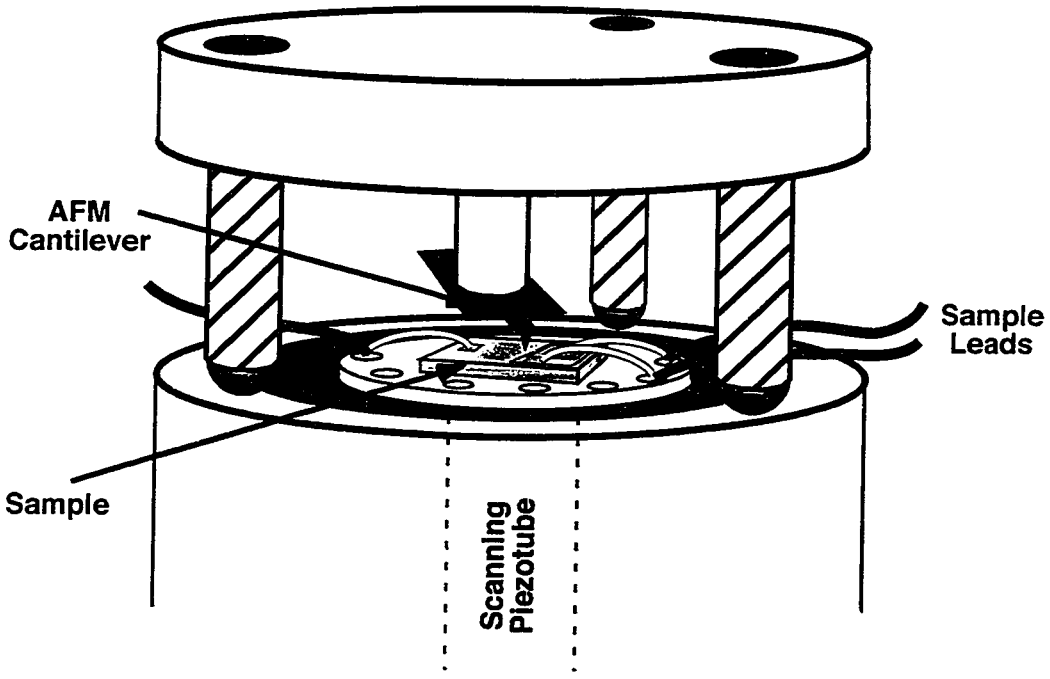

Figure 2.5 shows a schematic of a closeup view of the sample and tip.

The tip is aligned carefully at room temperature so that after cooling down to liquid helium temperatures it will be precisely aligned over the center of the device. Not shown

1. Staveley Sensors Inc., East Hartford, CT. 1-860-289-5428

in Figure 2.5 is a ground plane shield which caps the top of the piezo tube and is used to ensure that the high electric fields inside of the AFM cage (that go to the piezotube) do not reach the sample or sample leads.

Finally, Figure 2.6 shows a close-up of the tip positioned above a quantum point contact (QPC) sample, which is attached to the end of the piezotube.

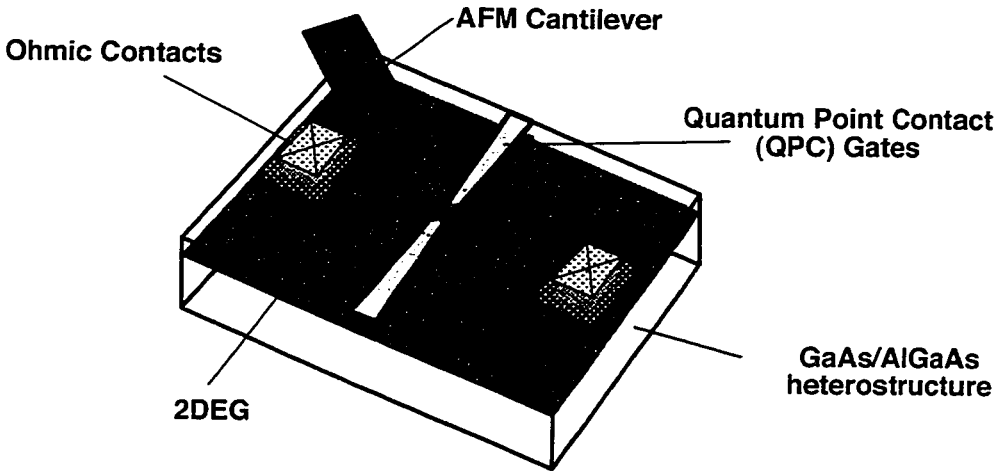

Figure 2.6 shows a closeup of a quantum point contact (QPC) and a negatively charged conducting AFM tip positioned directly in front of the QPC. A small depletion disc in the two-dimensional electron gas can be seen directly beneath the AFM tip.

The gates and ohmic contacts are connected by wirebonds to sample leads attached to the sample holder (see Figure 2.22 on page 34). In normal data taking operation the sample is then raster scanned beneath the tip while the conductance between the two ohmic contacts is monitored as a function of tip position. Chapter 3 details the techniques used for data collection.

2.3 Cryogenics

A number of cryogenic techniques have helped make this experiment a success. In this section I will discuss the key advances which have allowed a long liquid-He hold

time and a low base temperature. Through the use of these techniques, the Helium hold time is roughly 15 hours, and the base temperature of the system is about 1.7K, only 0.2K above the temperature of the liquid helium bath, inferred from its pressure. Before the implementation of the following cryogenics techniques it was doubtful that the sample was ever able to reach 4.2K[2].

Heat Shielding

Figure 2.7 shows the heat shield setup used in our dewar. The dewar has a liquid-N_2 and a liquid-He shield as well as an additional inner liquid-He temperature heat shield I added in order to improve the base temperature of the sample. Shielding the sample from radiation is especially important in two-dimensional electron gas (2DEG) experiments because of the poor electron-lattice cou-

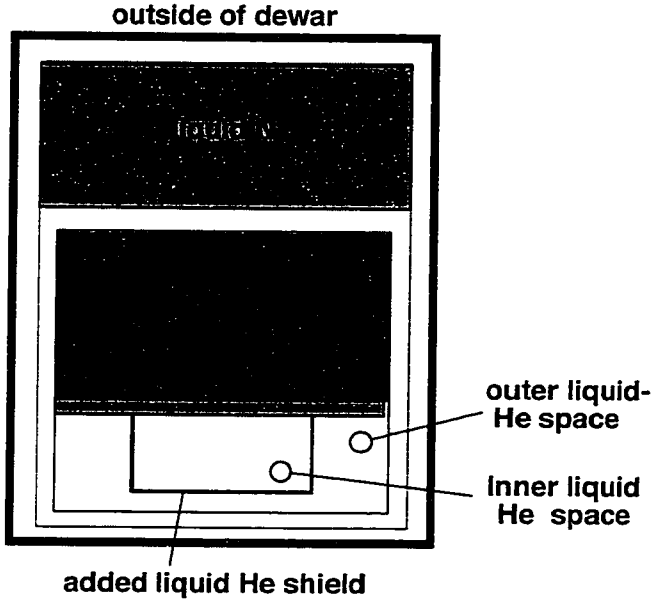

Figure 2.7 shows the basic layout of the dewar, with an emphasis on the radiation shields used to maintain a long hold time and low base sample temperature

2.The symptoms of insufficient heat-sinking were thermal smearing in transport measurements that seemed to be greater than would be expected for 4.2K, and the fact that pumping on the liquid-He bath had no noticeable effect on these transport measurements (the apparent sample temperature did not change). The blame for this heating fell on direct heating through the leads (from room temperature), on radiation from insufficiently heat-sunk or shielded wires, or on radiation from cracks in the standard, outer helium shield

pling combined with the excellent electron-electromagnetic (EM) noise coupling. The dewar normally has one liquid-N_2 shield and one liquid-He shield. I have opted to add a second, inner liquid-He temperature shield to keep the electron temperature as low as possible. The liquid-N_2 shield absorbs the relatively high power room-T radiation. The latent heat of vaporization for liquid-N_2 is much greater than for liquid-He is (160J/l compared to 2.6J/l). Inside the liquid-N_2 shield is the standard liquid-He temperature shield. Because it is difficult with this dewar to heat sink wires to the liquid-N_2 bath and shield, the wires enter the outer liquid-He space directly from the room-T connector. All wires (cantilever, LED, sample, and thermometer wires) are heat sunk to the liquid-He base plate before continuing into the inner liquid-He space (see Heat Sinking on page 20 for more information). The coarse approach mechanical rod is heat sunk at liquid-N_2 and liquid-He temperature before entering an intermediate chamber where it connects loosely to a similarly heat sunk hex key. Pictures of the additional liquid-He temperature heat shield are shown in Figure 2.8.

Figure 2.8 Close-ups of added liquid-He Shield. This shield surrounds the AFM and sample, and protects against stray radiation from holes in the shield, hot (room-T) wires and the hot parts of the coarse approach rod. (a) shows the box outside of the dewar. (b) shows the box with the AFM inside, but before the addition of the lid. (c) shows the copper box closed up and ready for the dewar to be closed up and cooled down. Note in (b) and (c) the dewar is flipped upside down from its operational orientation (seen in Figs 2.3 and 2.7).

Heat Sinking

In this section I describe the heat-sinking strategies used for the coarse approach rod (see also Coarse Z Approach & X,Y Positioning on page 31) and for the sample wiring.

The strategy employed to heat-sink the coarse-approach rod is illustrated in the following diagram.

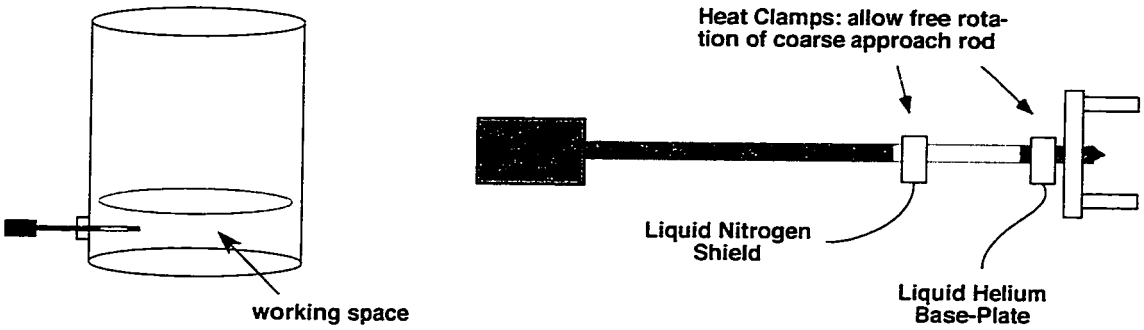

Figure 2.9 shows the heatsinking strategy used to ensure that the part of the coarse approach rod closest to the AFM and sample is cooled to base temperate.

It is important to both cool the end of the coarse approach rod to near the base temperature while at the same time avoiding unneccessarily high heat loads to the helium bath. To accomplish this, one heat sink to the liquid-N_2 shield is used to divert most of the heat flow from the room temperature end into the nitrogen bath. This heatsink is situated at the beginning of the thin-walled stainless steel portion of the approach rod. The thin walled portion of the rod reduces heat load. A second heat sink to the liquid-He base-plate is situated at the end of the thin-walled stainless steel portion so as to ensure that the end of the coarse approach rod which might otherwise cause radiative or conductive heating to the sample is cooled to as close to the base temperature as possible.

Heat sinking of the sample, cantilever, thermometer, and LED leads is achieved using standard techniques. The general strategy is shown below in Figure 2.10:

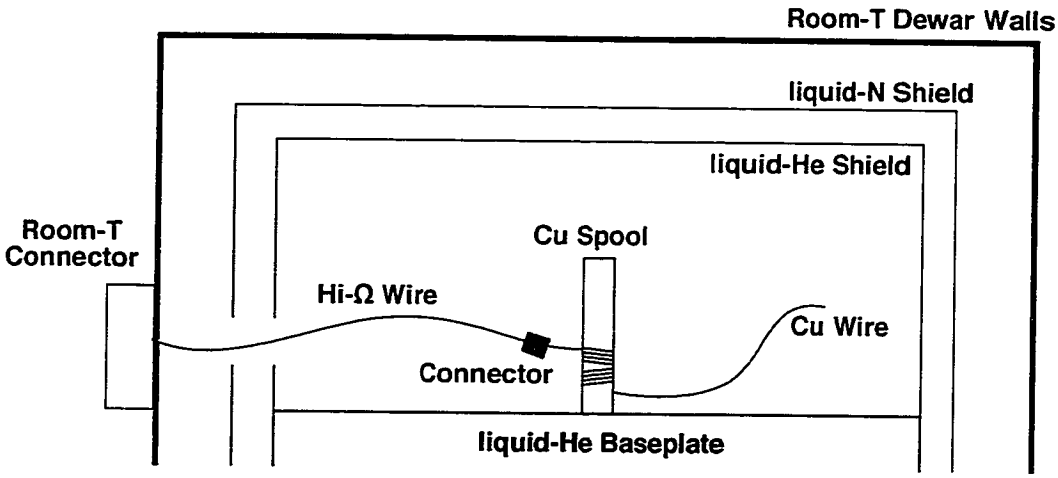

Figure 2.10 shows the general heatsinking strategy employed for sample wires, thermometry wires, and LED wires.

In order to minimize the heat leak to the helium bath from each wire, high resistance per unit length wires (R = 200Ω/ft) are used between the room-temperature connectors and the liquid-He temperature copper spools (See Figure 2.10). For historical reasons, there are two different types of high-resistance wire currently used in our apparatus. The sample leads are fine manginin wire connected to the room-T connectors and to 1.5kΩ resistors, which then in turn connect (through MicroTek connectors) to copper wires & spools. The thermometer, cantilever, and LED wiring was replaced more recently, and consists of extremely high resistance Stablohm800 twisted pair 3mil wire (from California Fine Wire Company) which has 85Ω/ft, and is made of 75% Ni, 25% Cr, 2.5% Al, and 2.5% Cu. Immediately before the copper spool are MicroTek connectors which connect the high resistance wires to thicker, low resistance (and hi-thermal conductivity) Cu wires, which then wrap around the copper spools. Copper wire provides a high heat-con-

ductivity path between the sample, cantilever, or LED and the liquid-He base plate. The thermometer is separated from the thermally conductive copper wires by an additional length of high resistance wire (not shown in) in order to allow the thermometer to measure it's surroundings rather than simply the temperature of the base plate.

The wrapping of the wires around the copper spools was done in a way which minimizes the 60Hz electromagnetic-pickup. Each wire is wrapped 5 times around the spool clockwise, and is then 5 times counter clockwise. Hence the total flux enclosed by the wire is close to zero. The wires are held onto the spool using a coating of GE varnish. Be sure that the varnish is thinned with enough toluene and xylene before using- if the GE varnish has been left open for too long it might become too thick to effectively fill in the air gaps between the wires and the copper spool. A general procedure that I've developed which works well for wrapping these spools is outlined in Figure 2.11. The "22-gauge wire posts" in Figure 2.11 are inserted (no gluing is necessary) in snug pre-drilled

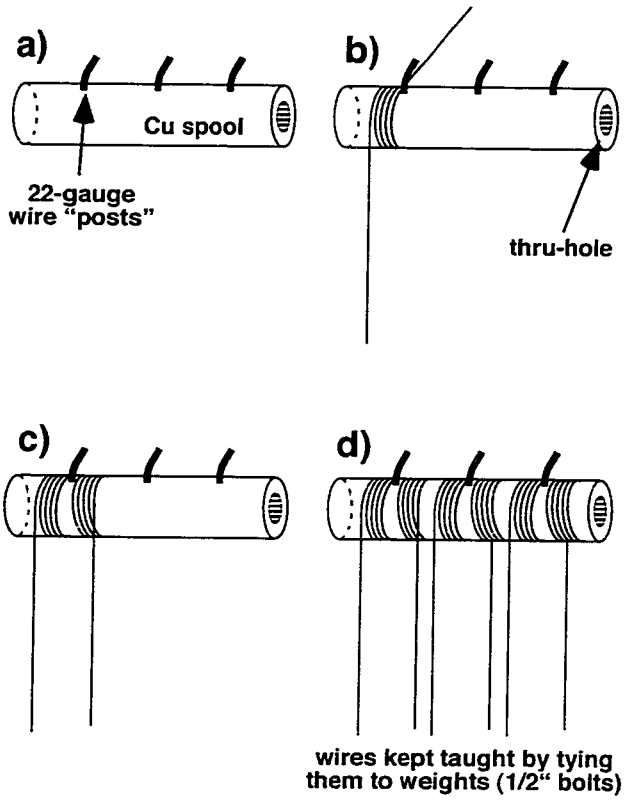

Figure 2.11 shows the general procedure for wrapping the heat-sinking copper spools with fine wire.

holes in the copper spools, and allow the reversal of wrapping direction mentioned above. The final step after 2.11d is to liberally apply GE-varnish to the entire spool and allow to dry for at least 12 hours in a warm room. It is advisable to use a respirator with an "organics" filter while completing this procedure, as toluene and xylene (two solvents contained in GE Varnish) fumes are potentially harmful. It is also worth mentioning that the choice of screw to actually bolt these heat-sink spools to the base plate is important: a brass screw should be used rather than a stainless steel screw, because a stainless steel screw will shrink less than the copper spool during cooldown, resulting in a potentially loose heatsinking spool at low temperature even if it appears to be solidly screwed down at room-T. This would be undesirable because the heat-connection to the base plate would then be quite poor[3]. One copper spool trick which we did not employ, and which might have saved us some headaches is to first wrap the copper spool in a single layer of cigarette paper (or any similar extremely porous paper), and *then* wrap the wires around the outside of this. This can help to prevent shorts between the wires and the copper spool, and indeed several of our wires have multi-MΩ shorts to the copper spool.

2.4 Vibration Isolation

Because of the high spatial resolution necessary for our images (the feature size can be smaller than 10nm in many cases, and tip-sample distances are also normally ≤10nm), it is important to minimize mechanical vibrations that could cause the piezotube and the sample attached to the end of it to vibrate relative to the AFM tip. Lateral vibra-

---

3.By the same reasoning, if washers are to be used it is preferable to use stainless steel washers rather than brass washers. (A word to the wise: many silver colored washers are actually brass with a thin chrome coating)

tions tend to blur out sharp features in the images, while longitudinal vibrations cause the tip-sample separation to become undependable, causing measurement errors and tip-crashes. Additionally, vibrations can cause triboelectric pick-up between leads inside the dewar. This is an especially important concern in our case because there are wires going to the piezotube that often carrying greater than 400V, and triboelectric pickup is directly proportional to the voltage sources involved[4].

The main sources of vibrations in our experiment are acoustic noise, building vibrations, and pump vibrations. The first two sources of vibration are greatly reduced through the use of a vibration and sound isolation box, the "blue box" in Figure 2.1. This is briefly described in the "Vibration Isolation" subsection below. Pump vibrations are reduced through the use of a cement-filled trashcan. The last significant source of vibrational noise, noise translated down the pumping lines through the diffuse He, is reduced through the use of pump line muzzles, and by nearly closing an elbow valve placed directly after the pump. These techniques are discussed in the "Pumping Line Muzzle and Valve" subsection. A third possible source of vibrations is the boiling of both the liquid-N_2 and liquid-He cryogens. The magnitude of the vibrations from these sources are not known, but they are not a limiting factor in our resolution. For this reason they will not be discussed further, although they may become factors in the upcoming He-3 system.

4.Triboelectric pickup refers to vibrations causing changes in capacitance between components, leading to voltage pickup proportional to $\Delta V\ dC/dt$.

Vibration Isolation

The first, and most easily eliminated source of vibrations is from the low frequency vibrations present in the building. It appears that either McKay Laboratory or our lab tables (or both) have a strong resonance around 12Hz, which can be clearly seen in the image taken on the right with the AFM resting directly on the tabletop. The vibrations visible in this image correspond to approximately 5nm peak to peak vibration.

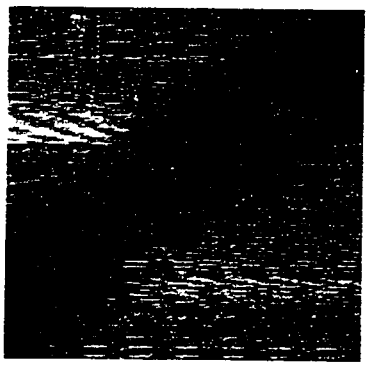

Figure 2.12 shows the effect of insufficient vibration isolation.

Because many of the electrical scans used in this experiment need to be taken with the tip held at 10nm or less above the surface, clearly these vibrations are not tolerable.

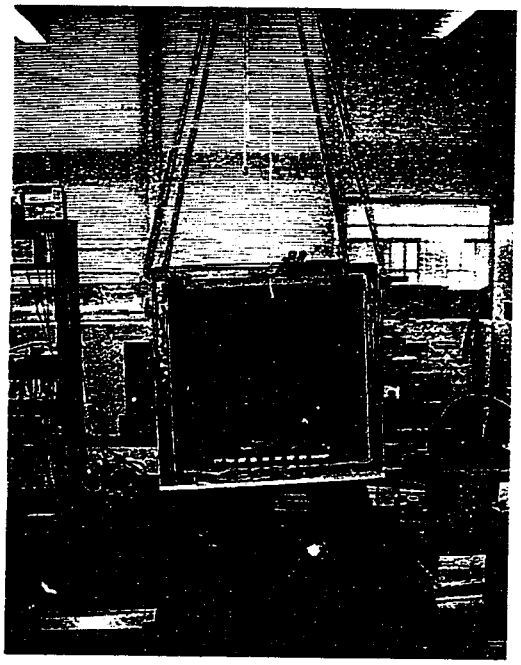

Figure 2.13 shows the sound and vibration isolation box. Note the active bio-feedback mechanism attached to bottom of box.

The solution to this problem was to place the entire experiment in a heavy lead-lined box suspended from the ceiling by long springs shown in Figure 2.13. The measured resonant frequency of this box is 0.5Hz, meaning that a 12Hz vibration in the ceiling is reduced by approximately a factor of 0.04^5. This is combined with the fact that the springs are anchored in one of the solid building supports, which in all likelihood vibrate less than a table.

Pumping Line Muzzle and Valve

A surprising additional source of vibrational noise was traced to the pump noise travelling back into the dewar through the dilute He gas inside the pumping lines. The two images to the right clearly show the symptom of this vibration: The only difference between Figure 2.14a and Figure 2.14b is that Figure 2.14b is taken without pump filters and with a completely opened pumping valve. The vibrations transmitted up the helium gas in the pumping line appear to be setting the piezotube vibrating, causing the diagonal lines.

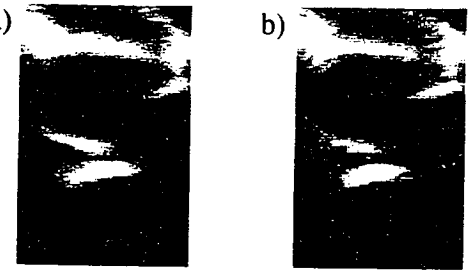

Figure 2.14 shows two closeup electron flow images, one (a) with the pump throttle almost closed and filters added, and the other (b) without.

The solution to this problem, which dampens the pump noise enough to the level seen in 2.14a, is quick and dirty, but effective. The "filters" are simply ten 1" diameter rubber test-tube stoppers and a 12"x2"x1" piece of acoustic foam placed directly into a KF-40 (40mm inner diameter) pump line. The throttled valve is simply a normal KF-40 right angle valve which has almost been closed off. The pumping speed through this acoustic "filter" seems to be slightly diminished (a base helium pressure is 7 Torr with the filter & throttled valve, and 5 Torr with no filter and a completely open valve) but this corresponds to a negligible difference in base temperature, and is well worth the removal of the vibrational noise.

5.This analysis is done assuming that the vibrational isolation system can be modelled as a 1-pole filter, which is a reasonable assumption since there is only one stage (the springs) and no active components. If this is the case, then given a driving vibration (from the building) of V_0, the vibration of the blue box and hence the AFM is $|V_{AFM}| = | V_0 \, 1/(1+i\, f/f_0) |$, where f = 12Hz and f_0 = 0.5Hz.

2.5 Advanced AFM Techniques

Making a tip conduct electrically

Developing a technique to ensure that the AFM tip conducts electrically all the way from its resistive leads to the very end of the tip was of critical importance in this experiment. The first piezolevers used (from Park Scientific, now owned by Thermomicroscopes) conducted all the way to the end of the tip at room temperature. The early experiments that Marc Eriksson, Rex Beck, and myself completed on imaging flow through a narrow constriction confirmed that these cantilevers conducted reasonably well even at low temperatures. At some point, however, something was changed in the manufacturing process which caused the tips to become very good insulators at 4K. The symptoms of this insulating nature for the tips appears obvious in hindsight. Below (Fig. 2.15) are three graphs taken with the tip held 150nm above a quantum point contact at three different "tip voltages".

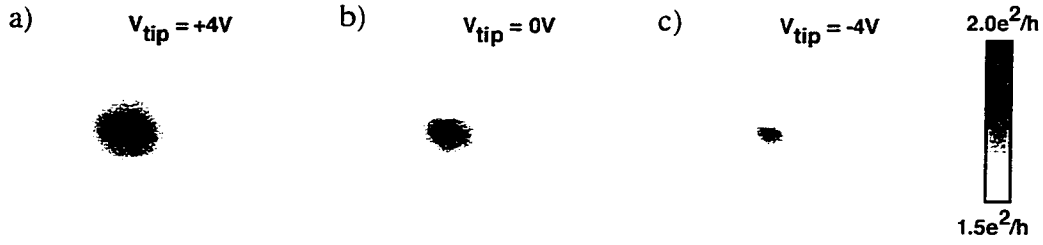

Figure 2.15 shows the symptoms of an insufficiently conducting tip.

In all these scans the tip was held at the respective voltage (+4 in a, 0 in b, and -4V in c) and scanned at 150nm above the surface over a QPC at the center of each image, (topo-

graphic image not shown). Regardless of the applied tip voltage, however, the effect of the tip was to enhance the conductance through the QPC. The pattern changes slightly, but the overall sign of the affect of the tip does not change. This observation simply does not agree with the assumption that the voltage applied reaches the end of the tip. Once a tip has been properly coated with metal the above patterns look like the following (Fig. 2.16):

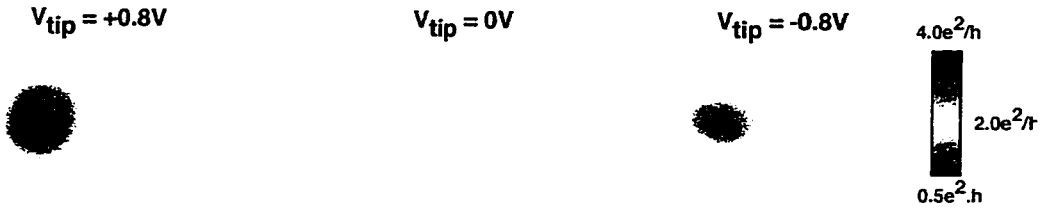

Figure 2.16 shows a similar series of scans to Figure 2.15, but here the tip has been coated with a thin layer of chrome. Now changing the sign of the voltage on the tip also changes the sign of the effect the tip has on the conductance through the QPC.

The procedure for coating the tip with metal is shown on the following page (Figure 2.17). The tip is positioned under a crude shadow mask with a everything but a small amount of the arms and the end covered. A thin layer of chrome (shown schematically in gold) is then evaporated over the exposed area.

It is important that not too much of the arms of the cantilever be evaporated onto, otherwise two bad things can happen. One is that the difference in thermal expansion between chromium and silicon can cause the cantilever to bend if too much of the cantilever arms are exposed and too much chromium is deposited. The other problem with exposing too much of the arms is that they can be shorted by the chrome layer and the cantilever deflection will not longer be detectable.

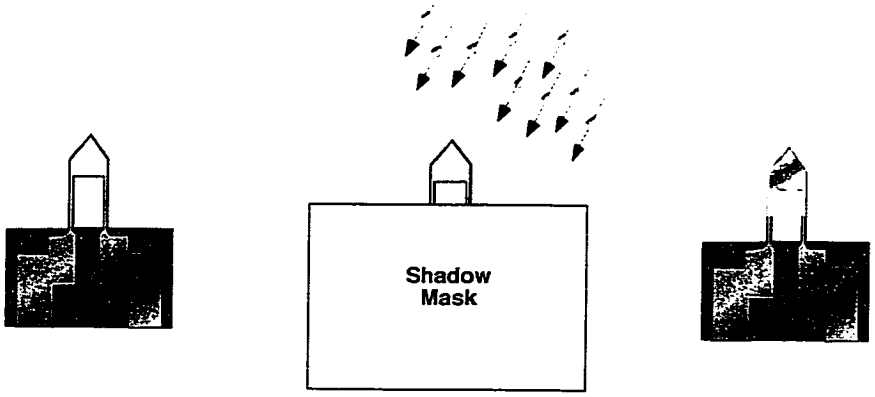

Figure 2.17 shows a schematic of a tip being metallized. The final metal coating over the end of the tip is not connected to any outside leads. It is pinned (by leakage through the oxide layer coating the entire tip) to a voltage halfway between the voltages on the two cantilever deflection detection leads (the two silver pads exiting off the bottom of the cantilever in the above drawings.

The setup used to evaporate chrome onto the AFM tip is show below in Fig. 2.18. The tip is placed facing down on a rotating sample stage in the thermal evaporator and the chrome rod is oriented at a large angle to the tip. The ideal angle ϕ is somewhere around 45°, although in practice due to space constraints in the evaporator it usually ends up being about 60°. If ϕ is too small, only the sides of the tip will be coated, while if it's too large, the tip will

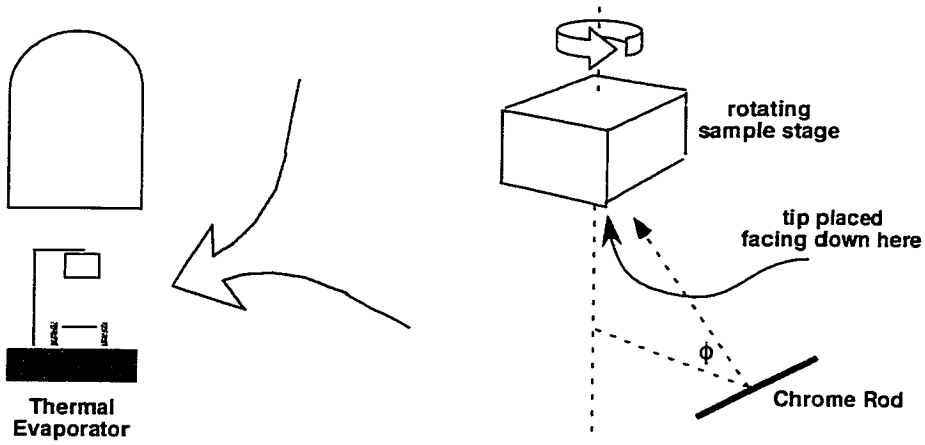

Figure 2.18 shows the basic setup used to coat tips. The tip is placed facing downwards on the bottom of the rotating sample stage.

only receive a dusting of chromium which will easily flake off. It is important that the crystal monitor have a clear line of sight to the chrome rod. Once the tip, sample holder, and rod are all properly oriented, 90Å of chrome is evaporated onto the tip while continually rotating the tip, so that all sides of the tip receive an equal amount of chromium.

It is perhaps somewhat surprising that this simple method for creating a "conducting tip" works, because there are no explicit connections between the evaporated chrome layer and the piezoresistive arms of the cantilever. One might guess that the resulting Schottky barrier would have a rather high resistance, but there is apparently more than enough leakage between the arms and the chrome layer to provide adequate electrical connection. A schematic for the final resulting cantilever is shown below:

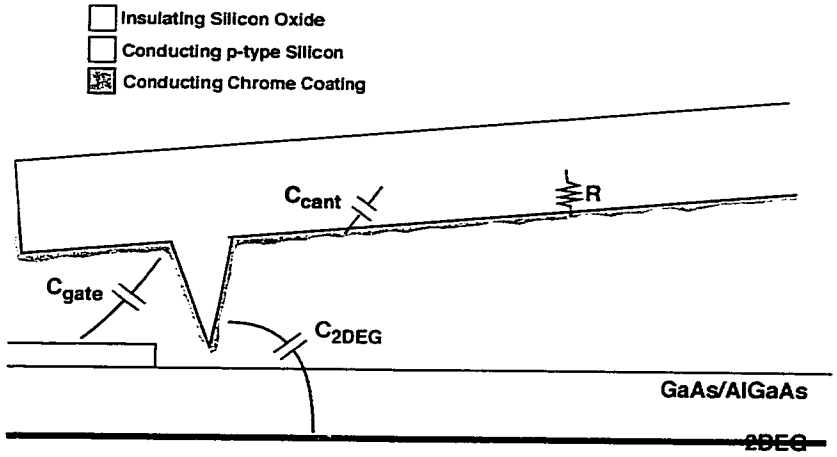

Figure 2.19 shows a schematic for the final resulting cantilever after Chrome evaporation. It is possible to arrive at an estimate for the maximum resistance between the conducting interior of the p-type Si cantilever and the Cr coating.

The main concern is that the RC time constant between the conducting interior of the p-type Si cantilever and the Cr coating will be so large that we will end up not maintaining the desired voltage on the Cr coating during the course of a scan. The capacitance

here is dominated by the capacitance between the Cr coating and the cantilever, which can be conservatively estimated at $C_{cant} \sim 2pF$ (assuming $50\mu m^2$ metallized coating, 50nm native oxide thickness, $\varepsilon=5$). Because we know that there are no observable RC time-constant effects in the time 0.1s it takes to move the tip along one scan line, we can conclude that R must be smaller than about $10^{11}\Omega$. This is not a very stringent requirement, and it seems to be easily met by leaks through dirt and defects in the insulating layer between the Cr and p-type Si.

Coarse Z Approach & X,Y Positioning

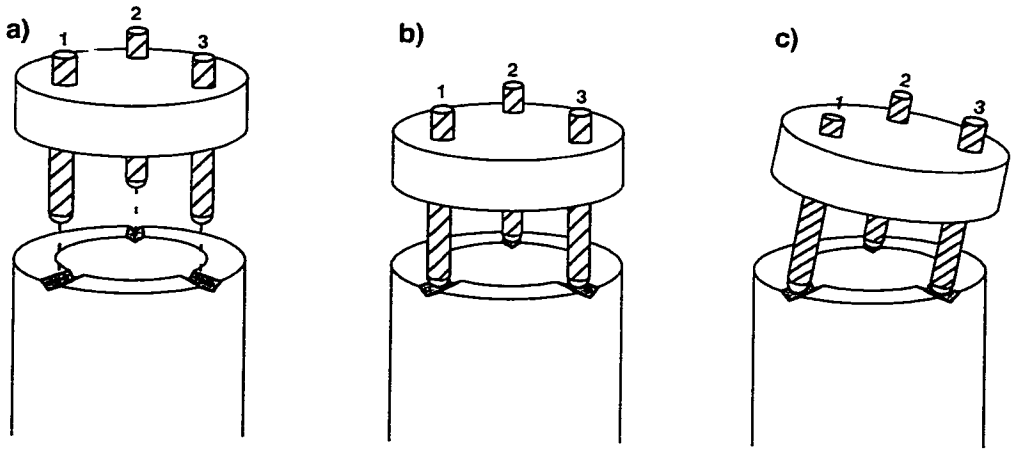

Figure 2.20 shows the coarse approach mechanism which allows the tip to be brought into and out of contact with the sample at both room-T and low-T. a) shows the AFM Head being positions above the AFM Cage. b) shows the AFM Head in place on top of the AFM Cage (fastening springs not shown). c) shows the method for coarse adjustment of Z-height.(In this figure, the tip would be farther from the sample than in b)

Because the piezotube has an extremely limited Z-range (less than 4μm at 4K), it is important to be able to perform coarse Z-positioning at both room-T and low-T. The AFM is aligned to the desired X,Y location at room-T, then the tip is lifted far off the surface (roughly 0.5mm), and the entire apparatus is cooled down. Once the system has

equilibrated at 4K, the tip is brought back into contact with the sample through the use of the coarse positioning screw. The general mechanism for accomplishing this is shown below in Figure 2.20.

The AFM Head (which holds the tip, facing down - the tip is not shown here) is first placed onto the AFM Cage (Figure 2.20b). The coarse positioning screw can then be adjusted to allow the entire AFM Head to pivot up and down, allowing several mm of adjustment in tip-height (Figure 2.20c). Screws #2 and #3 are adjustable only at room-T. Screw #1 is adjustable at both room-T and at low-T via the coarse positioning rod. The entire assembly, including the AFM Cage, the AFM Head, a hex-wrench T and a the coarse approach rod is shown in Figure 2.21

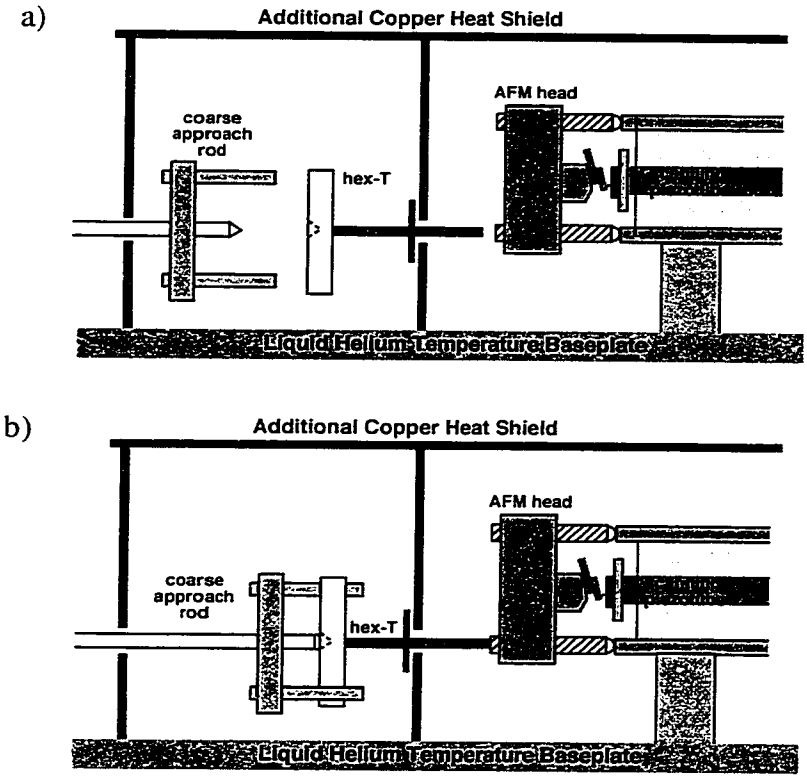

Figure 2.21 shows the entire coarse approach assembly. a) shows the assembly with the hex-T and the coarse approach rod separated for clarity. Each individually have complete rotational freedom. b) shows the assembly as it would be during an experiment.

An important improvement that was made to the AFM was the solution of the "drift problem". Previously, the process of successfully cooling down and being able to scan over a device was extremely time-consuming (weeks or sometimes even months!) and frustrating. The x-y scan range of one of our piezotube at 4K is roughly ±10μm. Aligning the sample and tip to within 10μm at room temperature is a straightforward task, but the difficulty arose because the position of the tip relative to the sample used to change by up to several hundred microns during cool down. Additionally, this shift would change by significant apparently random amounts from cool-down to cool-down. The problem was solved by several improvements to the AFM.

1) The entire AFM was remachined entirely out of one material - brass. This reduced differential thermal contraction between different pieces of the AFM, although there is still significant differential thermal contraction between the ceramic piezotube and the brass AFM cage.

2) The sample mount was redesigned so that the entire portion which holds the sample is metal (instead of the first design, which was plastic). This improves thermal contraction matching between the sample mount and the rest of the AFM apparatus. A close-up picture of the new sample mount is included below in Figure 2.22.

A side note about the sample holder: The "sample grounding connectors" are used to keep all the sample leads grounded together and attached to earth ground until the main sample connectors are safely attached to the dewar leads. In this way none of the sample gates or ohmics is ever floating to an unknown and potentially disastrous voltage, and no sudden voltage changes are applied to the sample leads during setup.

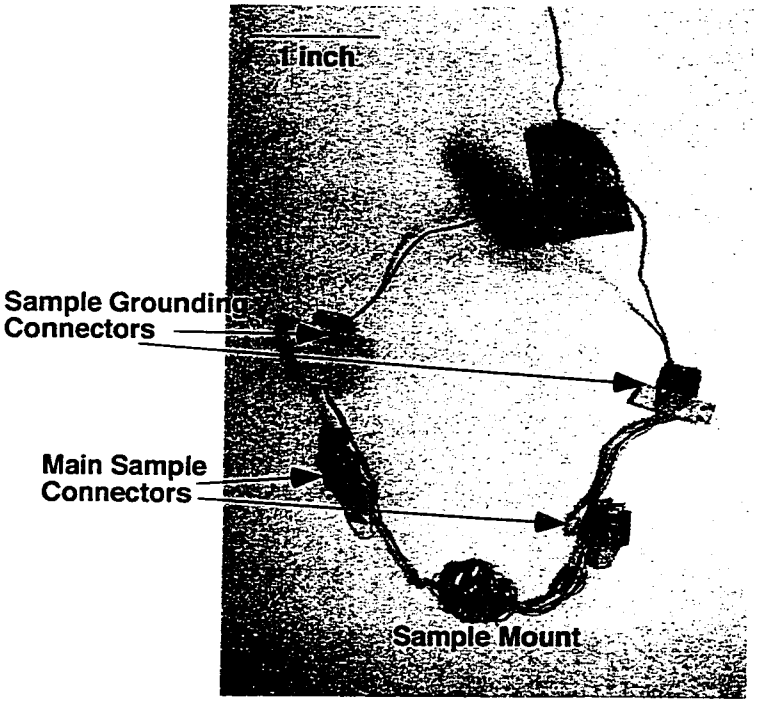

Figure 2.22 shows the sample mount used to hold samples.

3) The kinematic mount used to hold the AFM head onto the AFM cage was changed and is shown below in Figure 2.23.

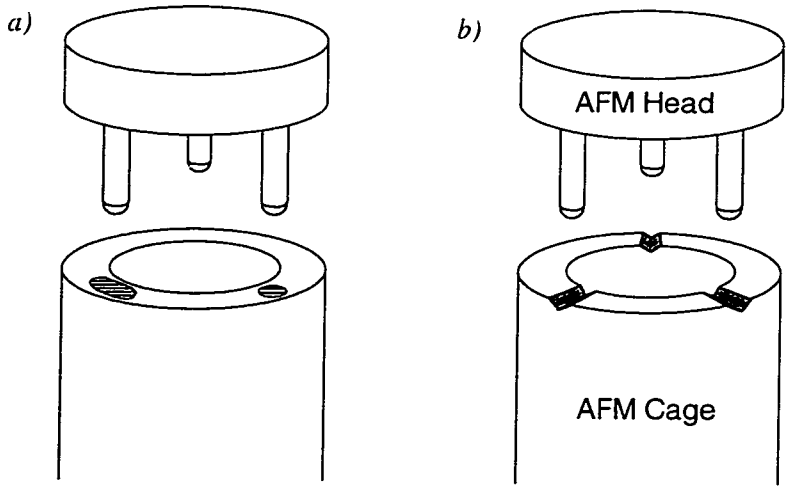

Figure 2.23 shows the old (a) and new (b) designs for the kinematic mount used for the coarse approach mechanism of the AFM. The AFM Head holds the tip, while the AFM Cage holds the scanning piezotube and sample.

Both designs successfully hold the AFM Head firmly in place (with the aid of springs, not shown) on top of the AFM Cage, but the new design offers improved resistance to any offsets from differential thermal contraction between the AFM cage and AFM head.

4) Additional spacers were added so that the pivots of the three stainless steel approach screws are precisely aligned with the plane of the sample. Incorrect alignment can lead to relatively large shifts due to differential thermal contraction. Examples of proper and improper alignment are shown below:

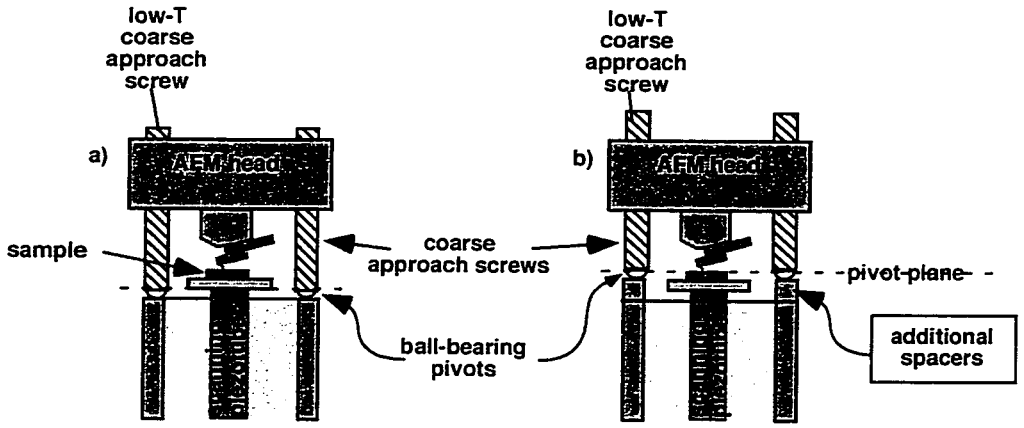

Figure 2.24 shows the improper and proper positioning of the AFM Head and coarse positioning screws. a) is incorrect, and results in very large "drifting" between room-T and low-T. b) is correct and results in little drift between room-T and low-T.

Figure 2.24a shows an problematic alignment- because the low-T coarse approach screw is moved out approximately 0.5mm during cool down, the tip rotates relative to the sample (this can result in up to 300μm shifts between room-T and low-T, making the corrective room-T offset very problematic). Fig. 2.24b shows a good working alignment - the pivot plane of the entire AFM Head (which is the plane which passes through the middle of each of the three ball-bearing pivots) lies exactly on the surface of the sample.[6]

Finding the surface

I have developed a technique to reliably locate the surface of the wafer to an accuracy better than 1nm. This is important because due to temperature drift, piezoelectric drift, and power-supply drift the height of the tip over the surface can change by as much as 10nm per hour. Usually once steady state operation is achieved (after an hour or so of warm-up time for the electronics and piezotube), the drift is considerably smaller than this, but it is often still appreciable. The following plot shows the cantilever deflection signal during the surface finding routine.

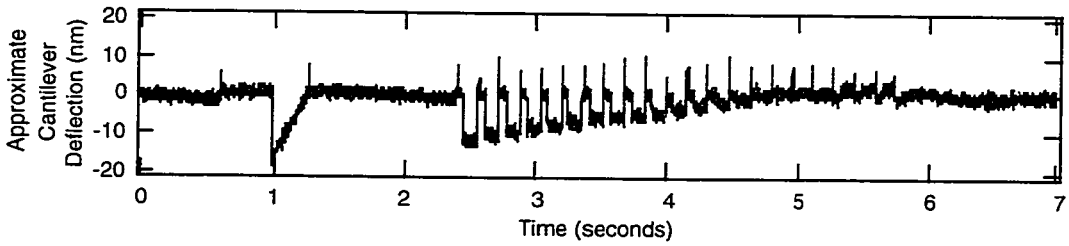

Figure 2.25 shows the measured cantilever deflection during first a coarse and then a fine surface Z determination. The coarse surface finding routine takes place from about 1.0s to 1.4s. The fine surface finding routine takes place from about 2.5s to 6s.

There are two techniques we use to find the surface. The first is a quick and dirty method which finds the surface ±3nm in about a second. This is accessed from within the program with the call "setheight". The cantilever deflection signal for this routine can be seen between about 0.6s and 1.3s in Figure 2.25. The basic procedure is as follows: 1) Pull off of surface (corresponds to the short positive spike in cantilever

6.In actuality, the best positioning is to have the plane pass 0.25mm above the sample at room-T, because it will then be 0.25mm below the sample at low-T (after an approximately 0.5mm differential contraction between the piezotube and the brass cage), resulting in no net lateral drift from this mechanism.

deflection at t = 0.6s where the cantilever is pulled downwards as it momentarily sticks to the surface). 2) Approach surface until cantilever voltage changes by more than $2*V_{cant-noise}$ ($V_{cant-noise}$ is the peak-to-peak noise in the raw cantilever signal, usually about 0.2V) (t = 1.0s). 3) Pull back until cantilever voltage just returns to un-bent value (t = 1.0s to t = 1.3s). For normal operating parameters, $2*V_{cant-noise}$ corresponds to about 7nm of cantilever deflection. Experimentally this seems to be low enough to avoid significant blunting of the tip. Due to noise on the cantilever deflection signal and hysteretic creep in the tube, this technique should not be relied on for greater than 2-3nm accuracy.

The second technique, used to position the tip more precisely once the previous technique has already been used to roughly locate the surface is accessed from the program by a call to "adjustheight". The procedure is as follows: 1) the tip must already be just barely touching the surface ±3nm. 2) a roughly 10Hz square wave is applied to the Z-piezotube, superimposed on a slowly increasing voltage (which pulls the tip slowly away from the surface). For the first half of each square wave ("T_{down}") the tip is in contact with the surface, while for the second half of each square wave ("T_{up}") the tip is out of contact with the surface. The cantilever deflection signal corresponding to this can be seen in Figure 2.25 from t = 2.5s to t = 6.0s. The signal from the "T_{up}" portions of the square wave are used to establish a "no-deflection" signal for that cycle, and the changing deflection signal from the "T_{down}" portion of the square waves gives a "deflection signal" at each Z-piezotube voltage. By differencing these two signals for *each cycle* we can beat the 1/f noise inherent in the deflection signal, because each measurement of deflection is completed in 0.1s, before significant 1/f drift occurs. This series of exact deflection vs. Z-piezotube voltage can then be fit to a straight line and the Z-piezotube

voltage which corresponds to 0 deflection then identifies the surface. This method is superior to the coarse method because it (at least partially) defeats 1/f drift, it allows more averaging, and because the tube is continually pushing above and below the surface, slow hysteretic creep does not cause inaccuracies.

Smooth Scans

Something that has allowed us to significantly speed up the rate of data collection in our experiment has been the implementation of "smooth scans". In the course of taking an electron flow image the tip must be raster scanned over the device of interest, and there are different ways this can be done. Both the simplest raster pattern and an improved raster pattern are shown below in Figure 2.26

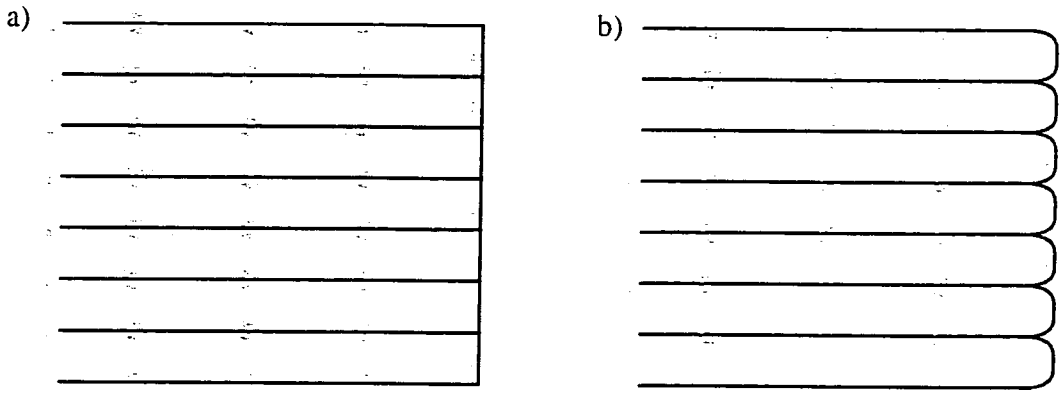

Figure 2.26 shows the rastering scheme used to improve the maximum possible data acquisition speed. Both figures show the X-Y path the tip takes during a scan consisting in this example of 8 scan lines. a) shows the simplest method where the tip is smoothly moved along the black line in the direction of the green arrows and suffers an infinite acceleration (an impulse) at the end of each scan line. b) shows an improved rastering scheme where the tip is smoothly decelerated and re-accelerated at both ends of each scan line.

In Figure 2.26a, the tip is scanned smoothly along the black path, but at the ends of each scan line it suffers a step acceleration (or deceleration) in its velocity. Before the method of raster scanning the tip shown in Figure 2.26b was implemented, the piezotube would being to vibrate at relatively slow scan speeds because of these step functions in its velocity. (Recall that the only way to a step function in velocity is by application of an impulse, which in turn sets up ringing of the tube at the tube's resonant frequency).

As a solution, the path that the tip takes was coded in software to be that shown in Figure 2.26b. In this new improved scheme, the tip undergoes a constant, finite acceleration at the end of each scan line instead of the sudden infinite acceleration in the old scheme. Thanks to the implementation of this improvement has made it possible to scan at several times the old speed without setting up significant "ringing" in the tube.

Helium Boiloff

It is important to be sure to have a hose or tube that directs helium boiloff out of the vibration isolation box if the box is ever to be closed off (by adding the lid). If this is not done, helium gas will build up inside the box and, because of the ease with which Helium passes through tiny cracks through which other gasses cannot, will eventually soften the vacuum of the dewar. This will result in high boiloff rate and, in all likelihood, ultimately an unexpected warm-up.

2.6 Electronics

This section details a number of important circuits used in the operation of the AFM experiment.

The convention used throughout this (and all subsequent) sections to indicate two different types of BNC connectors is shown in Figure 2.27. BNC connectors can either have their shields directly connected to a metal case enclosing the circuit (Fig. 2.27a) or they can deliberately isolate the shield of the BNC from the case shield (Fig. 2.27b). Using the different connectors correctly is critical in avoiding ground loops, and care has been taken to indicate in each circuit diagram the exact type of connector used. If two connectors of the type shown in Fig 2.27a are attached to the same box, one can safely assume that the shields on both are electrically connected to the box and to each other. The ground symbols attached to the cases seen in Figure 2.27 are only included wherever an explicit connection from the case to ground is made. Cases which are grounded through the shields on their BNC connections do not have the ground symbol attached to them in the schematic.

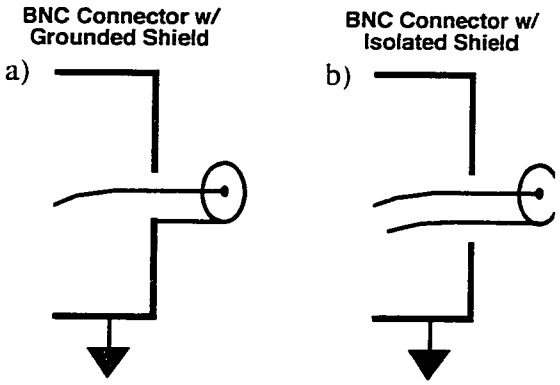

Figure 2.27 shows the schematics used to indicate grounded and isolated BNC connectors shields

Smooth switches

A very simple but important addition to the AFM involves the use of "smooth switches". These switches are used mostly in connecting the computer output voltages to

the high voltage amplifier supplying voltages to the piezotube. The design of these switches is shown below

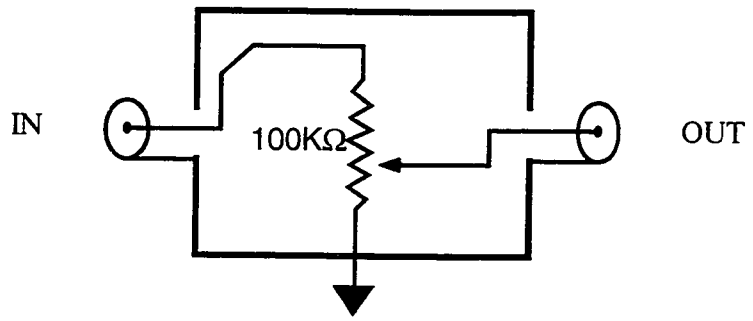

Figure 2.28 shows a simple schematic for the "smooth switches" employed throughout the experimental setup. This switch allows the output at OUT to be smoothly switched between 0V (grounded) and the input voltage (the voltage applied at IN)

These switches are critical to the successful operation of the AFM because they allow the high voltage signals to be smoothly switched to and from 0V whenever necessary. This is critical in certain instances. One such instance is if the computer crashes during operation of the AFM (a rare but not unheard of event). In this case, one must slowly lower the voltages on the piezotube to zero and reboot the computer. Before the addition of these switches, this was impossible and it was unfortunately necessary to abruptly cut power to the tube, resulting in a sudden and unpredictable jerk of the piezotube. The other situation where these smooth switches are critical is in the turning on and off of the feedback. It is often necessary in the normal course of AFM operation to disconnect and reconnect Z feedback. Whenever the output of the feedback circuit is disconnected from the piezotube, it will naturally drift to one rail or another (+/-15V which corresponds to +/-200V on the Z-electrode of the piezotube). These switches allow this voltage to be

slowly added in to (or removed from) the piezotube, allowing a smooth, jerk-free feedback on/off control.

Cantilever Electronics

The circuit used to monitor cantilever deflection is shown n Figure 2.29 on page 43. The first stage is responsible for floating the voltage of the entire tip circuit at a specified voltage with respect to ground (V_{tip}), and also providing a small (usually 0.1V) bias across the tip to allow detection of cantilever deflection. Ground reference for this entire circuit is provided through the shields attached to the dewar.

The AFM cantilever itself is part of a Wheatstone bridge circuit. The resistor values of the other three resistors, R1, R2, and R3 in the bridge have been chosen to be roughly equal to the cantilever resistance and to balance the bridge. The bridge is exactly balanced with $R1/R2 = R3/R_{cant}$ because for this choice of resistors the voltage across the bridge will be zero. High quality metal film resistors are used to avoid problems from changing resistance values between room-T and low-T. The cantilever resistance does change slightly between room-T and low-T. The resistors in the bridge are chosen to most closely balance the bridge at low temperature, and the slightly unbalanced bridge at room-T is sufficiently well balanced to work with.

The deflection detection circuit consists of two PAR 113 voltage pre-amplifiers and a voltage offset which is added into the second PAR 113. The entire cantilever circuit is floating at a voltage "V_{tip}" with respect to the ground, it there is therefore a significant common-mode voltage on the + and - inputs to the first PAR 113. The PAR113's are designed to operate linearly with common-mode voltages (CMVs) as large

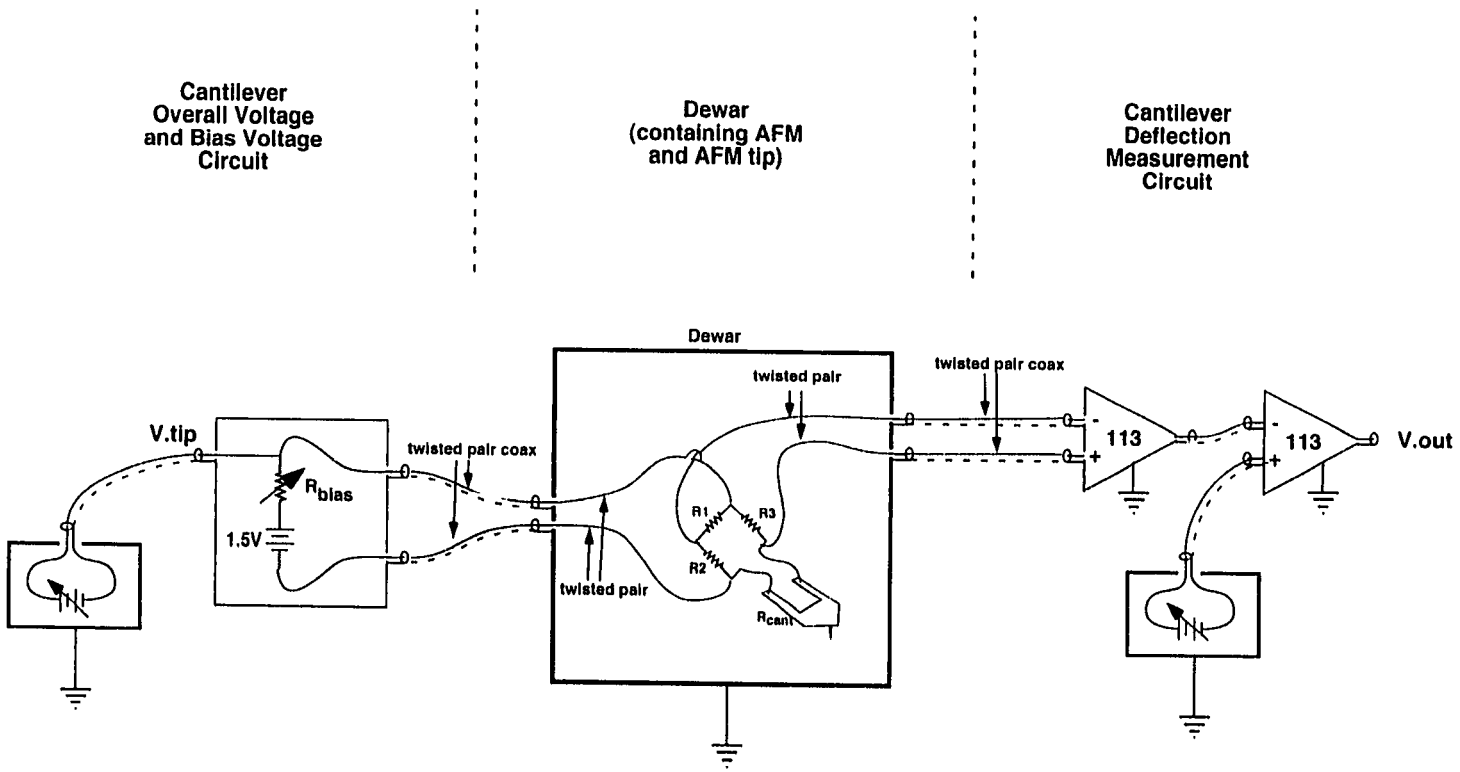

Figure 2.29 shows the circuit used to set the DC voltage the cantilever floats at relative to the 2DEG as well as to measure the deflection of the cantilever. Careful choices for shield connections has eliminated serious ground loops. An additional minor ground loop can be (and on occasion is) eliminated by cutting the shields between the dewar and the first Par 113.

as $1V_{rms}$, and to not be damaged at CMVs as high as 7.5V. The DC common-mode rejection (CMR) figure for the PAR 113 is 120dB, but is really not important in our application, because our common mode voltage is DC and simply results in a slight voltage offset on the output of the first PAR113. The total voltage gain of the two PAR113's is 100000, with the first gain usually being set to 200, and the second gain being set to 500. If the cantilever bridge is particularly well balanced, settings of 500 & 200 or even 1000 & 100 can also be used. It is desirable to use a higher gain on the initial amplification stage to minimize total noise.

The bias voltage for the cantilever circuit is usually set at about 0.2V (R_{bias} = 10KΩ in Fig. 2.29), which results in a power dissipation of about 20μW in the entire bridge circuit, and 5μW in the cantilever itself. Experimentally we have found this to be small enough to avoid increasing helium boiloff or causing sample heating.

Feedback Circuits

There are actually two nearly identical feedback circuits employed in the experiment. The circuit diagram for them is shown in Figure 2.30 on page 45. One feedback circuit is used by the AFM to take topographic scans. The second circuit is used to keep the Quantum Point Contact positioned at the center of a conductance plateau during an electrical scan.

The feedback circuit is mainly a difference integrator. The difference between V_{in} and V_{ref} is amplified by a variable gain in the first two stages (the "Differential Amplifier & Buffer" stage and the "0.01x - 100x Gain" stage. The "Integrator" stage

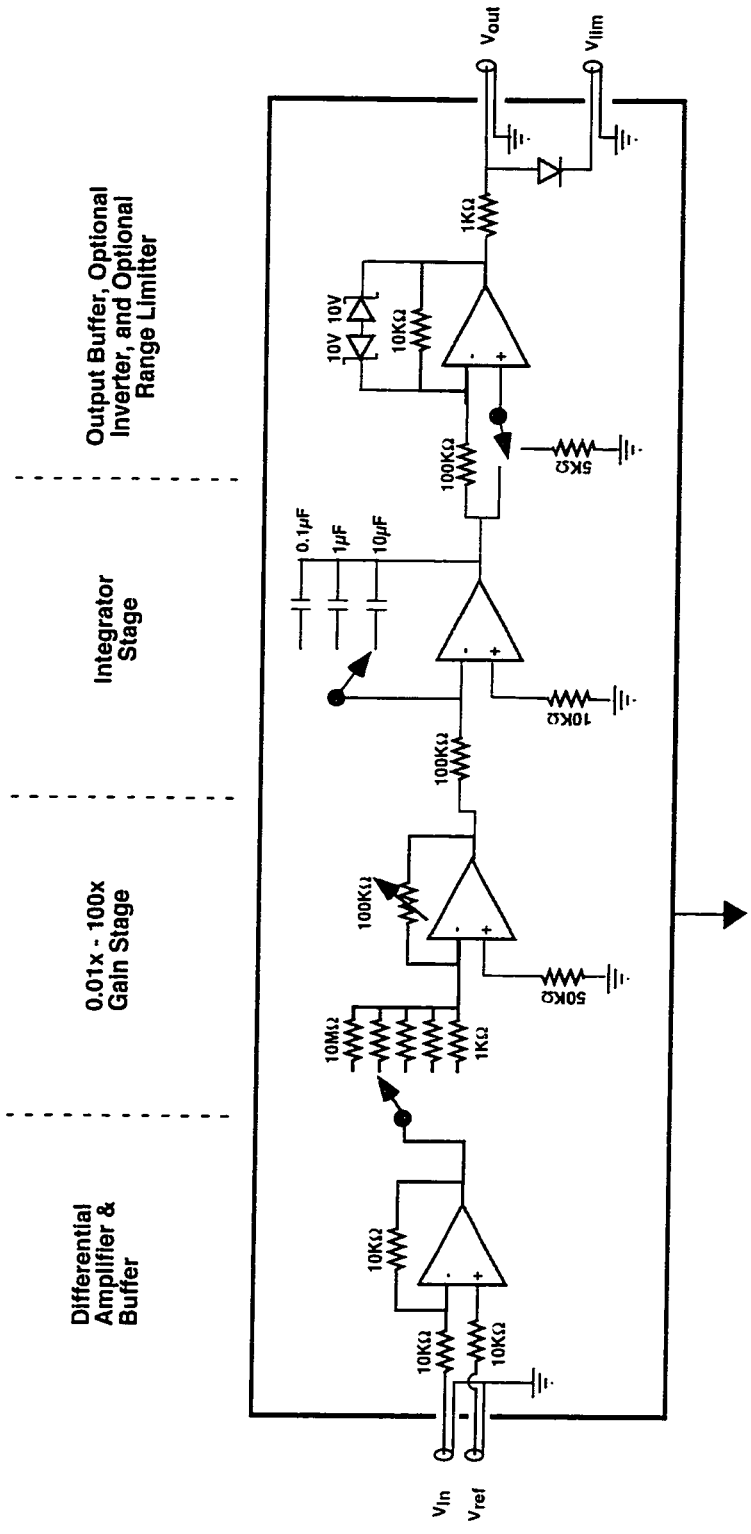

Figure 2.30 shows the circuit diagram for the feedback boxes.

then integrates this difference - if $V_{in} = V_{ref}$, then the output from this stage stays constant.

The final stage buffers the output from the integrator, and also provides both an optional inverter switch and a also an optional range limit. The range limiting is a useful addition (currently only implemented in the AFM topography feedback circuit) which has two parts. The two 10V Zener diodes keep the op-amp from ever "hitting the rails", which would cause the op-amp to go into current saturation. Once in current saturation, op-amps have a significant recovery time before they can respond to changes at their inputs- up to 50ms for the OP97s used in our circuit. This is extremely undesirable for our AFM feedback circuit because this means that during the initial approach, the tip has 50ms to plunge into the surface before the feedback circuit can even begin to respond. These diodes essentially preemptively keep the output of the op-amp from ever swinging to the rails. The other diode, connected to V_{lim}, allows the user to specify an output voltage beyond which the output from the feedback circuit is not allowed to go. This is useful if one wants to take contact scans where the tip is allowed to brush the gates but is not allowed to touch the surface. By leaving V_{lim} floating, this diode has absolutely no effect on the operation of the circuit. By defining the voltage between the shield and pin of the BNC, one can set a voltage (which turns out to be -V.lim+0.7V) above which the output is not allowed to go. The twin 10V diodes keep the op-amp from ever entering current saturation mode, however, so that there are no delays or glitches associated with having the output voltage, V_{out}, hit or leave this voltage limit.

Iso-amps

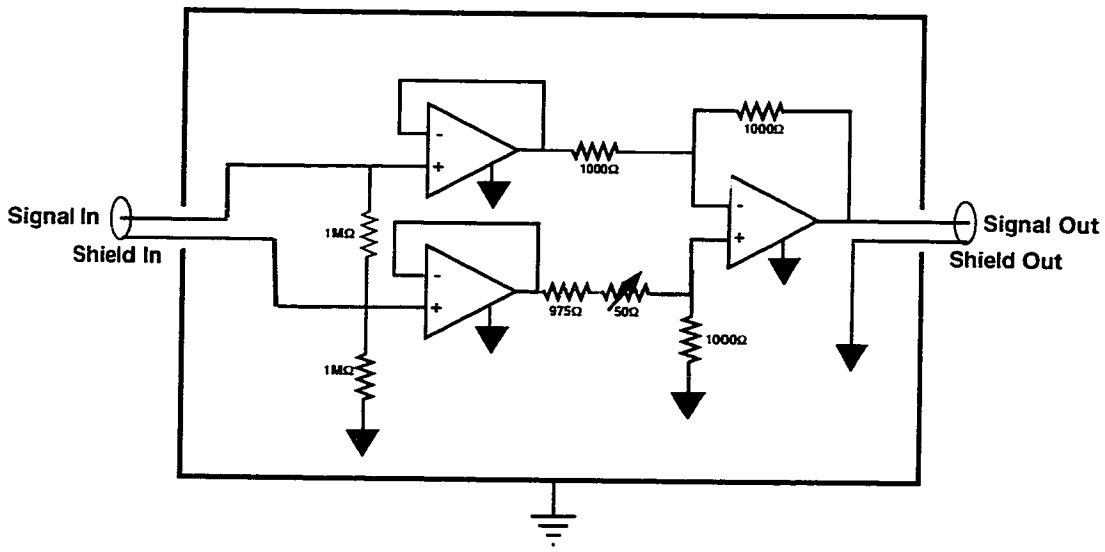

Figure 2.31 shows the circuit diagram for one isolation amplifier. This circuit is very useful for breaking potential ground loops and isolating the experiment from noisy grounds.

An isolation amplifier circuit used in many different places in the AFM experiment is shown above. It isolates the ground of the "Shield Out" from "Shield In" by 1MΩ. This is essential to isolate the sample from digital noise from the computer, and also for cutting potential ground loops. The 50kΩ pot allows for precise zeroing of the circuit. While this circuit is good for eliminating ground loops, we have not found it to be a good current buffer- if something on its output (a National Instruments board, for instance), draws lots of current in short bursts (when the multiplexor switches channels, for instance), it seems to faithfully pass these current spikes back to the input.

DAC Box

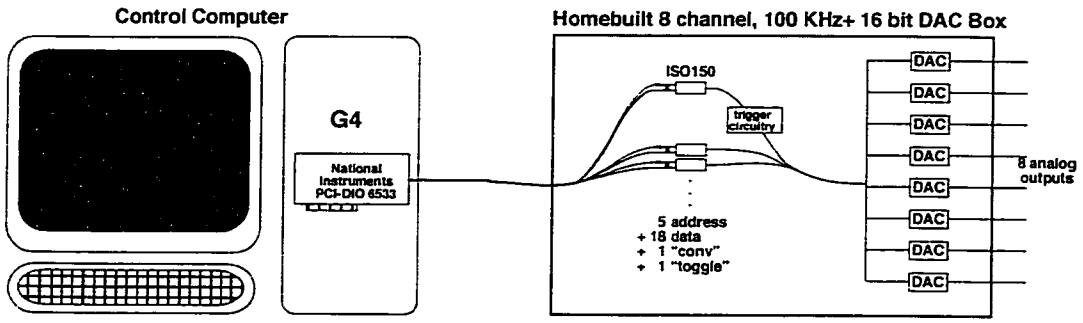

Figure 2.32 shows the new output system built by Brian LeRoy. It allows high speed, high precision, multi-channel output that is precisely synchronized with separate input channels (not shown).

The DAC box currently being used to control the AFM and the sample is shown in Figure 2.32. The computer is completely electrically isolated from the DAC box through the use of ISO150 capacitively coupled digital isolation buffers. 20 digital lines are run from the PCI-DIO 6533 (a high speed digital I/O board) in the Mac out to the inputs of the ISO150's. One difficulty with the ISO 150's is that on power-up they are initialized to random initial states (1's and 0's). It is necessary, therefore, to first turn on the DAC box and then set all the voltages to a non-zero value and back to zero before actually connecting the DAC box to the experiment.

The box in combination with the PCI-DIO-6533 is capable of up to 16 simultaneous 100KHz 16bit outputs (only 8 are currently connected) completely electrically isolated from the computer. This isolation has decreased the number of isolation boxes (shown in Figure 2.31) needed in the experiment because now all of the computers outputs are already automatically isolated from the noisey ground of the computer.

2.7 Control Software Overview

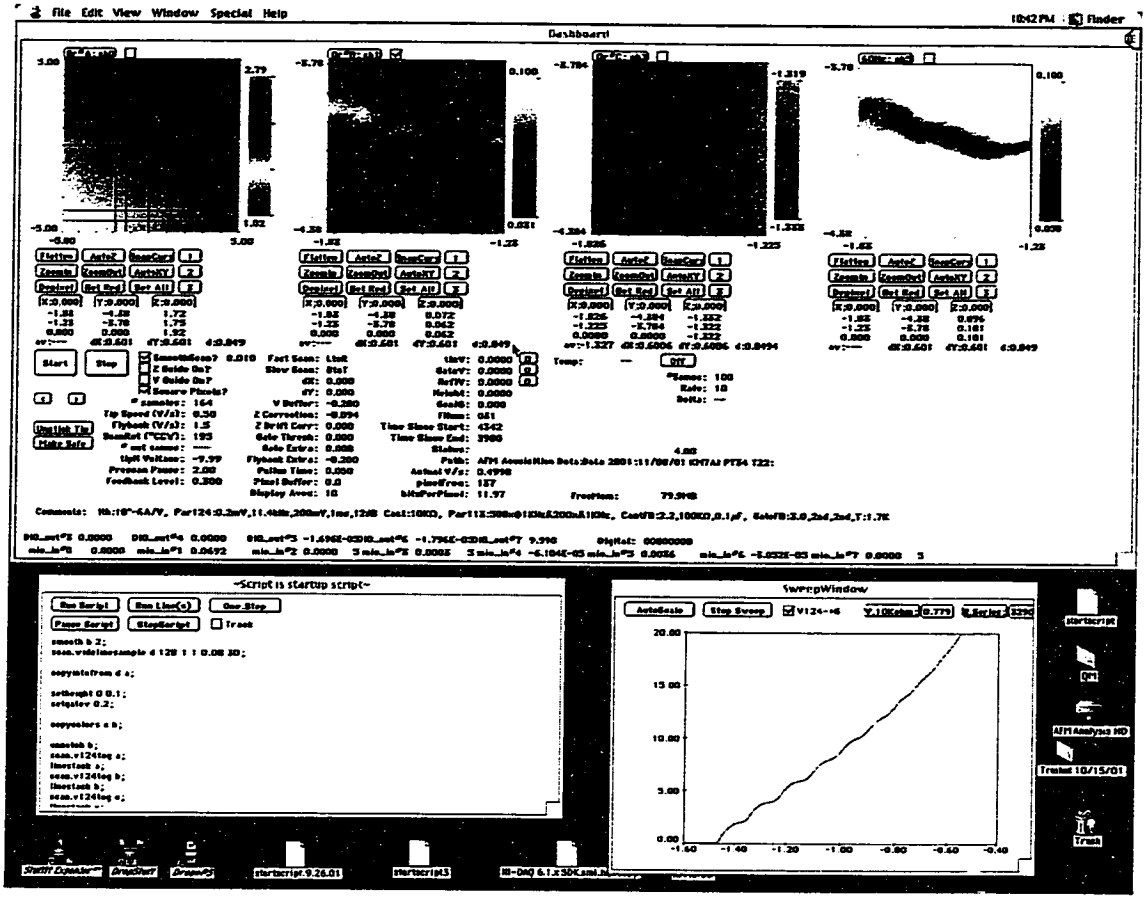

Figure 2.33 shows a screenshot of the AFM program. This program is responsible to running the AFM and simultaneously taking data from the device. It is also used to analyze and plot the data once collected.

The AFM Program (shown in Figure 2.33) has been essential to the success of the experiment. The first version was implemented in Labview 3.1, but this newer version is completely written in C (using Metrowerks Codewarrior 6). The use of C as a programming language has allowed us to control and optimize the performance of the program to levels not possible in Labview or similar high-level programming languages.

The AFM Program is used both on the data acquisition machine as well as on the data analysis machine. Most 2-d and 3-d plots for presentations and publications have been done using this home-written software. The analysis version of the program has additional controls and capabilities related to data analysis, and has all the hardware specific code removed. Most of the discussion here will be focussed on the acquisition version of the program. The functions of each of the four windows employed by the AFM program are detailed below.

Dashboard Window: The main window, called the "Dashboard" (the uppermost window in Figure 2.33), contains most read-outs and graphs related to AFM operation. The four graphs across the top of the window allow one to record and display in real-time up to four separate channels of input. Three cursors (red, green, and blue) can be seen in each graph. These cursors allow the user to zoom the graphs, select scan areas, and examine data values. All like-colored cursors move in unison across all of the graphs. The values of the data under each cursor are displayed directly below each graph. Additionally, the blue cursor always controls where the tip rests when it is not scanning. This is useful for completing measurements like those in Section 4.5 as well many other situations. The red and green cursors identify the limits of the area to be scanned when the Start button is pushed. The series of buttons underneath the graphs allow quick access to common functions and graph controls such as zooming in or out on the data, fitting and subtracting a plane from the data, autoscaling the Z color scale, and taking a line sample between the red and green cursors.

Sweep Window: The sweep window (the lower right window in Figure 2.33) is used for displaying Y vs. X graphs of things such as conductance vs. gate voltage and differential conductance vs. drain-source bias voltage and, on occasion, temperature vs. time. It can display up to 9 independent sweeps, and allows the user to scale the data conveniently and also to convert between raw voltage measurements (from the output of the PAR 124 lockin) and conductance values (in units of $2e^2/h$). I-V curves are plotted in real-time in this window while they are being collected.

Script Window: The script window (the lower left window in Figure 2.33) is a very important part of the AFM program. It allows the user to write data acquisition or data analysis scripts including loops, variables, procedures (called "macros"), and simple logic, which allow intelligent automation of the data acquisition and analysis process. In the old days before the use of automated scripts, if a user wished to take a series of images for conductance values between $1.0e^2/h$ and $7.0e^2/h$ in steps of $0.2e^2/h$, they needed to perform a labor-intensive series of steps for each and every one of the 31 scans in that series. By using a script to automate the data taking process, things can be done in a fast, error-free, reproducible, and controllable way which allows the computer to perform repetitive, otherwise mind-numbing tasks such as checking the surface position before each scan and computing the correct gate voltages to apply for each scan and remembering to save each scan when it's done, and frees up the graduate students (us) to concentrate on more important and subtle issues.

The script window has several buttons which control the use of scripts. The "Run Script" button causes the script to begin executing. The pair of brackets, "[]" show

the current point of execution- if the "Run Script" button is pushed, execution will begin with the statement between or after these brackets. If there are no brackets in the script, execution begins with the topmost line. The "Stop Script" button stops execution of the script and resets all script variables (including numeric and string variables as well as loop variables), and erases the execution point markers (the "[]"). This button is used when we want to completely abort and reset (and possibly later restart) the script. The "Pause Script" button suspends operation of the script, but does not clear any variables, and leaves the execution point (indicated by "[]") where it was before being paused. The "Run Lines" button allows the used to select a group of lines in the script which will be executed, followed by a stopping and resetting of the script. The "One Line" button allows a user to single-step through a script one line at a time, and is very useful for debugging and testing purposes.

Console Window:

The console window is hidden in Figure 2.33. It is simply used to output status messages during AFM operation. It is purely an output window- there is no area for user input on the console window. It has a 10K looping buffer that stores all output messages. This allows messages that have scrolled off the top of the window to be viewed by resizing the Console Window.

2.8 Lithography

Most lithography performed during this experimental work uses standard techniques which have been perfected by previous students in the lab. A number of excellent and thorough descriptions of the techniques for SEM lithography and thermal evaporation can be found in previous group theses[7]. The procedures and details which are unique to this experiment are detailed here.

Bonding Pad Placement

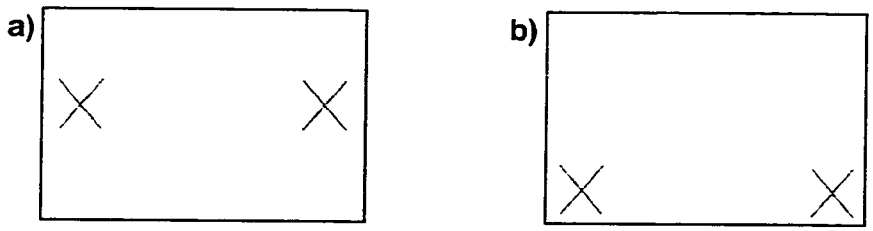

Figure 2.34 shows a unwise (a) and wise (b) placement of wirebonding pads for the ohmic contacts and electrostatic gates on a device. (a) shows an improper placement of bonding pads, where the wirebonds will interfere with the AFM tip when the tip is brought close to the surface. (b) shows a proper placement of the bonding pads, all on one side of the active device region (the narrow channel in between the two split gates)

Figure 2.34 shows improper (a) and proper (b) placement of gate and ohmic bonding pads. The AFM cantilever chip must be held nearly parallel to the surface of the sample, so it is important to leave the upper half of the chip free of wirebonding pads so that the AFM cantilever chip can approach close to the surface without grazing any wirebonds. The device is designed so that all of the electrostatic gates and ohmic bonding pads lie on one side of the device.

7. J.A.Katine, Ph.D. Thesis, Harvard University (1996), D.S.Duncan, Ph.D. Thesis, Harvard University (2000)

Etch Trenches

For samples that use a backgate connection, it is important to be able to create etch trenches which can cut the 2DEG on a chip into different sections which are electrically separate. The procedure for defining an etch trench which cuts through the 2DEG but does not reach the n+ GaAs substrate is outlined below (thanks to Lester Chen for the original recipe).

- define etch trench shapes using standard bilayer PMMA and SEM techniques
- quick dip in distilled water (plastic beaker #1)
- 5s dip sample in 1:5 (by volume) (30% NH_4OH solution):H_2O. (plastic beaker #2)
- 5s dip sample in 1:5 (by volume) (37% HCl solution):H_2O (plastic beaker #3)
- quick dip in distilled water (plastic beaker #4)
- 45s dip in 50° citric-H_2O_2 etch solution (see below) (glass beaker)
- first rinse in distilled water (plastic beaker #6)
- second rinse in distilled water (plastic beaker #7)
- Acetone to remove PMMA

The citric-H_2O_2 etch solution consists of 10mL of 1:1 (by weight) citric acid:H_2O and 1mL of 30% Hydrogen Peroxide solution (H_2O_2). It is heated on a hot plate to 50° before starting. The 45s dip in this etchant at 50° results in a roughly 700nm etch.

Contacting the Backgate

We have developed a particularly simple method for contacting the "backgate". The material used for all results in this thesis is known inside the lab as KM7, and was grown on top of a degenerately doped n+ substrate which serves as a backgate. The heterostructure is shown in Figure 2.35.

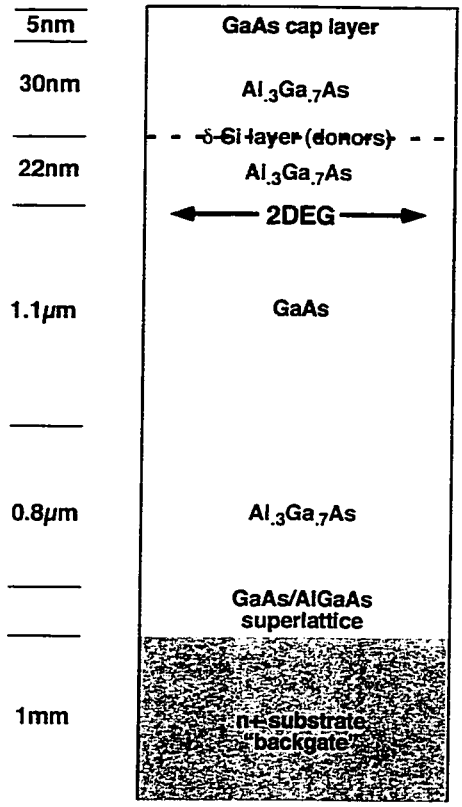

Figure 2.35 shows a cutaway view of the heterostructure used in our experiments. The 2DEG resides at the interface between the AlGaAs and GaAs 57nm beneath the surface.

It is important to be able to make separate electrical contact the 2DEG and the backgate. The general scheme used to accomplish this is shown in Figure 2.36, and involves first separating the wafer with etch trenches into a center 2DEG region (shown in light green) which will contain the device, and any number of edge regions (shown in white) which are separated electrically from the central 2DEG region. The etch trenches used are deep enough to cut through the 2DEG but are not deep enough to reach the backgate. The fact that the edge 2DEG regions defined by these etch trenches are electrically isolated from the "active 2DEG region" will allow us to make contact to the backgate without making contact to the 2DEG. A relatively large region of 2DEG is separated from the main active 2DEG region along one side of the chip (on the far right in Figure 2.36). The edge of the wafer along this side is then scraped with a sharp scalpel at a 45° angle after the trilayer of PMMA for the ohmic contacts has been spun. All

the ohmics shown in the figure are then written, evaporated, and annealed. The final result is that 2DEG ohmic contacts make contact to the active 2DEG region and the Backgate ohmics make contact to the backgate without causing any shorts between the active 2DEG and the backgate.

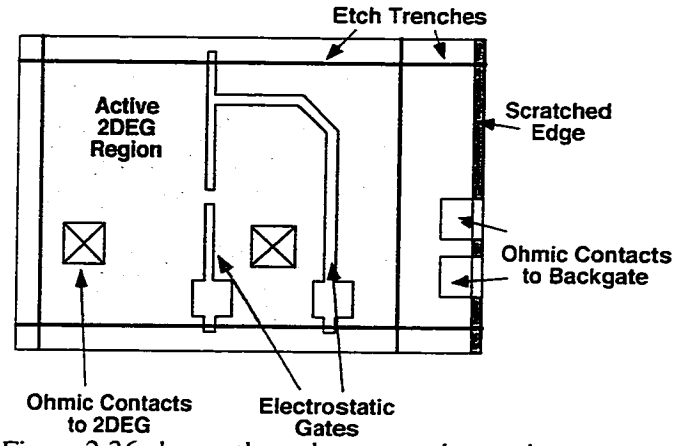

Figure 2.36 shows the scheme used to make separate electrical contact to the 2DEG and the backgate.

Chapter 3

Imaging Current Flow

3.1 Introduction

This chapter is focussed on understanding our method of imaging coherent electron flow. This method consists of scanning a negatively charged AFM tip above a nanoscale device and measuring the effect of the tip's perturbation on the conductance through the device as a function of tip position (Figure 3.1). The tip capacitively couples to the 2DEG and, if the tip potential is sufficiently negative, it creates a small depletion disc directly beneath it. When the tip is over an area of relatively high current flow, the depletion disc beneath will backscatter electron flow, and it will have a correspondingly large effect on the conductance through the device. When the tip is over an area where very little current flows through the device, it will have a correspondingly small effect on the conductance. By raster-scanning the tip over the device and simultaneously measuring the conductance through the device we can compile an image of the current flow.

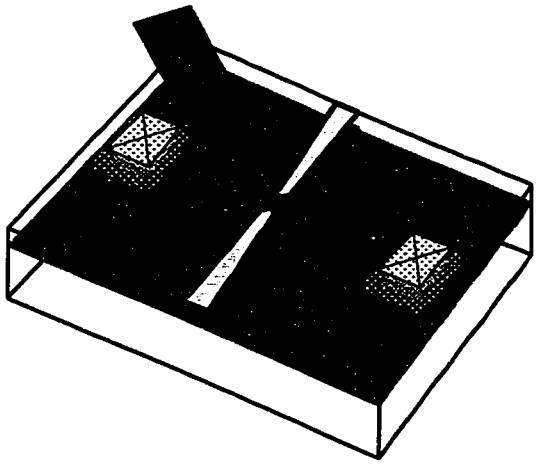

Figure 3.1 shows the basic experimental setup used to image coherent electron flow. Electrons flow from one ohmic contact (the X'ed boxes) to another through the quantum point contact (QPC) channel (defined by the two electrostatic split gates). The negatively charged AFM tip is used to induce a movable depletion disk which can block electron flow through the QPC.

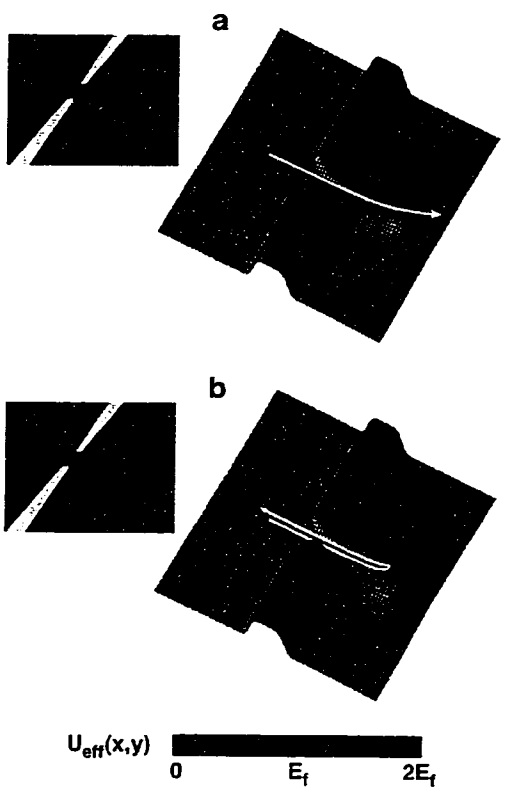

Figure 3.2 This figure shows the two basic modes in which the apparatus can operate. a) here the perturbation from the tip is too weak to create a depletion region, and electron trajectories are bent but not backscattered. b) here the perturbation is strong enough to create a depletion disk, and electron trajectories can now be backscattered from the tip 180° back through the QPC.

There are two fundamentally different modes of imaging that our AFM can be used in. Figure 3.2 shows these two modes- in (a) the tip is inducing only a weak scatterer in the 2DEG, while in (b) the tip is creating a strong depletion region in the 2DEG. If the perturbation from the tip is too weak to create a depletion region (Fig. 3.2a), the flow through the device is bent and lensed by the tip, but the total current flow through the device is largely unchanged. The first part of this chapter, which consists of Sections 3.2 through 3.4 investigates both theoretically and experimentally this "weak scattering" mode of operation. Although it is not possible to image current in this mode of operation, useful information about the mechanisms behind our technique can be collected. In order to image electron flow, the AFM must be operated in the second of these two modes- the tip must create a depletion region directly beneath it which backscatters electron waves (Figure 3.2b). Section 3.5 introduces this main mode of operation, in which it is possible to image coherent electron flow.

3.2 Calculation of Induced Charge Profile from Tip

In this section we theoretically investigate the perturbation of a 2DEG by a charged AFM tip. When the AFM tip is positioned directly above the 2DEG wafer, the conducting tip of the AFM couples capacitively to the 2DEG and introduces a local density perturbation beneath the tip. We numerically modeled this situation using a home-written 3-D Poisson solver. Figure 3.3 shows the physical geometry of the AFM tip and underlying 2DEG. The exact values of the different physical parameters are difficult to determine precisely, but best estimates for normal values used while acquiring current images are: h = 10 nm, L = 2 μm, d = 57 nm, and R = 40 nm. The resulting induced charge from placing the tip as shown (10 nm above the surface of the wafer) and holding the tip at 1V with respect to the 2DEG is shown in Figure 3.4. The 2DEG is assumed to behave as an equipotential (essentially a thin metal sheet) up until depletion.

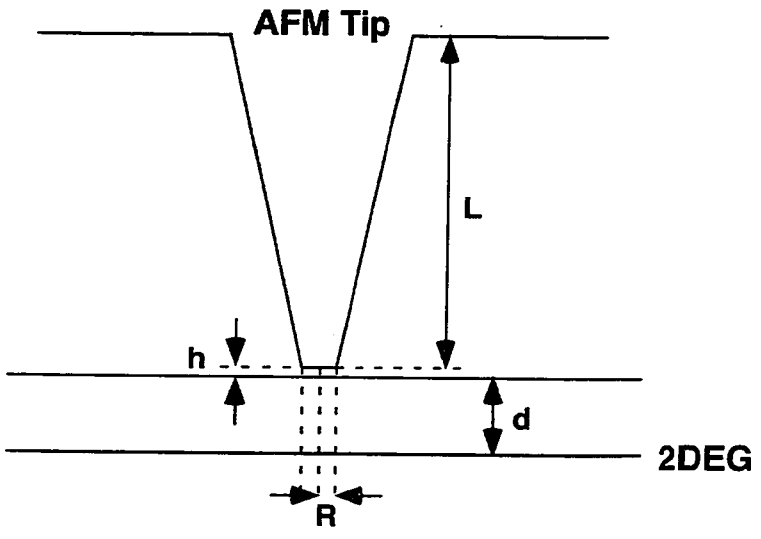

Figure 3.3 shows the tip geometry used in the Poisson simulations in this section.

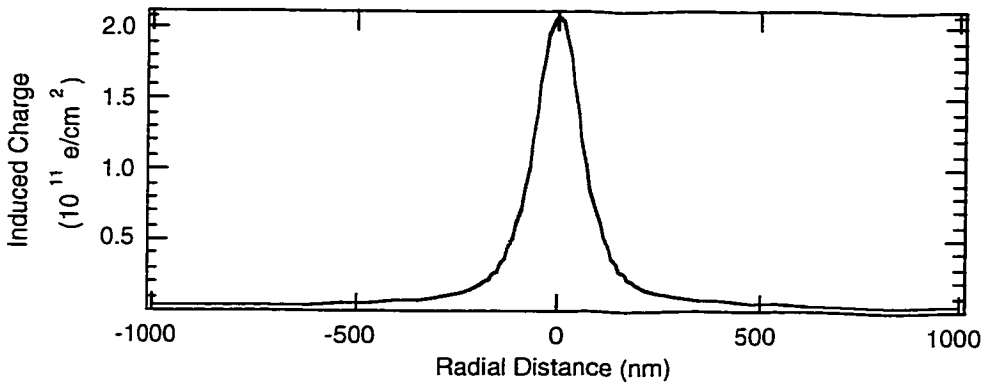

Figure 3.4 shows the charge induced in the 2DEG when the tip is held 10nm above the surface of the 2DEG and is held at 1V with respect to the 2DEG. The geometry used in this simulation is shown in Figure 3.3, with R = 40 nm, h = 10 nm, d = 57 nm, and L = 2 μm.

The results from this simulation (see Figures 3.3 and 3.4) show that if the tip is held 10nm above the surface of the 2DEG, a tip voltage of -2V with respect to the 2DEG will produce a depleted disk beneath the tip for sheet density $n = 4.2 \times 10^{11}$ e/cm^2. The results of the simulation beyond this voltage are not as accurate, because at this point the assumption of the 2DEG being an equipotential breaks down directly beneath the tip. The result from this simulation that -2V is needed to create a depletion region (and hence to be able to image current) agrees quite well with measurements- see Section 3.5 for the comparison.

As an additional way to build intuition and also as a check on the induced charge profile calculated using my Poisson solver we can compare the exact computed charge profile for a realistic tip (using the geometry used in Figure 3.3 and 3.4) with what would

be induced from placing a point charge at the same height[1]. A comparison for h=10nm (the usual operating height of the tip) is shown below:

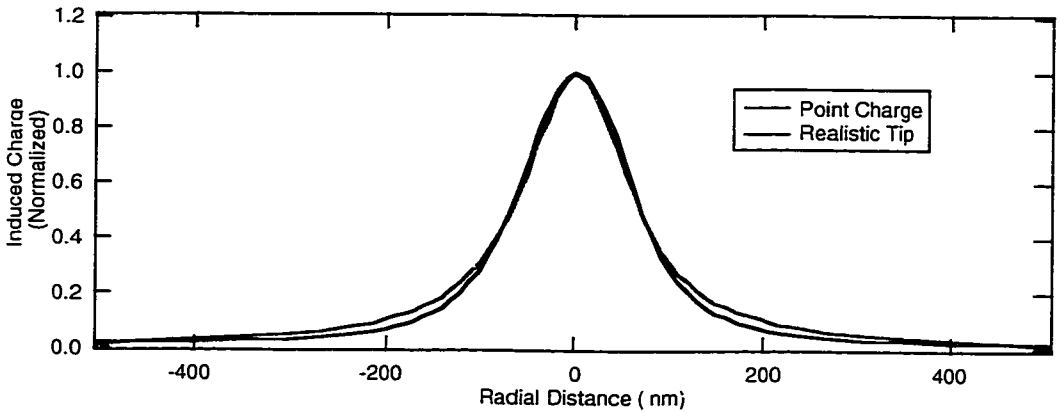

Figure 3.5 shows a comparison between the exact calculation of induced charge for a realistic tip 10nm above the surface (black) and the induced charge beneath a point charge also located 10nm above the surface of the wafer (black).

The two results match quite well, with the difference in FWHM between the two of about 1%. Thus, a useful physical intuition to keep in mind is that the tip can be thought of, to a reasonable degree of accuracy, as a point charge. Throughout this thesis, however, the results of the Poisson simulation will be used since they do represent an increase in accuracy.

It is useful to investigate the dependence of the perturbation shape and strength on the tip height (the distance between the GaAs surface and the bottom of the tip). Scanning with the tip as close to the surface as possible is critical to obtaining images of current flow, and the following series of calculated tip perturbations at different tip heights shows why.

---

1. see Appendix A for more information on the point charge calculation.

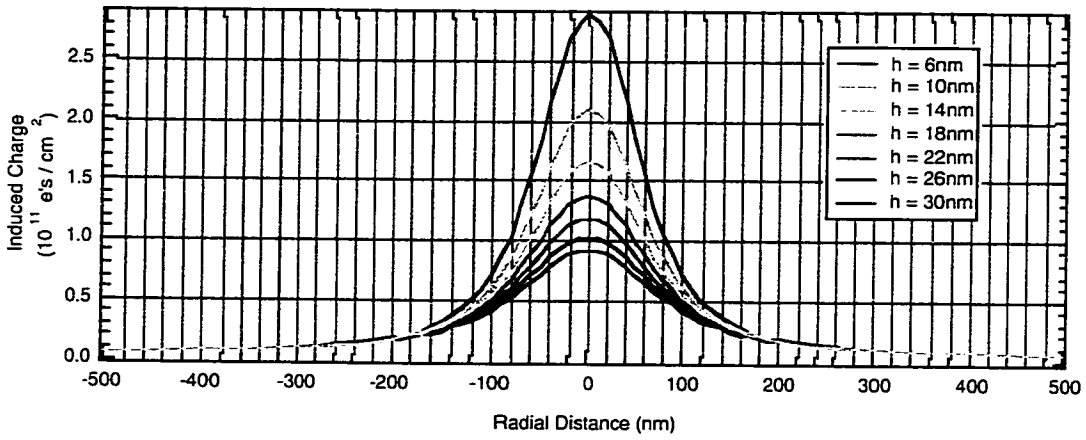

Figure 3.6 shows the calculated tip perturbation for heights ranging from 6nm to 30 nm above the GaAs surface. Other parameters used in these calculations were: r = 40 nm, angle = 6°, V = 1 V, and d = 57 nm.

Because the largest voltage we can safely apply to the tip is about -4V[2], in order to create any depletion region at all we must be within 25nm of the surface (for $n_s = 4.2 \times 10^{11}$ e/cm^2 and $V_{tip} = -4$ V). In order to create a reliable depletion region which does not change size radically with slight variations in tip height, surface roughness, or imperfections in the tip we should try and be significantly closer than this.

Another important point to take away from Figure 3.6 is that the full-width at half maximum of the perturbation introduced by the tip, even for tip heights less than 10nm, is quite large - for h = 10nm (a common operating height), the FWHM is 120nm. This relatively wide lower limit on the perturbation is to be expected, because even if the tip were on the surface, the 2DEG is still 57nm away. Even with a relatively large FWHM of the tip perturbation, it turns out that the actual resolution limit in our experiments is not lim-

2.There is some evidence that tip voltages much larger than -4V can cause the tip to field emit. Also, common mode voltages larger than about 3V seem to cause a slow degradation of performance in our voltage preamplifiers (model PAR-113s).

ited by this dimension - features in the current flow images on the order of 5-10nm are easily visible. The origins of this surprisingly high resolution are explained in Section 3.5.

3.3 Experimental Determination of Tip Perturbation

It is possible to measure the actual induced charge underneath the tip and compare these measurements with theoretical predictions from Section 3.2. In order to do this we apply a large ac bias voltage (V_{ds} = 5.0 mV) across the QPC to blur out the plateaus and make its response roughly linear in gate voltage, and then we raster scan the QPC underneath the tip. This experimental setup is shown below in Fig. 3.7.

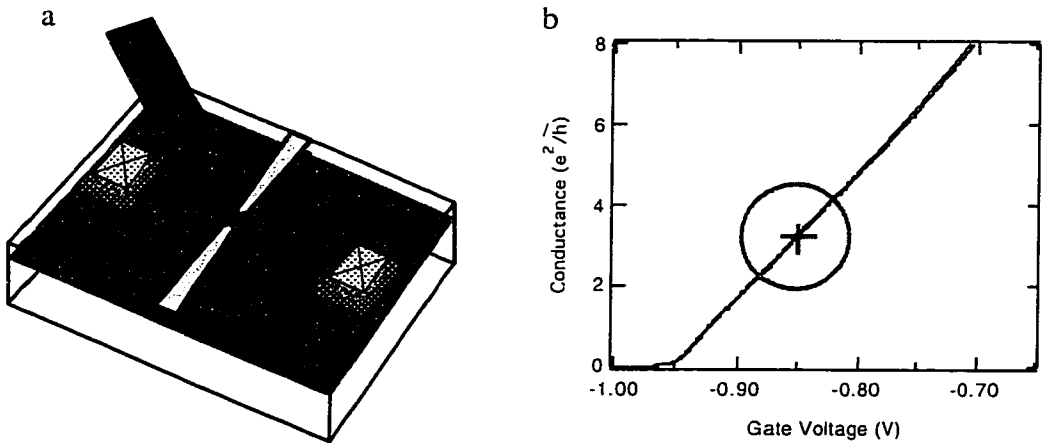

Figure 3.7 shows the setup used to measure the perturbation introduced to the 2DEG by the charged AFM tip. a) shows the AFM tip positioned above the 2DEG sample introducing a weak density perturbation (not high enough to create a depletion region). b) the QPC is biased at a high bias-voltage (5mV) which blurs out the plateaus and allows the conductance to be a linear function of the induced charge in the QPC channel. The operating point is indicated by the blue circle. By raster scanning the QPC underneath the tip, an image of the tip perturbation can be compiled.

In these measurements the tip voltages are purposely kept low enough, and the tip-sample separations large enough, to prevent the tip from ever creating a depletion region

below it. By doing so we guarantee that the dominant effect that the tip has on conductance through the QPC is from its capacitive coupling to the 2DEG in the QPC channel. If a depletion region were formed it would directly backscatter electron waves, overpowering the simple capacitive effect we are attempting to measure.

By raster scanning the QPC sample back and forth underneath the tip and simultaneously measuring the conductance through the QPC, a 2D image of the charge induced by the tip can be compiled as shown in Fig 3.8a below.

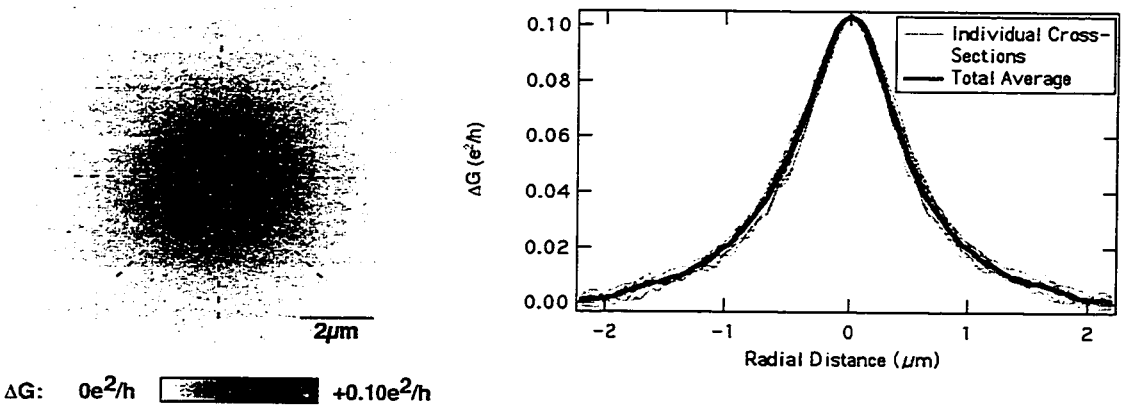

Figure 3.8 shows the measurement and analysis used to obtain tip perturbations. a) Shows the data taken for the tip held at 500nm above the sample surface with +3V on the tip. The black dashed lines show the lines along which cross sections were taken. b) These cross-sections are then averaged together to obtain an average radial profile of the tip perturbation.

Figure 3.8 shows the measurement used to obtain the induced tip perturbation for one particular tip height (500nm for Fig. 3.8). Because we are operating the QPC in the linear response regime due to the high source-drain bias voltage (see Figure 3.7b), the change in conductance through the QPC plotted in Figure 3.8a is linearly proportional to

the charge induced in the channel region of the QPC, and hence this ΔG image is also an image of the induced charge profile from the tip.

By repeating the measurement and analysis shown in Figure 3.8 for different tip heights we can compile a series of tip perturbation radial cross sections and test whether our simple electrostatic picture given in Section 3.2 is accurate in describing the tip perturbation. The results of this series of measurements, as well as a comparison with the theoretically calculated tip perturbations, is shown in the figure below (Figure 3.9).

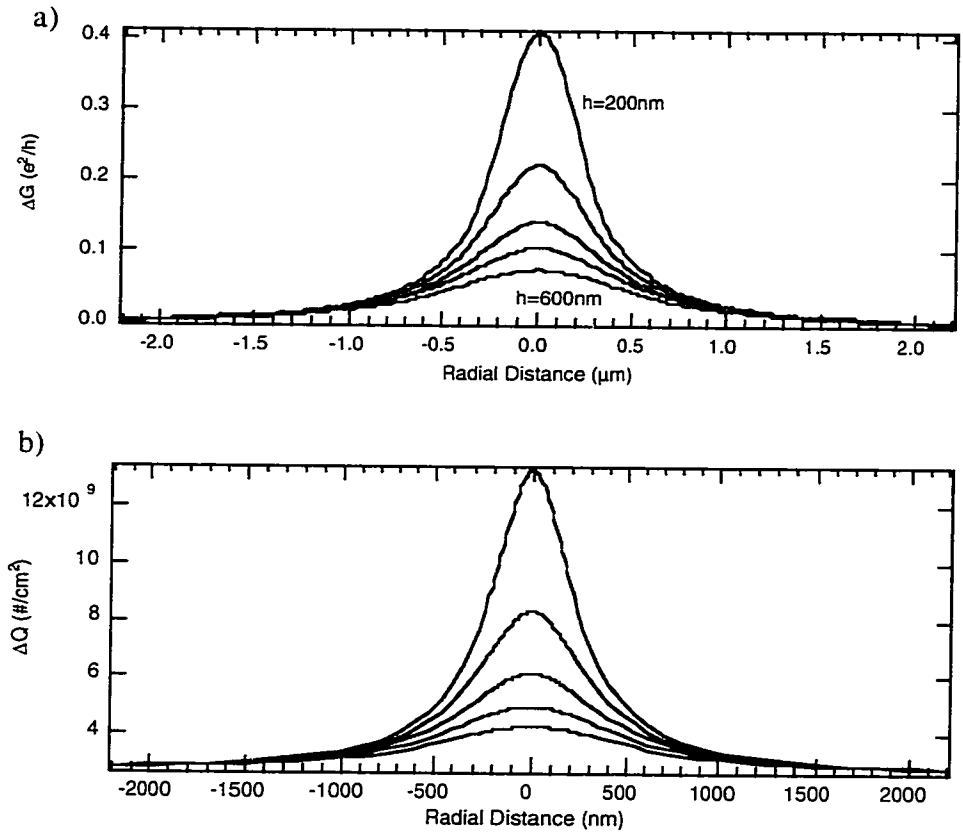

Figure 3.9 shows measured and theoretical tip perturbations for tip heights ranging from 200nm to 600nm above the GaAs surface. a) shows the experimentally measured tip perturbation, and b) shows the theoretically computed tip perturbation. There is excellent agreement between theory and experiment.

There is excellent agreement between the peak amplitudes of our calculations of the induced charge profiles and the actual measured profiles. In order to further compare the dependence of the shape and width of the calculated and measured perturbations it is helpful to present the above series of calculated and measured perturbation in a normalized format, with each radial cross-section rescaled to run from 0 to 1.

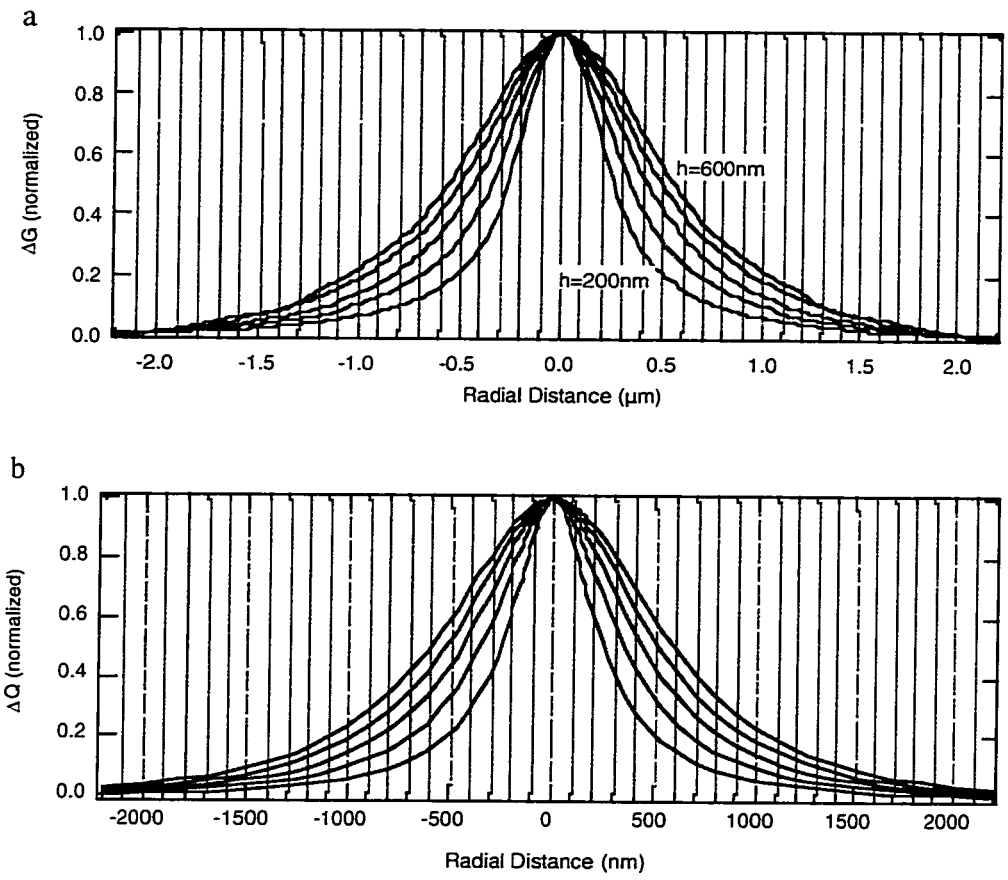

Figure 3.10 shows the normalized series of measured tip perturbations for heights ranging from 200nm to 600nm above the GaAs surface in 100nm steps. The normalized cross sections allow easier comparison of half widths for different tip heights

Again, as with the magnitude of the induced charge perturbations, the agreement in perturbation shape and width between calculations and theory is excellent. These results give us confidence that our simple electrostatic picture we use to model the tip, with the tip being one equipotential and the 2DEG being another, is a very good approximation to the real system.

3.4 Tip as a Moveable Gate

In this section we present measurements where the perturbation is stronger than in Section 3.3, (using a larger tip voltage and bringing the tip closer to the surface) but is still kept smaller than would be necessary to create a depletion region. We show that it is possible to drive the QPC through several conductance plateaus simply by changing the tip to QPC distance. We find, interestingly, that the presence of a relatively large (but still not depleted) perturbation from the tip leaves the conductance plateaus nearly unchanged.

As in Section 3.3, so long as the voltage on the tip is kept from being too negative or the tip height is kept sufficiently large, the dominant effect that the charged AFM tip has on conductance through the QPC is that of a movable gate. The tip induces a charge perturbation as shown in Sections 3.2 and 3.3, but as long as the height of the density perturbation is smaller than the sheet density[3] of the 2DEG, the resulting potential bump simply bends electron trajectories without backscattering them. The conductance

3.If the perturbation were extremely sharp compared the electron wavelength, it would be possible for it to backscatter electron waves even if it were significantly below the Fermi level (i.e. significantly far away from creating a depletion region), much like light is both reflected and transmitted by a sharp change in refraction index. Section 3.2 showed, however, that the FWHM of the expected tip perturbation even when the tip was within 5nm of the surface would still be long on the order of the electron wavelength (FWHM=120nm, λ=40nm). And in this section the tip is held significantly farther away from the surface than this.

through the QPC is unchanged by this lensing effect. The tip perturbation extends all the way to the QPC, however, where the induced charge from the capacitive coupling between the tip and the QPC channel does have an effect. This effect was used in Section 3.3 to image the charge perturbation underneath the tip, and it is used in this section to drive the QPC through several conductance plateaus.

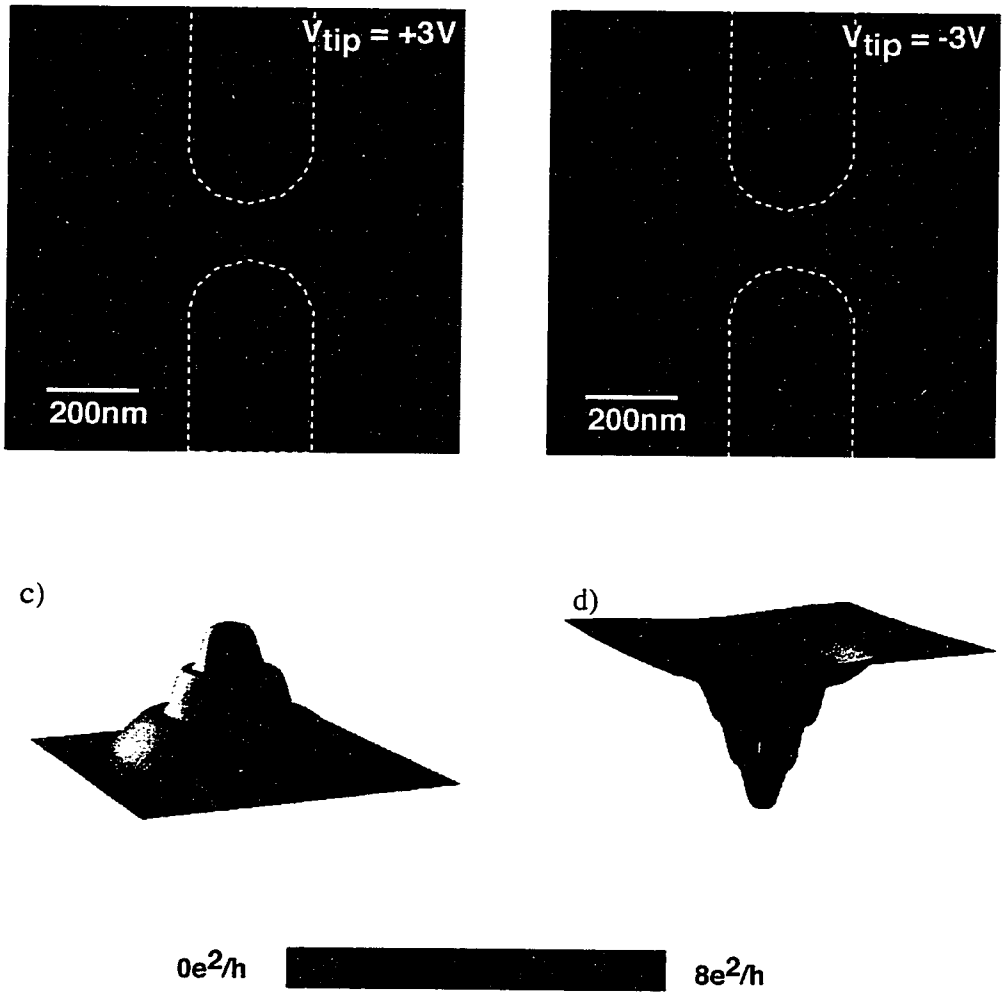

Figure 3.11 a-d show scans which illustrate the use of the charged AFM tip as a movable gate. c) is a 3d-plot of the same data as that shown in a), and d) is a 3d-plot of the same data as that shown in b). a) and c) show the effect a positively charged tip can have while b) and d) show the effect of a negatively charged tip.

In Figures 3.11a and 3.11c the QPC is biased so that when the tip is far away the QPC is pinched off ($G = 0e^2/h$). As the tip moves closer to the QPC, however, the tip-QPC channel capacitance increases and the tip draws charge back into the depleted QPC, restoring conductance to the 1st, 2nd, and finally when the tip is directly over the QPC, 3rd plateaus. Conversely, Figures 3.11b and 3.11d show the effect of using a negative tip voltage. The QPC can be pushed from the 4th plateau (when the tip is far away from the QPC) all the way to depletion (when the tip is directly over the QPC).

One very interesting result of these measurements is the conclusion that the presence of a reasonably strong (but not depleted) perturbation from the tip does not significantly disrupt conductance through the various modes of the QPC even when the peak of that perturbation is placed squarely in front of or right in the middle of the QPC. In fact, the conductance plateaus are remarkably unaffected by this perturbation, as can be seen from the following figure (Fig 3.12)

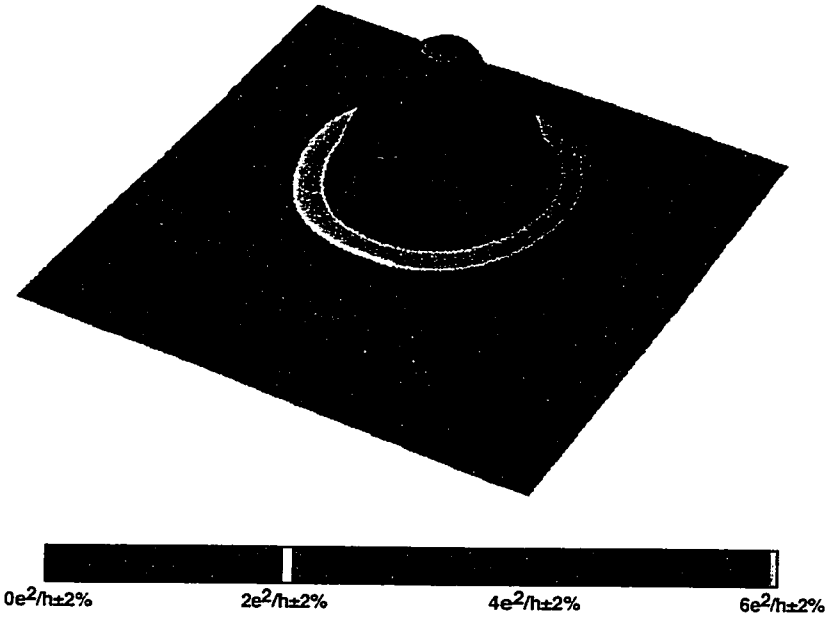

Figure 3.12 shows the high degree of robustness against non-backscattering perturbations that the QPC has. The color bands are centered on multiples of $2e^2/h$ and extend $\pm 0.04e^2/h$, or 2%, on either side. V_{tip}=+3V for this image.

This figure is the same scan as in Fig. 3.11c with a different color scale chosen to emphasize any deviations from perfect conductance quantization. This figure demonstrates that the presence of a large perturbation, even directly in front of the QPC affects the plateau heights by significantly less than 2%.

For the scans in Figures 3.11 and 3.12, the tip was held at ±3V at a height of 100nm above the surface. Poisson simulations (identical to those shown in Figure 3.9b but using h=100nm and V_{tip}=+3V) give an expected peak perturbation height of $0.9x10^{11}e/cm^2$. This corresponds to a 21% change in the density of the 2DEG directly beneath the tip. These measurements indicate the somewhat surprising result that an impurity, donor inhomogeneity, defect, or charged tip which makes a perturbation as large as 20% of the density of the 2DEG with a HWHM (half width at half max) as small as approximately 150nm will not significantly affect the quality of the conductance plateaus through a QPC.

3.5 Imaging Current - Tip as a Moveable Backscatterer

In the previous section (Section 3.4) we reached the somewhat surprising conclusion that the perturbation from the tip could represent a density perturbation larger than 20% of the total sheet density and still not change the transmission coefficient of electron waves passing through a QPC. The changes in conductance seen in Figures 3.8 through 3.12 were all due to indirect capacitive coupling between the tip and the QPC channel, and depended purely on the height and distance between the QPC and the charged tip, (and, specifically, not on whether or not the tip was positioned above current flowing from the QPC).

In this section we make the critical discovery that this picture changes entirely once the strength of the perturbation from the tip is such that it causes a depletion region to form. The presence of a depletion region allows the tip perturbation to actually back-scatter electron waves back through the QPC, which in turn means that the effect the tip has on conductance through the QPC depends largely on whether or not the tip is inter-rupting flow from the QPC. Creating a depletion region with the tip allows us to image current flow.

Figure 3.13, below, shows a series of scans taken at a series of different tip voltages.

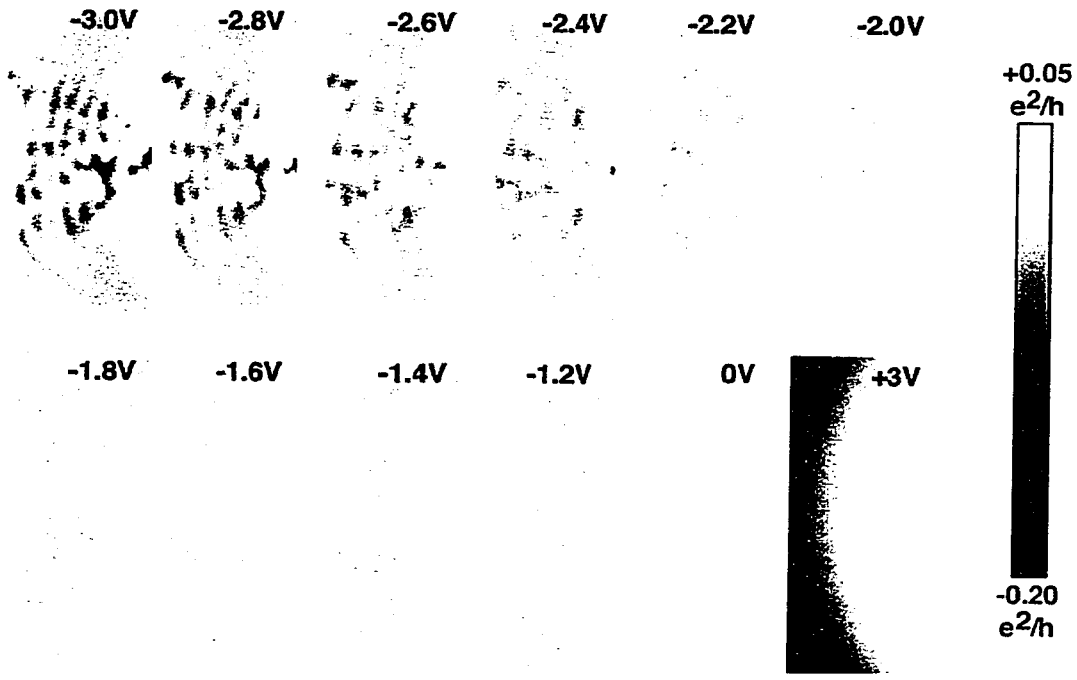

Figure 3.13 shows a series of scans demonstrating that it is necessary to create a depletion region beneath the tip in order to image coherent electron flow. Any tip voltage more positive than -2.0V is not sufficient to create a depletion region, and no current pattern is seen.

As was mentioned in Section 3.2 on page 60, calculations of the tip perturbation indicated that for h_{tip} = 10nm and R_{tip} = 40nm (a reasonable estimate for the tips we use), V_{tip} = -2.0V is required to create a depletion region (a perturbation that represents a 100% change in sheet density). The agreement between this estimate and experiment is quite good, as the observed current pattern in Figure 3.13 disappears at V_{tip} = -2.0 or V_{tip} = -1.8V. At this point, the tip's perturbation changes radically in character, going from a lens for voltages more positive than -1.8V to being a backscatterer for voltages more negative then -2.0V. The difference is illustrated in this schematic repeated from earlier in this chapter:

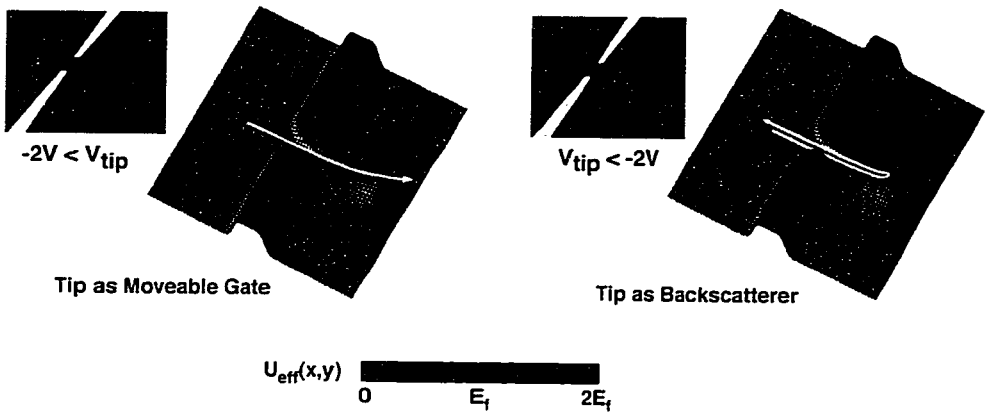

Figure 3.14 This figure shows the two basic modes in which the apparatus can operate. a) here the perturbation from the tip is too weak to create a depletion region, and electron trajectories are bent but not backscattered. b) here the perturbation is strong enough to create a depletion disk, and electron trajectories can now be backscattered from the tip 180° back through the QPC.

Using the tip in the "backscattering" or "imaging" mode thus allows one to image the current through a device by raster scanning the tip above the device and measuring the

change in conductance through that device as a function of tip position. When the tip, and accompanying depletion disk, is above a region of high electron flow, a relatively high flux of electron waves will be backscattered back through the device, thus decreasing the overall conductance. The capacitive effect discussed in Section 3.4 is still in effect as well, but the dominant effect on the conductance through the device is from the direct backscattering of electron waves from the tip. This is especially true if the device being scanned is a QPC biased on a conductance plateau, since in this case indirectly capacitively induced charge in the QPC channel from the tip has no effect on the conductance, and the only changes in conductance come from electron waves backscattered from the tip.

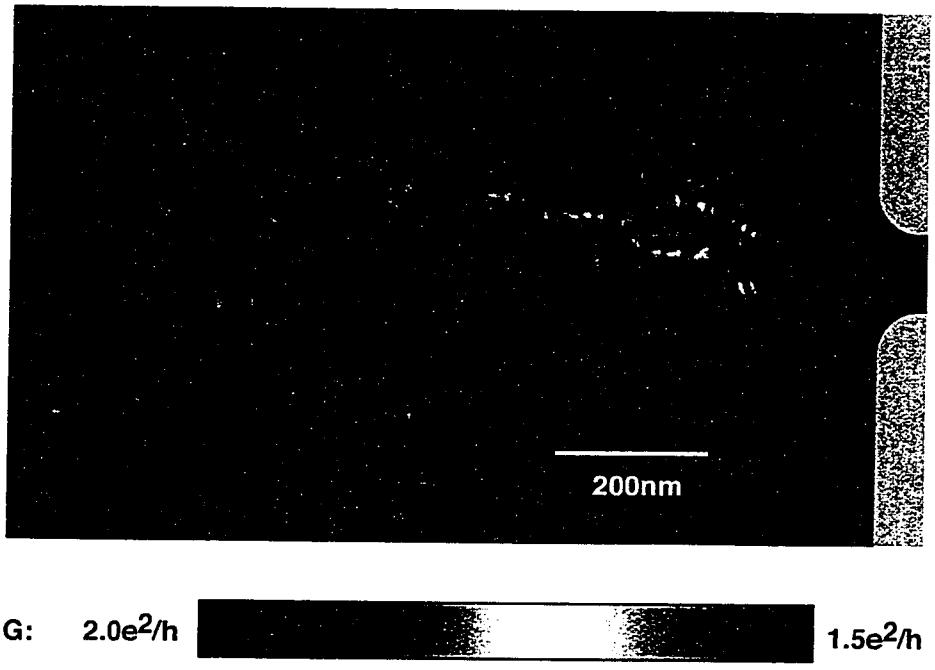

Figure 3.15 shows an example of the images of current flow that are possible from using a movable tip which introduces a perturbation strong enough to backscatter electron waves. Of note is the surprisingly good resolution, much better than the expected 120nm FWHM tip perturbation from placing the tip 10nm above the surface of the wafer.

Using the tip in the strongly backscattering mode allows images such as Figure 3.15 to be taken, which shows the current flow from a QPC biased at $G = 2e^2/h$. Images such as this are, of course, the topic of the rest of this thesis. Precisely why the flow runs in surprisingly narrow branches as well as why the flow pattern is decorated by fringe spaced by $\lambda_F/2$ will be discussed in detail in Chapters 4 and 5. For now it is sufficient to notice that there are features which show that our scanning technique has surprisingly high resolution. Fringes spaced at about 19nm, decorate the entire image, and in many places the lateral widths of the current branches is also on the order of 20nm. From the calculations and measurements of Sections 3.2 and 3.3 and an operating height of 10nm, the expected perturbation FWHM is about 120nm. How is such high resolution obtained when the perturbation being used is over 6 times larger? A schematic illustrating this basic question is shown below in Figure 3.16.

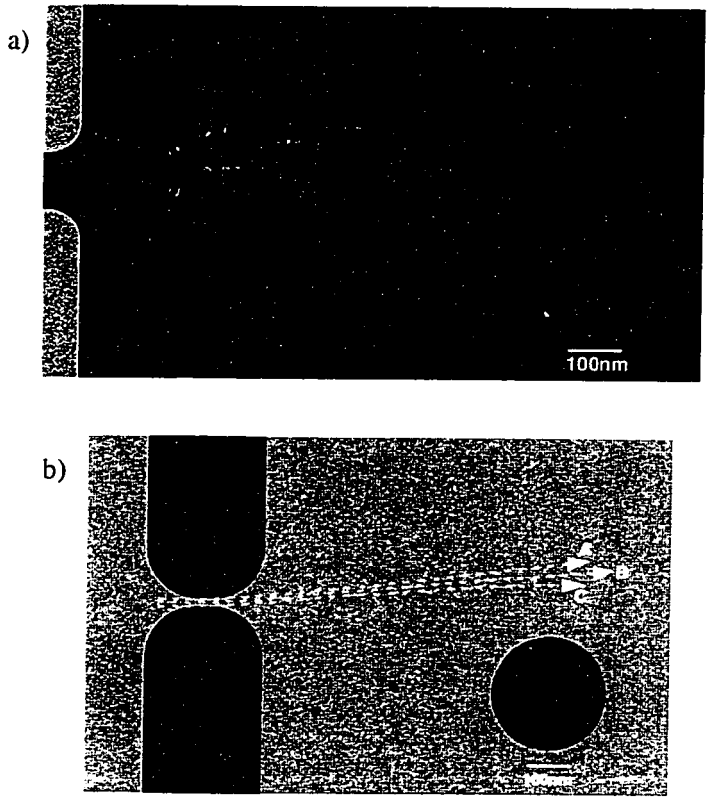

Figure 3.16 illustrates with both a picture of real data (a) and a schematic (b) the interesting problem of understanding how we can achieve such high resolution with a relatively blunt perturbation. a) shows the same data as in Figure 3.15 but with a dark circular region superimposed which represents the rough expected size of the tip perturbation. b) shows a simplified schematic with the current concentrated between paths A and C and a tip perturbation which will be used to image this current flow.

Figure 3.17 shows a schematic which explains why it is possible to achieve such high lateral resolution in our image. The observed resolution seems to be at least 20nm, while the expected width of the perturbation is estimated to be greater than 100nm. The reason for the surprisingly high lateral resolution is related to an effect which could be called the "christmas ornament effect" - if one shines a flashlight (the QPC) at a shiny round christmas bulb (the tip), one sees a very small spot much smaller than the diameter of the bulb. The key point is that light scatters off the entire ornament, but only light that hits the ornament straight on reflects back into an observer's eye, resulting in a very small reflection.

The same effect occurs when a tip is swept in front of a narrow feature in the flow (see Figure 3.17)- since the perturbation from the tip is circular, it will only backscatter the flow through the QPC (and hence change the conductance through the QPC) if it scatters a significant

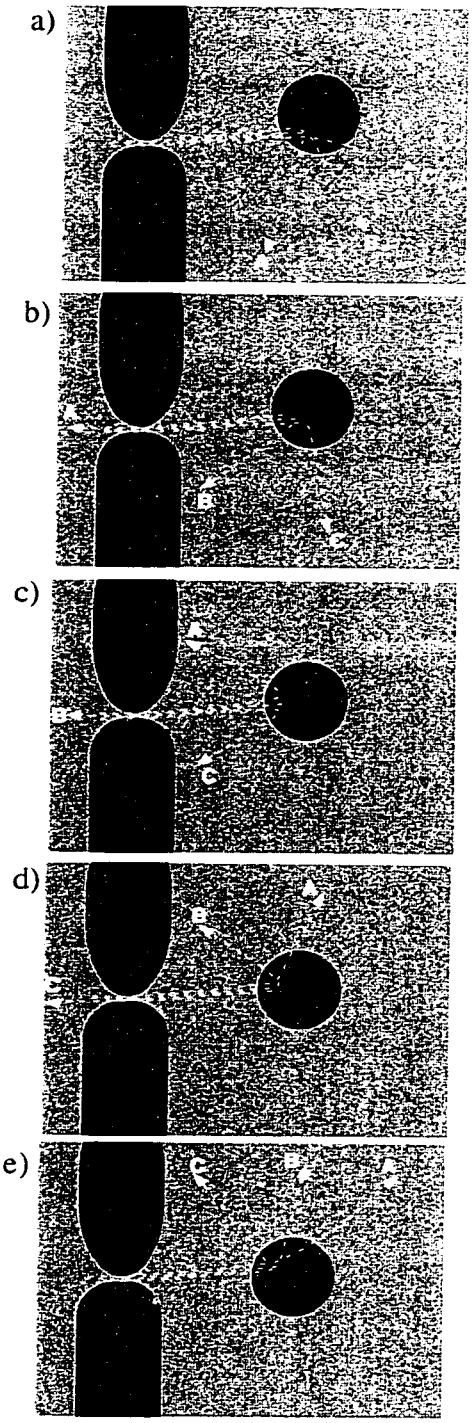

Figure 3.17 shows a tip-perturbation scattering a narrow beam of current as it is swept through the beam.

portion of the flow 180° back along the path on which it came from the QPC and straight back through the QPC. The only tip position in Figure 3.17 which will result in a strong change in conductance is the position in 3.17c, where the tip directly blocks the flow. In 3.17b and 3.17d the tip has just barely begun to backscatter some of the flow back through QPC, and has just begun to cause a change in the conductance through the QPC. In Figure 3.17a and 3.17b, even though the perturbation is blocking the flow, no change in conductance is observed because none of the scattered rays are backscattered through the QPC. Thus, features much smaller than the diameter of the tip perturbation can be faithfully reproduced using this method of imaging current. The key point is that in order for the tip to cause any signal, not only must it scatter the flow, it must backscatter the flow straight back through the QPC.

A similar line of reasoning illuminates why it is possible to have fringes perpendicular to the flow decorating images of flow which are separated by less than 20nm.

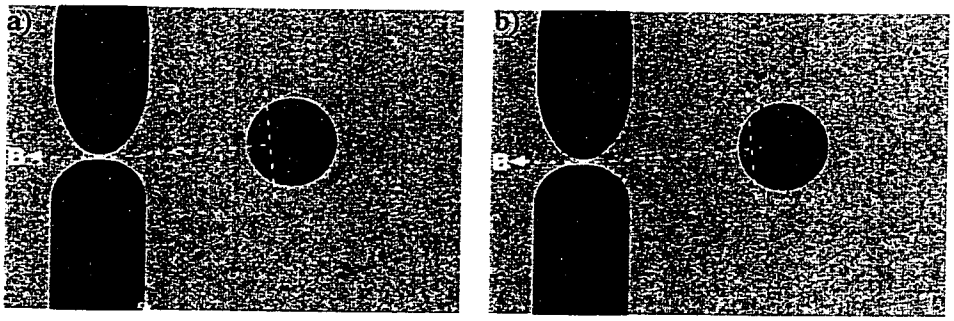

Figure 3.18 shows two tip positions and a backscattered semi-classical path from the QPC to tip and back. The tip is about 20nm further out in b) than in a). The yellow dashed line shows the turning point in a), while the red dashed line shows the turning point in b)

In our analysis of the origins of the fringes in Chapters 4 and 5 it will become apparent that these fringes are due to interference between straight round-trip paths between the tip and QPC with other paths the electrons can take- moving the tip by $\lambda_F/4$ causes the total interference between paths to shift from constructive to destructive. We are getting ahead of ourselves here, however. The essential point here, is that even though the perturbation is large and has long tails to it, there is one definite reflection point for a given tip position, (shown by the yellow and red lines in Figure 3.18). Even though the width of the perturbation is greater then 100nm, moving the tip by 10nm ($\lambda_F/4$) moves this classical turning point by 10nm as well.

Chapter 4

Imaging Electron Flow Through Individual Modes of a Quantum Point Contact

\

4.1 Introduction

The quantum point contact (QPC) is a centrally important device in the study of mesoscopics and two-dimensional electron gas (2DEG) physics. Since its experimental discovery in 1988[1,2] it has been a crucial element in many experiments, and indeed continues to be the subject of intense investigation. The fundamental origins of conductance quantization in a QPC are well understood[3], but many questions crucial to understanding real-world QPCs remain. In this chapter we discuss the results of bringing a powerful new imaging technique to bare on the study of QPCs which allows one, for the first time, to gather direct spatial images of electron flow through these devices.

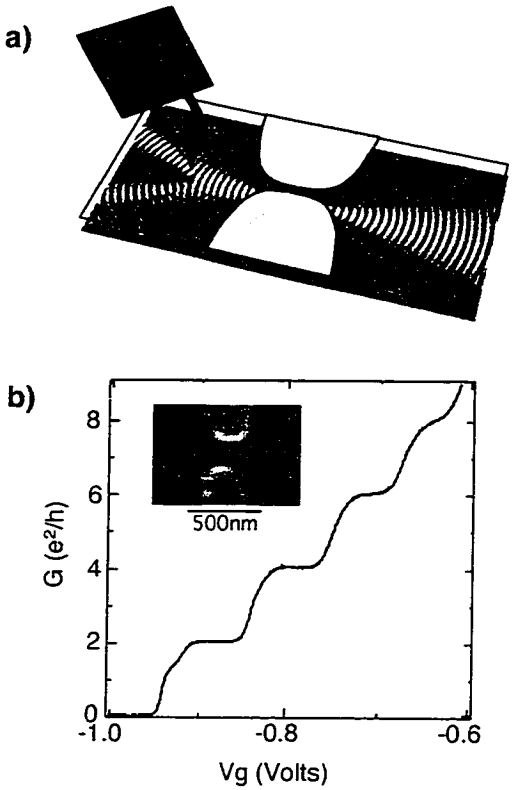

Figure 4.1a shows a schematic of the experimental setup used to image electron wave flow. b) shows the conductance curve and topography of one of the quantum point contacts (QPC) used.

1. B. J. van Wees et al., Phys. Rev. Lett. **60**, 848 (1988)
2. D. A. Wharam et al., J. Phys. C Solid State Phys. **21**, 209 (1988)
3. Reviewed in C. W. J. Beenakker and H. van Houten, Solid State Phys. **44**, 1 (1991)

Figure 4.1a shows the experimental technique used to image electron flow through a quantum point contact (QPC) and also the methods we use to define a QPC. The QPC is formed by negatively charging a pair of electrostatic surface gates to create depletion regions in the 2DEG below. These depletion regions define a variable width channel connecting the left and right 2DEG reservoirs. When the width of this channel is on the order of the Fermi wavelength λ_F, the conductance through the QPC becomes quantized in multiples of $2e^2/h$ as electrons flow through the wave functions of the lowest individual transverse modes. Figure 4.1b shows a conductance trace taken at 1.7K for the QPC used in these experiment as well as a topographic image of the electrostatic gates used to define a device. This device shows excellent conductance quantization, with all of the plateaus on the unperturbed device spaced by $2e^2/h$ +/- 0.5%.

Electron flow through the QPC is imaged by scanning a negatively charged AFM tip (shown in blue in Figure 4.1a) over the sample and simultaneously measuring the effect the tip has on the conductance of the QPC as a function of tip position. The tip creates a movable depletion disc beneath it which can backscatter electron waves. When the tip is over areas of relatively high electron flow from the QPC it will backscatter a relatively high flux of electron flow back through the QPC, thus decreasing the total conductance by a large amount. Conversely, when the tip is over areas of little or no electron flow, the depletion disc will not backscatter any flow back through the QPC, and the total conductance will be unchanged. By raster scanning the tip and compiling a map of conductance change vs. tip position, we are thus able to create an image of electron flow. (More information about this technique is given in Section 3.5 "Imaging Current - Tip as a Moveable Backscatterer")

It is helpful to briefly review some of the theory describing the operation of a quantum point contact before continuing on to the experimental results. A conductance curve and schematics showing the contributions to the electron flow at various point along the conductance curve are shown below in Figure 4.2.

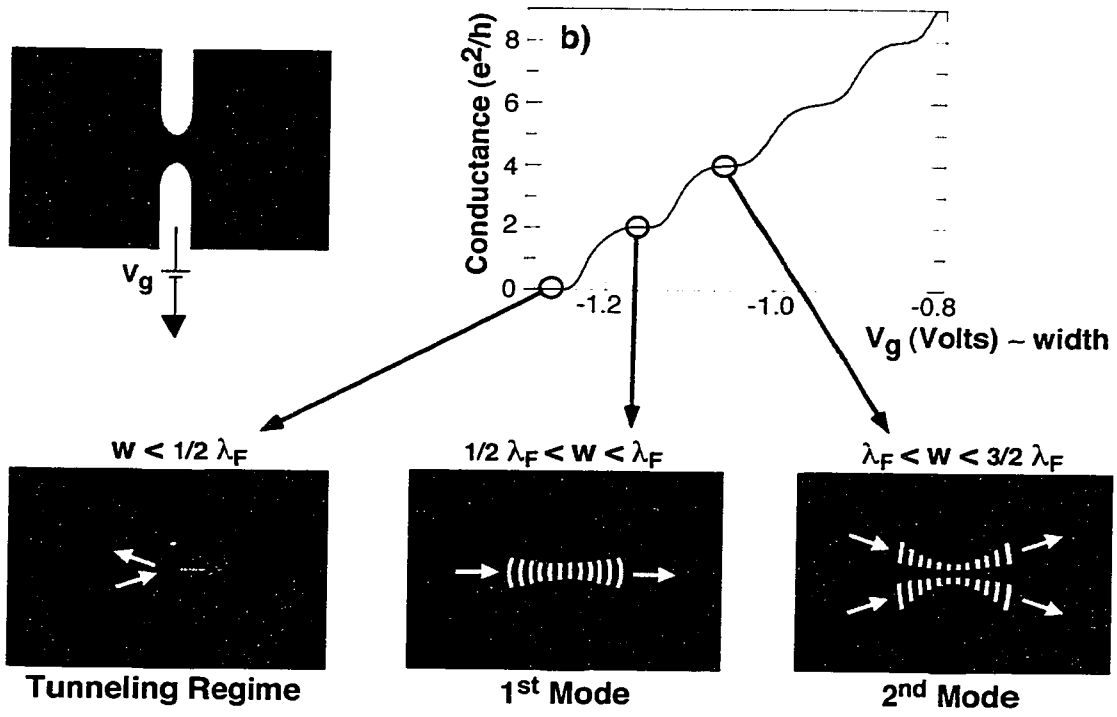

Figure 4.2 shows a schematic explaining the operation of a quantum point contact. a) shows a QPC with gates (yellow), a 2DEG (green) and depletion regions beneath the gates (black). b) shows a measured experimental QPC curve. c) shows current flow when the QPC is "pinched off" or closed so that only tunneling current may pass. d) shows the current through the first mode. e) shows the current through the second mode. At $G = 2e^2/h$, the current pattern will be that of the first mode (d), while for $G = 4e^2/h$, the current pattern will be that of the first and second modes, (d) + (e).

Fig. 4.2a shows a schematic of a QPC with electrostatic gates held at a negative voltage V_g, creating a variable width channel of width w in the 2DEG. Figure 4.2b shows the conductance experimentally measured on an actual QPC device while varying the gate

voltage V_g- essentially changing the width of the channel. When the width of the channel is less than 1/2 λ_F ($V_g \lesssim -1.25$V for this device), the QPC is in the "tunnelling regime" and the only current that flows is the current that tunnels through the pinched-off channel. This situation is shown schematically in Figure 4.2c. As the channel is widened by making the gate voltage less negative, the conductance jumps in steps of $2e^2/h$ with the addition of each new transverse mode. The conductance jumps from 0 to $2e^2/h$ when the channel is widened to between 1/2 λ_F and λ_F ($-1.20 \lesssim Vg \lesssim -1.13$). This corresponds to the first transverse mode, illustrated in Figure 4.2d, becoming energetically accessible to electrons at the Fermi energy. On this conductance plateau, the current will be concentrated along the axis of the QPC in one main lobe as in Figure 4.2d. The conductance jumps from $2e^2/h$ to $4e^2/h$ when the channel is further widened to between λ_F and 3/2 λ_F ($-1.10 \lesssim Vg \lesssim -1.03$). The current pattern on this plateau then is be a sum of the single lobed pattern of the first mode (4.2d) and the double lobed pattern of the second mode (4.2e). As the QPC is further widened, addition modal wavefunctions become energetically accessible, with the Nth mode in general having N lobes.

This chapter presents images of electron flow close in to the quantum point contact (less than 400nm from the opening)[4]. Section 4.2 presents images of current flow obtained on the QPC as it was opened from the first plateau ($G = 2e^2/h$) to the second ($G = 4e^2/h$) and third ($G = 6e^2/h$) plateaus. Strong coherent fringes perpendicular to the current flow decorate these images, and are discussed in Section 4.3. This section also discusses a method for washing these fringes out by using elevated ac drain-source bias

4.M. A. Topinka, et al., *Science* **289**, 2323 (2000)

voltages. The images of current flow at each conductance plateau are separated into their constituent modes in Section 4.4, which are seen to agree very well with theoretical predictions. Section 4.5 illustrates another way to use the tip - instead of scanning the tip and measuring its effect on the conductance, we can place the tip in a specific location, creating an artificial impurity, and measure this perturbed QPC's new conductance curve. A series of these tip placements and conductance curve measurements illustrates how we can selectively scatter either the 1st or 2nd mode and leave the other unperturbed. In another series of tip placements we show how one can directly measure the angular widening of the current flow as the QPC is opened from the 1st conductance plateau up all the way through the 8th conductance plateau.

4.2 Angular Patterns of Electron Flow from a QPC

Figure 4.3 shows experimental images of coherent electron flow from a quantum point contact biased on each of the first three conductance plateaus. These images are the first published two-dimensional spatial images of electron flow that directly show coherent electron wave flow from a QPC. Each image is composed of two separate scans - one to the left of the point contact and one to the right. The area near the gates was not scanned in order to avoid accidental contact between the charged tip and gates. In each scan, dark areas correspond to low electron flow, with colors and increasing height in the scans corresponding to higher electron flow.

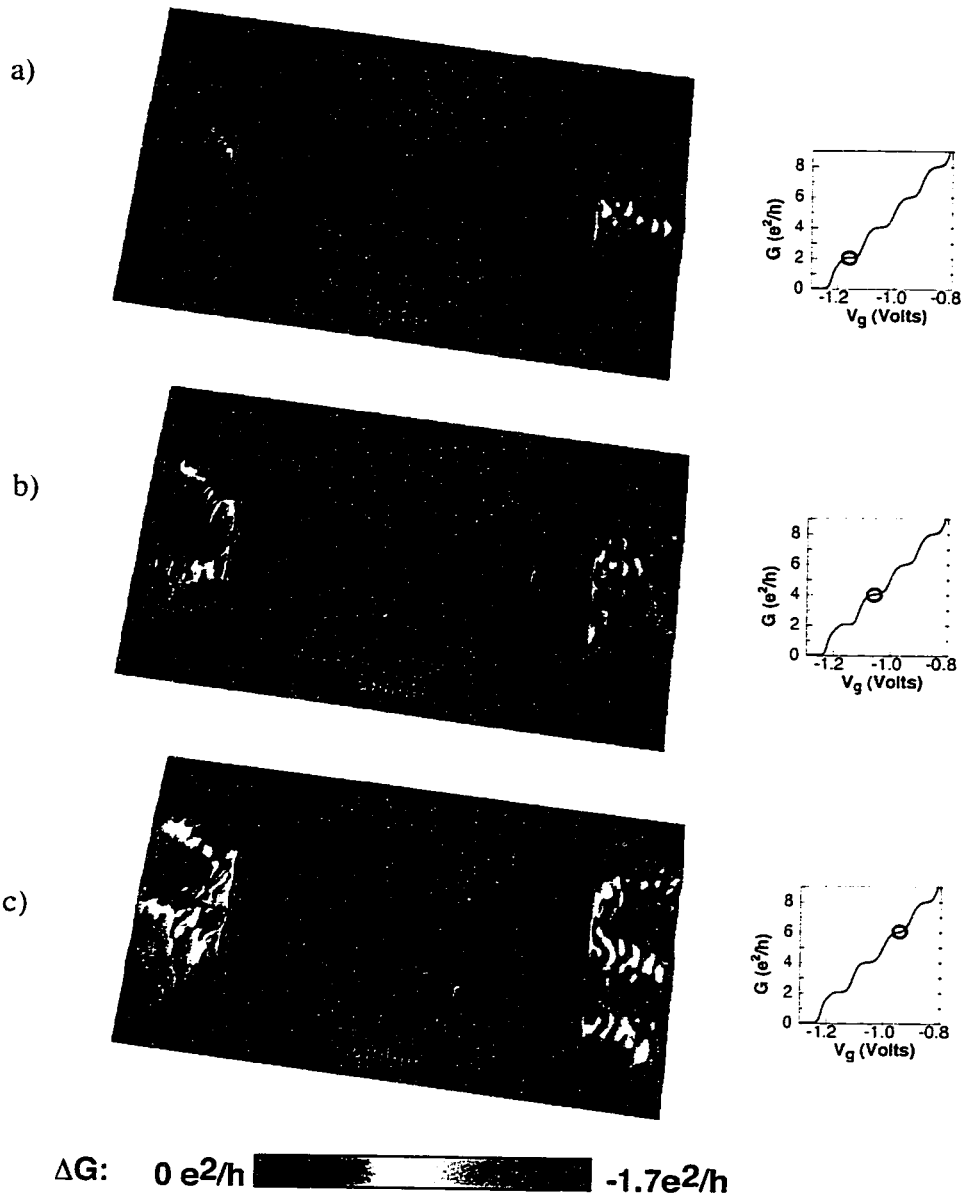

Figure 4.3 shows the electron flow from a QPC as it is opened from a) the first plateau ($G=2e^2/h$) through b) the second plateau ($G=4e^2/h$) and c) the third plateau ($G=6e^2/h$).

A number of interesting features are visible in these images. One clear feature is the changing and widening angular structure of electron flow as the QPC channel is widened. New angular lobes in the electron flow patterns appear at each step in the

conductance as a new mode through the QPC becomes energetically accessible. The current through the QPC on the first plateau (Figure 4.3a) is concentrated in one main lobe along the axis of the QPC in agreement with theory - the electronic wavefunction passing through the first transverse mode should also have a single lobe along the axis of the QPC. When the QPC is opened to the second plateau (Figure 4.3b), a two-lobed current pattern appears to be added on top of the single-lobed flow pattern from the 1st mode. This, again, agrees well with the simple theoretical explanation of flow through a QPC (see explanation of Figure 4.2). - the flow on a given plateau should be a linear addition of all the modes contributing to that plateau. When the QPC is opened to the third plateau (Figure 4.3c), a three-lobed current pattern appears on top of the flow already seen at the second plateau.

The electron flow patterns do not change appreciably along conductance plateaus; changes in flow occur only while moving up the steps between plateaus, where new transverse subbands become energetically accessible to electrons at the Fermi surface of the 2DEG. This observation is consistent with the theoretical picture that the flow through the QPC on each conductance plateau is a linear superposition of the flow through each of the constituent modes, and that the angular distribution of electron flow in each mode is unique.

The conclusion we reach, here, is that Figure 4.3a shows the current flowing through the 1st transverse mode (or wavefunction), Figure 4.3b shows the current flowing through the 1st transverse mode added on top of the current flowing through the 2nd transverse mode, and Figure 4.3c shows the current flowing through the 1st, 2nd, and 3rd

transverse modes, all added together. In Section 4.4 we separate these scans on each conductance plateau out into individual modal wavefunction patterns.

4.3 Coherent Fringes

A striking feature in the images of electron flow in Figure 4.3 is the appearance of fringes spaced by $\lambda_F/2$ that are oriented perpendicularly to the direction of current flow. These fringes can be understood in terms of alternating constructive and destructive interference between different semi-classical paths along which electrons can be backscattered through the QPC. Figure 4.4 shows a close-up of the fringes as well as a schematic representation of two such paths.

Figure 4.4 shows data with superimposed schematic electron paths illustrating the origin of the fringes seen running perpendicularly to the current flow. One possible round-trip taken by electrons travelling through the QPC is shown by the red path, while another interfering path is shown by the blue path.

One possible backscattered path is shown in Figure 4.4 as the red path, and consists of an electron passing through the QPC, striking the tip, and backscattering back through the QPC. A second path (there are many others not shown), passes through the QPC, strikes the tip, reflects off the gate, back to the tip, and finally passes back through the QPC. As the position of the tip changes, the total phase accumulated on these two paths change differently, and these paths can move from constructively to destructively interfering with each other.

The consequences of using electrons with a wider range of energies (similar to using hotter electrons) to measure electron flow are shown in Figure 4.5a to 4.5f.

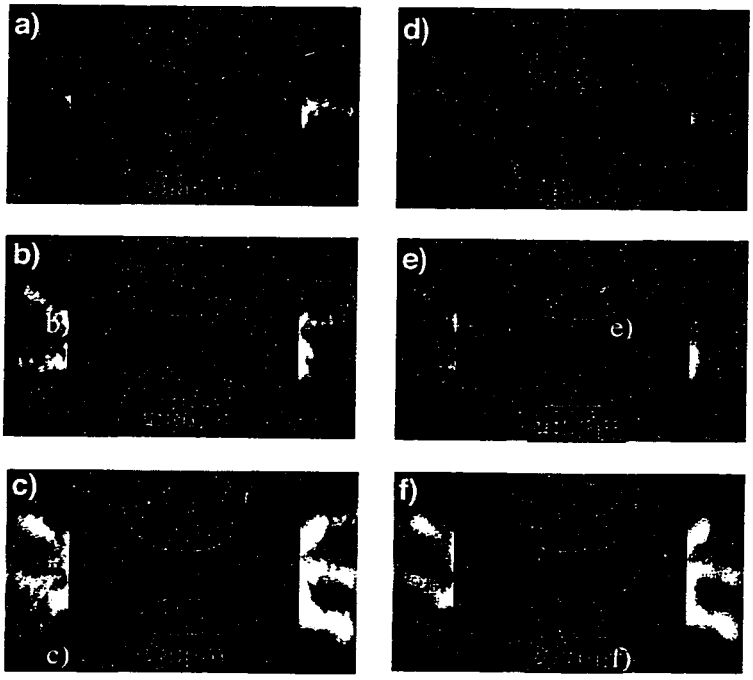

Figure 4.5 shows the effect of electron heating on images of flow: (a to c) show electron flow for the 1st, 2nd and 3rd conductance plateaus taken under the same conditions as Fig. 2A to 2C with low voltage 0.2 mV across the QPC; (d to f) show corresponding images for high voltage 3 mV across the QPC which causes electron heating. Heating destroys interference fringes, but leaves the angular pattern unchanged.

The left three images (Figs. 4.5a-4.5c) were taken at low drain-source bias voltage (0.2 mV ac across the QPC), while the right three images (Figs. 4.5d-4.5f) were taken at

higher drain-source bias voltage (3 mV ac). The net effect of using this higher bias voltage, (comparing 4.5d to 4.5a, 4.5e to 4.5b, and 4.5f to 4.5c) is to wash out the coherent fringes which decorate the low-bias voltage scans while leaving the overall envelope of current flow unchanged. Because in Figures 4.5d-4.5f we are using a range of electron energies from E_F-3mV all the way through E_F+3mV, we expect an effect similar in some ways to the effect from using hotter electrons since the electrons involved in transport now have up to 3meV, or 35K, of excess kinetic energy. The fact that the $\lambda_F/2$ fringes disappear with this high effective electron temperature is additional confirmation that they are due to coherent quantum interference. The angular envelope of electron flow, however, remains unchanged (Figs. 4.5d-4.5f). In Section 4.4 we will use these images of the envelope of the electron flow without the decorating coherent fringes (using high drain-source voltages, V_{ds}=3mV) to extract the angular contribution of electron flow from each transverse mode.

4.4 Angular Distribution of Electron Flow thru Individual Modes

Figures 4.6 shows images of the angular pattern of electron flow from the 1st, 2nd, and 3rd transverse modes of the QPC.

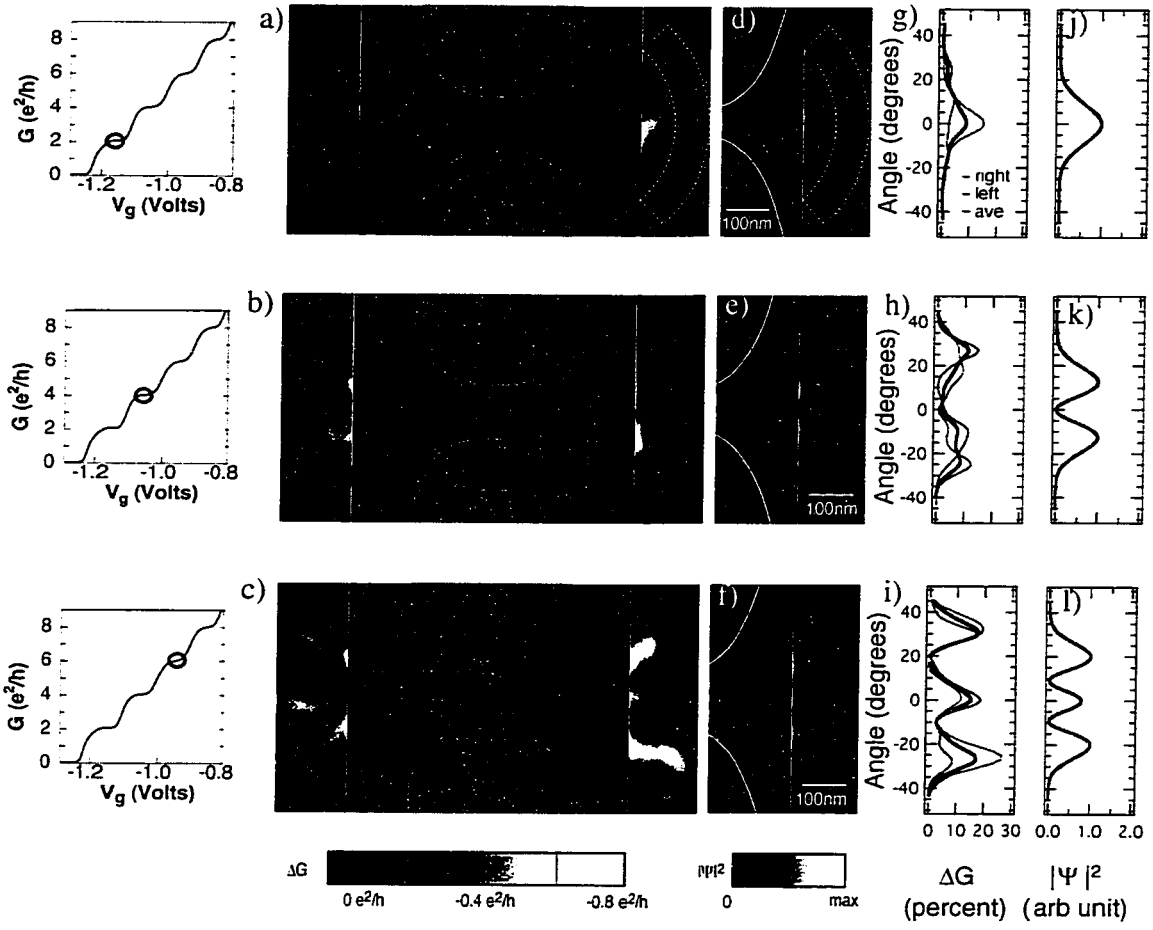

Figure 4.6 The measured images of electron flow through the first, second, and third mode of the QPC. Figures (a) to (c) show the measured angular distribution of the electron flow through the first three transverse modes of the QPC. Figures (d) to (f) show calculations for the angular distribution of the electron flow through the QPC, Figures (g) to (i) show the measured angular profile of the electron flow, and (j) to (l) show the theoretical angular profile of the electron flow.

Figures 4.6a, 4.6b, and 4.6c show the experimentally measured flow patterns through the first, second, and third transverse modes, respectively. These images agree

remarkably well with our simple expectations for flow through the different modes outlined at the beginning of the chapter, that the electron flow through the Nth mode in general has N lobes. Figs. 4.6d to 4.6f show the results of exact quantum mechanical simulations for flow through each of the first three transverse modes[5]. The agreement between the measured modal flow patterns (Figs. 4.6a to 4.6c) and the exact theoretically predicted modal patterns (Figs. 4.6d to 4.6f) is excellent. In both theory and experiment the electron flow through the Nth mode in general has N lobes. This result makes intuitive sense, because the same is true for the wave functions of electrons travelling through the QPC itself - electronic wave functions passing from the Nth mode in a point contact have N maxima (or lobes) in $|\Psi|^2$. Also, the angular extent of each mode widens significantly from one mode to the next in both experiment and theory.

The images of flow from individual modes (Figs. 4.6a to 4.6c) are obtained by subtracting images of total electron flow on different conductance plateaus (Figs. 4.5d to 4.5f) from each other. Fig.4.6a is particularly simple- because only the first mode is conducting when the QPC is biased at $G = 2e^2/h$, Fig.4.5d (the image of flow through the QPC at $G = 2e^2/h$) turns out to also be a direct image of the first mode - Figs.4.5d and 4.6a are identical. Fig. 4.6b (electron flow from only the 2nd mode) was obtained by subtracting Fig. 4.5d (electron flow from the 1st mode) from Fig. 4.5e (electron flow from the 1st and 2nd modes). Likewise, Fig. 4.6c (electron flow from just the 3rd mode)

5.Scot Shaw in Prof. Rick Heller's group performed the exact quantum mechanical simulations for the flow through the lowest three modes plotted in Figs.4.6d to 4.6f The color scale represents the amplitude $|\Psi|^2$ of the wave function. For these calculations the transverse potential of the QPC was parabolic, with varying curvature to produce an electron gas channel approximating the lithographic shape of the gates; the white curves in Figs. 4.6d to 4.6f show where the potential crosses the Fermi energy. To ease comparison, areas not scanned in the experiment are dimmed in the simulation.

was obtained by subtracting Fig. 4.5e (electron flow from the 1st and 2nd modes) from Fig. 4.5f (electron flow from the 1st, 2nd and 3rd modes). The underlying assumption here is that current flow at a particular conductance plateau is a linear superposition of all the modes that are each contributing $2e^2/h$ of conductance to that plateau.

Figures 4.6g to 4.6i plot the angular distribution of measured electron flow in Figs. 4.6a to 4.6c. The circular slice used to determine the distribution is shown on the right side of Fig. 4.6a. Figures 4.6j to 4.6l plot the angular distribution of electron wave functions $|\Psi|^2$ from Figs. 4.6d to 4.6f taken using a circular slice shown in Fig. 4.6d. Comparison shows a high degree of agreement between theory and experiment. The measured angular dependencies of images and theory have the same modal structure, N lobes for the Nth transverse mode, and they agree quite well in shape. Even the amount of spreading between the 1st and 2nd, and 2nd and 3rd modes agrees quite well. It should be noted that no effort was made to engineer the potential used in the simulation to match experimental results. The match between experiment and theory with regards to the total angular width of each modal pattern could probably be made very good through a small amount of tinkering with the precise form of the potential used in the simulations- the faster the potential defining the channel in the simulations is made to open, the more spread out the current flow pattern becomes due to diffraction. We have decided to resist adding a fitting parameter to these simulations for now, however.

It is worth noting here, (and some may already have noticed), that the experimental images of flow through the individual modes (Figs. 4.6a to 4.6c), lack the coherent fringes visible in Figure 4.3. These fringes have been purposely blurred away by using the high drain-source bias voltage measurements (Figs 4.5d to 4.5f) to derive the modal

flow instead of the low drain-source bias voltage measurements (Figs. 4.5a to 4.5c). This was done because here we are interested in the underlying electron flow patterns through the modes and not in the coherent fringes from interference off of the tip which can decorate our images.

The remarkable agreement between theory and experiment seen in Figure 4.6 shows that our technique for imaging coherent electron flow works, and that our understanding of the imaging mechanisms involved (presented in Chapter 3) are accurate. These images of the actual modal patterns of electron flow through a quantum point contact show for the first time that close in to the QPC flow through the Nth mode has N lobes (in agreement with theory). This fundamental feature of the modal patterns appears to survive the effects of impurities, defects, inhomogeneities in the donor layer. Does this relationship continue to hold for electron flow further out from the QPC? The question of what happens to the flow further out into the bulk is the subject of Chapter 5.

4.5 Selective Mode Scattering - The Tip as a Positionable Impurity

In this section we switch gears slightly from the scanning methods of the earlier sections and will instead be "parking" the tip at a given location and taking conductance vs. gate voltage measurement. This allows us to study the effect of introducing what is essentially a very large impurity (the depletion region below the tip). One of the motivations for operating in this mode is that it allows us to clearly identify one possible source for imperfect conductance quantization - variations in the height of conductance steps from $2e^2/h$ have been observed in many papers and assigned to various

mechanisms[6.7.8]. Using the tip as a movable impurity we investigate one mechanism that can cause variations in conductance step heights; the scattering of electrons from impurities or defects which decreases the transmission of individual modes.

Figure 4.7 shows that the height of the Nth conductance plateau can be changed when the negatively charged AFM tip is held at a fixed position above the electron flow pattern from the Nth mode of the QPC.

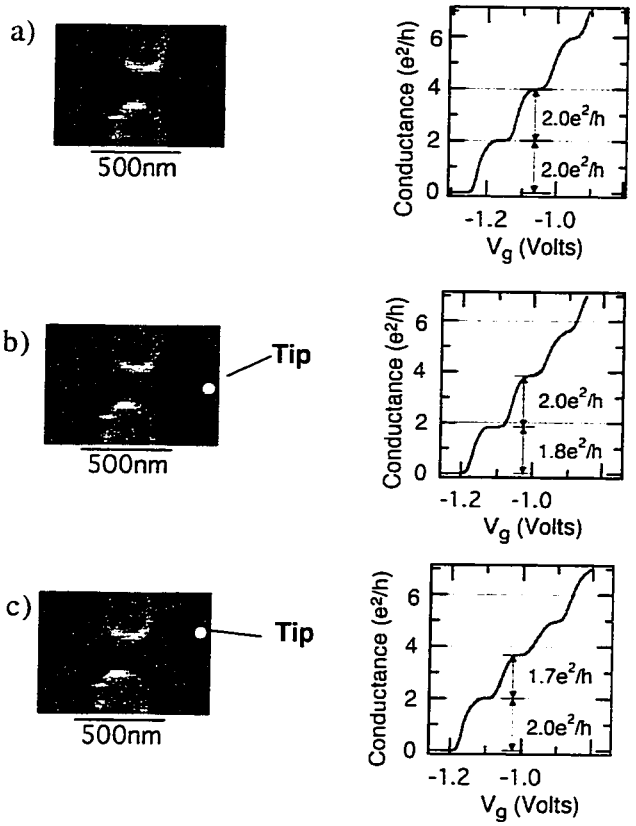

Figure 4.7 The selective effect of the AFM tip on conductance plateaus of the QPC (the small gray circle indicates the position of the tip): a) conductance plateaus with no AFM tip, b) suppression of the 1st conduction plateau when the AFM tip is located directly in front of the QPC, blocking the electron flow from the 1st mode, c) suppression of the 2nd conductance plateau when the tip is located 15° off the axis of the QPC, blocking electron flow from the 2nd mode.

---

6. Bruus, H.; Cheianov, V.V.; Flensberg, K., "The anomalous 0.5 and 0.7 conductance plateaus in quantum point contacts", *Physica E* **10** 97 (2001)

7.Thomas, K.J. et al. "Interaction effects in a one-dimensional constriction." *Phys. Rev. B* **58**, 4846 (1998)

8.S. Cronenwett, et al., submitted to Science October 2001.

When no tip is present in Fig. 4.7a, each transverse mode contributes $2e^2/h$ of conductance and all the conductance plateaus lie within 0.5% of integral multiples of $2e^2h$. When the tip is placed directly in front of the QPC in Fig. 4.7b, it backscatters electrons from the 1st mode without backscattering electrons from the 2nd. This reduces the entire 1st plateau to $1.8e^2/h$ without changing the spacing between the 1st and 2nd plateaus (the 2nd plateau lies at $3.8e^2/h$). When the tip is placed off axis as in Fig. 4.7c, it backscatters electrons from the 2nd mode without backscattering electrons from the 1st. This reduces the spacing between the 1st and 2nd plateaus to $1.7e^2/h$ without affecting the height of the 1st plateau. It is helpful when thinking about these measurements to refer back to the measured flow patterns of the 1st and 2nd modes in Figures 4.6a and 4.6b. The tip position in Figure 4.7b lies directly in the path of the 1st mode (Figure 4.6a), while lying in a zero of the 2nd mode (Figure 4.6b). Likewise, the tip position in Figure 4.7c lies outside the flow through the 1st mode (Figure 4.6a) while lying squarely in the path of one of the lobes of the 2nd mode (Figure 4.6b).

This set of measurements sheds light on a common occurrence in the study of quantum point contacts. Many QPCs, especially if they are part of a larger more complicated structure such as a resonator or a dot, exhibit conductance plateaus which do not fall exactly on integral multiples of the conductance quantum, $2e^2/h$. This result supports a satisfying intuitive picture for why this is sometimes the case: if an impurity or defect (or inhomogeneity in the donor distribution) which is strong enough or sharp enough to cause backscattering of electrons at the Fermi level lies in the path of the wave function through the Nth mode of the QPC, then that plateau will be suppressed beneath

$2e^2/h$. It will not, however, affect the transmission of modes whose wave functions, $\Psi(r)$, do not have an appreciable flow through that spot.

Quantum point contacts are robust against relatively high levels of disorder- as shown in Section 3.4 "Tip as a Moveable Gate" conductance quantization is preserved despite the presence of a relatively strong perturbation even directly in front of the QPC so long as that perturbation is not strong enough to actually backscatter electron waves. What we have seen in this section, however, is that if the scatterer is strong enough to actually backscatter the flow back towards the quantum point contact (i.e. if it is strong enough to create a depletion region), and it lies directly in the current path, then is does strongly affect the transmission coefficient of electrons travelling through that mode.

Another measurement that can be done using the tip as positionable scatterer is to take a series of QPC conductance curves, starting with the scatterer at a large angle to the QPC and moving inwards until the scatterer lies directly in front of the QPC. This series of measurements is shown below in Figure 4.8. By observing which modes are unaffected at each tip placement, one can directly observe the narrowing angular width of successively lower modes from the QPC. All modes which have a wave function with an angular cone which lies inside the placement of the artificial impurity will be unaffected and will thus each contribute $2e^2/h$ to the total conductance. The first mode which is blocked by the artificial impurity will be suppressed below $2e^2/h$. By slowly moving the tip in, starting at approximately 40° (Figure 4.8a) and progressing inwards in steps of about 5° each until the tip is directly in front of the QPC (Figure 4.8h), we can gauge the angular spread of each of the first seven modes.

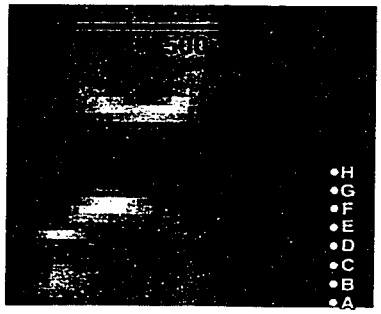

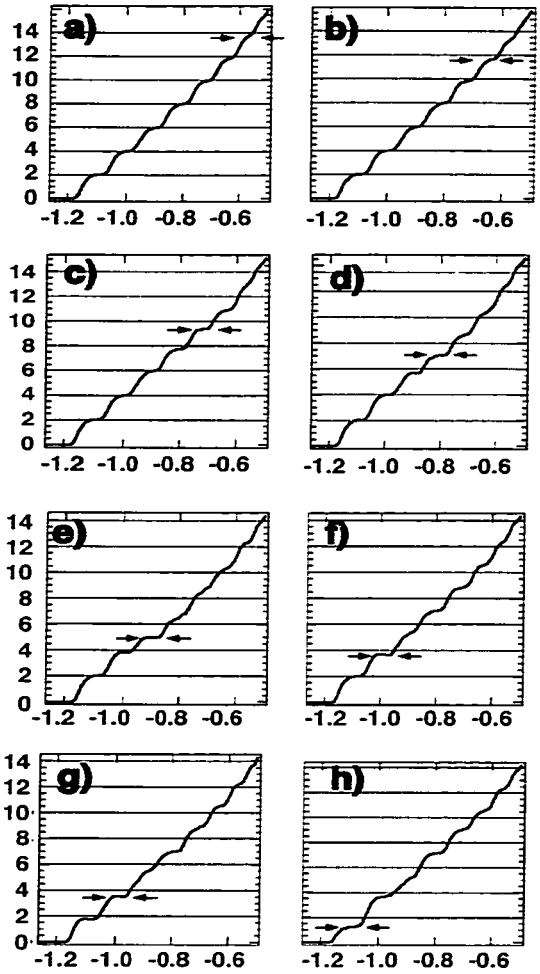

Figure 4.8 Widening angular pattern of the first through seventh modes from the QPC. The arrows in Figures a) through h) indicate the first plateau which is suppressed by at least $0.4e^2/h$ from its full value.

When the tip is placed at a large angle to the QPC (point A and Figure a), the first six plateaus are all at or near their unperturbed value and only the seventh plateau is significantly suppressed. As the tip moves in towards the axis of the QPC, the first affected mode moves downward one by one until finally in Figure h (with tip at point H), the 1st plateau is significantly suppressed. Interestingly, for this device there seems to be a linear relationship between mode number and mode width- the Nth mode has a roughly (5°)N angular spread.

Chapter 5

Imaging Branched Electron Flow Far From a Quantum Point Contact

5.1 Introduction

Figure 5.1 illustrate the fundamental question addressed by this chapter: what does the electron flow pattern far from a quantum point contact (QPC) look like? Figure 5.1a is a schematic showing the current pattern for the 1st mode as it travels out into an idealized 2DEG (infinite mobility) far from the QPC- the current stays in one central lobe which slowly widens as it travels away from the QPC. Figure 5.1b shows one guess for what happens to the 1st mode in an actual real-world QPC with scattering by dopant atoms and impurities - here the bumps and dips in the effective potential that the electron must pass over (due to

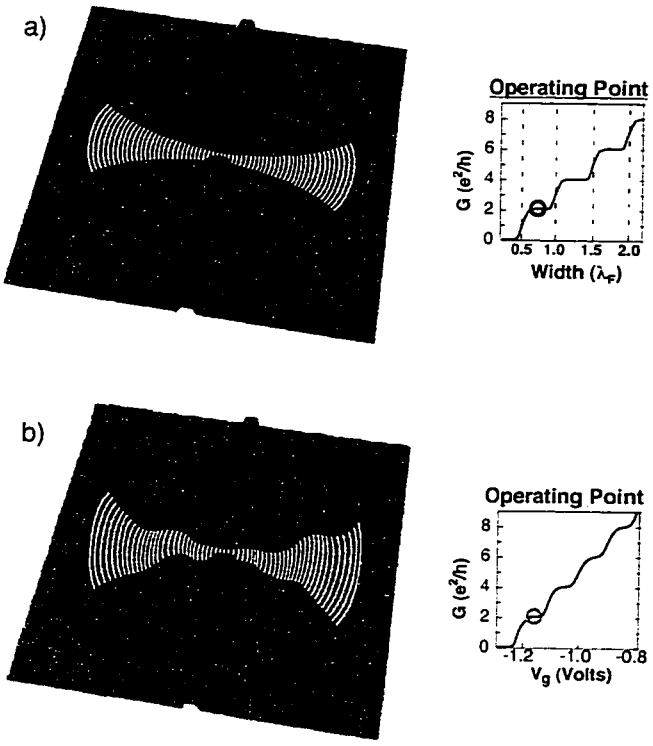

Figure 5.1 illustrates the basic question addressed in this chapter - what does the coherent flow far from a QPC look like? a) shows coherent electron flow through the first mode a quantum point contact over a large area around the QPC in an idealized (infinite mobility) 2DEG. b) shows one possible guess for the effect of finite mobility (a bumpy effective potential from defects, impurities, etc.) on this flow. Here the disorder simply causes a quicker broadening and fanning out of the flow. Actual flow is radically different than this picture, however.

impurities, donor atoms, etc.) are seen to bend and distort the idealized flow pattern of Fig. 5.1a, but not to fundamentally alter its appearance. Previous to these experiments, little was known of what the electron flow patterns far away from a QPC actually looked like. The results presented in this chapter show that the actual current flow far from a QPC contains very interesting and important differences from this simple expectation shown in Fig. 5.1b.

Section 5.2 presents the experimental images of this flow, where, contrary to the simplest expectations shown in Figure 5.1b, striking and unexpected narrow branching is seen to occur - the electron flow forms persistent, narrow, branching channels rather than smoothly spreading fans. Section 5.3 presents quantum and classical simulations performed by Prof. Eric Heller s group which successfully reproduce the observed branching behavior. These simulations incorporate electron scattering by impurities and donor atoms in the 2DEG crystal. Section 5.4 discusses further theoretical study of this flow, which shows that the observed channels are not due to deep valleys in the potential, but rather are caused by the indirect cumulative effect of small angle scattering. Section 5.5 discusses a statistical measure of this branched flow and confirms that this surprising new information about flow through a 2DEG is still consistent with simple statistical measures of flow such the fact that the flux should fall off as 1/r with radius. Section 5.6 details and discusses the surprising persistence of fringes spaced by $\lambda_F/2$ throughout the entire scan range. Finally, Section 5.7 discusses several additional observations of interesting and surprising features in the electron flow far from a QPC.

5.2 Discovery of Branched Electron Flow

Figures 5.2a and 5.2b show images of electron flow from two different quantum point contacts at the temperature T=1.7K; both QPCs are biased on the $G = 2e^2/h$ conductance plateau.

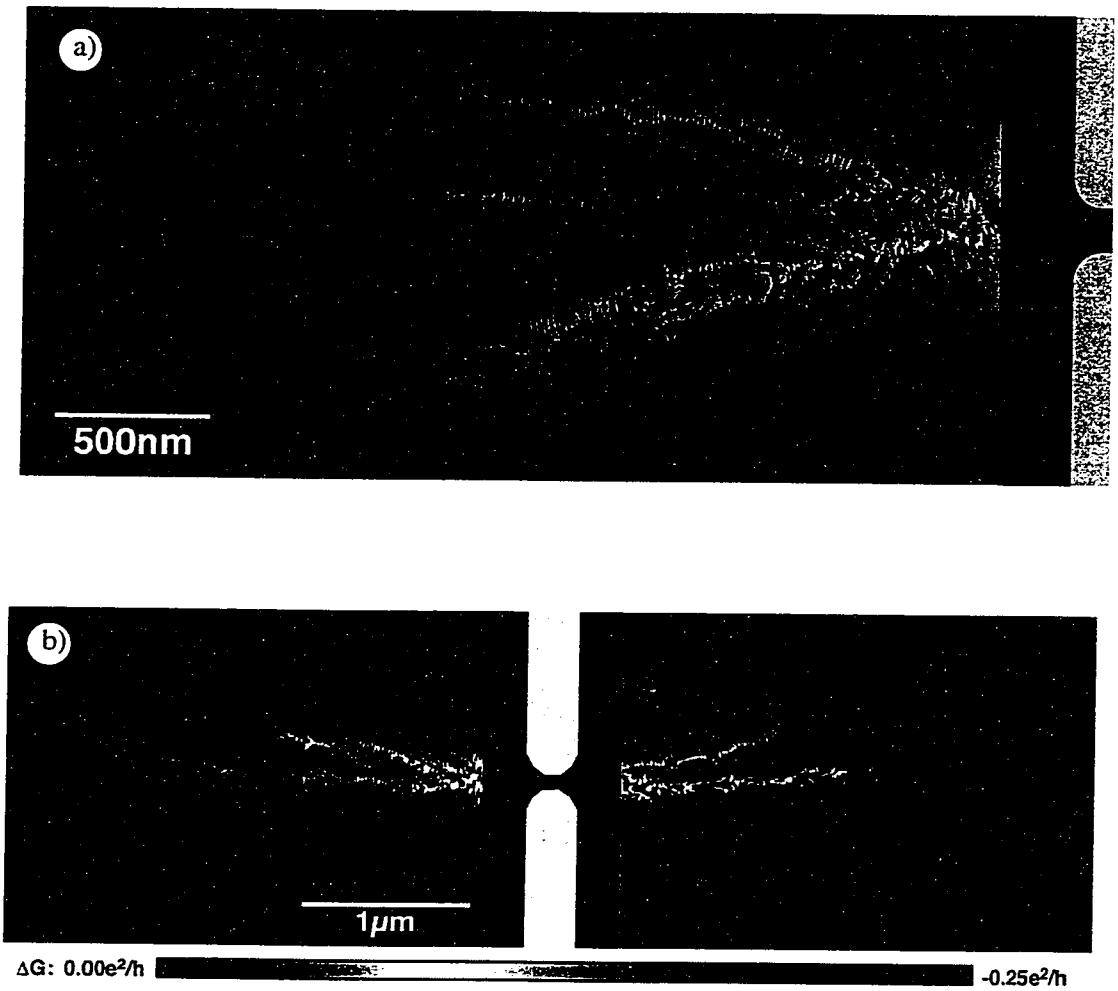

Figure 5.2 Experimental images of electron flow from two different QPCs. Figure a) shows a closeup of current flowing on one side of a QPC, and b) shows an image of flow on both sides of a different QPC. In both figures the QPCs are biased on the $G = 2e^2/h$ conductance step at T = 1.7K. Dark regions correspond to areas where the tip had little effect on QPC conductance, and hence are areas of low electron flow. The color varies and the height in the scan increases with increasing electron flow. Narrow branching channels of electron flow are visible, and fringes spaced by $\lambda_F/2$, half the Fermi wavelength, are seen to persist across the entire widths of both scans.

Figure 5.2b shows the flow patterns on both sides of a quantum point contact (the gated region at the center was not scanned), and Figure 5.2a shows a higher-resolution image of flow from one side of a different QPC. In both these images, the electron flow exits the point contact concentrated along the central axis, as one would be expected from a quantum-mechanical calculation of electron flow through an idealized QPC without impurities or non-uniform distributions of dopant atoms. Rather than continuing out as a smoothly widening fan, however, it quickly forks into several different paths and continues to branch off into smaller rivulets for the full width of both scans. There are many places directly in front of the QPC which, surprisingly, seem to be receiving almost no current whatsoever. Instead all the current seems to be concentrated along narrow branches which, interestingly enough, *stay narrow* throughout the entire width of the scan.

This strong branching behavior has been observed in all of more than twenty QPC exit patterns (eight devices with two sides per device, including multiple cool-downs over several samples) observed so far. Until now high-resolution, detailed images of electron flow from a quantum point contact have been difficult to obtain, and no observations of this type of strong branching behavior have been published.

It is interesting to note here that these current patterns are independent of the polarity of the drain-source bias voltage. The measurements presented here are taken using ac lock-in techniques (to improve signal to noise), but exactly the same image of electron flow would be found if a dc measurement were performed with electrons flowing left to right *or* right to left. This is understandable from a theoretical perspective because any quantum mechanical eigenstate will have a time reversed twin (so long as no magnetic fields are present)[1].

Another remarkable feature of these images is that coherent fringes similar in appearance to those seen in Chapter 4 and discussed in Section 4.3 decorate the current flow images for the entire width the scans. This observation is additional confirmation that our apparatus is imaging coherent electron flow. These fringes are the subject of Section 5.6 "Persistent Coherent Fringe".

It is interesting to ask whether or not the simple relation between the mode number and the number of lobes in the angular pattern of flow confirmed for close in to a QPC in Section 4.4 applies in the unexpected new regime of branched current flow found far from a QPC. Figure 5.3 shows a series of images of flow through a QPC that show the flow patterns for the first four transverse modes of that QPC.

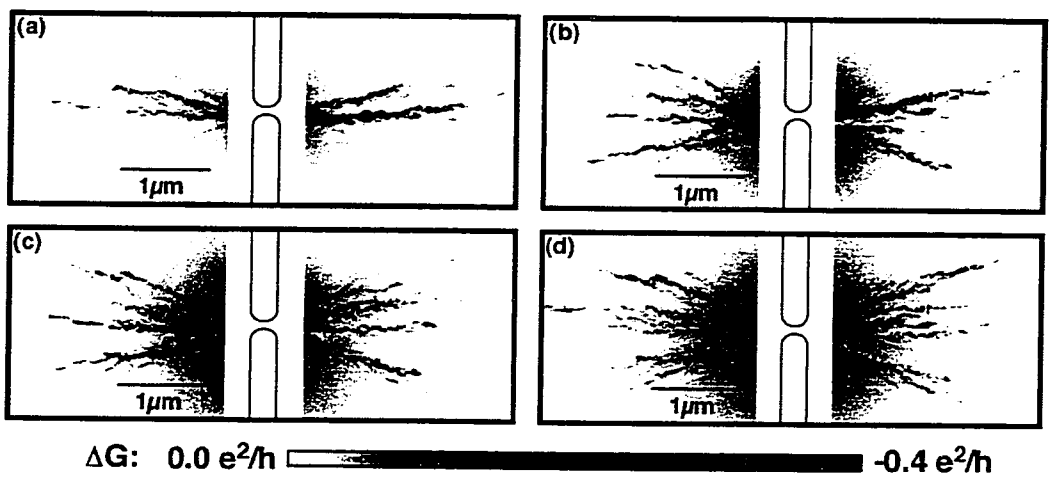

Figure 5.3 Images showing the branching behavior of the current flow from the (a) first, (b) second, (c) third and (d) fourth mode of a QPC. The branches are formed by the cumulative effect of passing over many small bumps and dips in the potential. Each modal image was extracted from the raw images of flow on the first four plateaus by the same method as was used in Figure 4.6 on page 88 and described on page 90.

1.Being experimentalists, we have also seen fit to test this assertion experimentally and have found it to be true.

Figure 5.3 shows images of electron flow through each of the first four transverse modes through a QPC. The same striking branching behavior noted in Figures 5.1 and 5.2 is present in these images. Figure 5.3a is an image of the electron flow through the first mode of the QPC, $G = 2e^2/h$. As in Figure 5.2, the electrons enter and exit the QPC in one main branch oriented roughly along the axis of the QPC, but then quickly fork into several narrow rivulets further from the QPC that themselves continue to fork throughout the scan. Comparing the first mode (Fig. 5.3a) to the second mode (5.3b) we see that in moving to the second mode the current pattern widens and new branches of current appear. This is in agreement with the theoretical results presented in Chapter 4 where the angular width of a modal pattern was found to increase with increasing mode number (see Figs 4.6d - 4.6f). We note here, however, that further out from the QPC (where these scans are taken) the presence of impurities and dopant atoms complicates the simple relationship between mode number and number of lobes found in Chapter 4. It appears that each of the lobes found close in to the QPC quickly branches and forks into sub-branches, complicating the simpler relationship between mode number and number of lobes closer in to the QPC. Figures 5.3c and 5.3d show the pattern for the third and fourth modes, respectively. Here, again, the patterns widens as we step up to higher modes, and new electron flow branches appear.

The scans in figures 5.2 and 5.3 start around the same distance from the QPC as the outer limits of the modal images in Chapter 4. We can see from Figure 5.3 that there is still some concentration of current along the axis close to the QPC for the 1st mode, while for the 2nd mode the current appears to spread out in more or less of a bi-lobed pattern, but the simple relationship between mode number and number of lobes found in

Chapter 4 seems to be complicated by the presence of impurities and dopant atoms when we look at electron flow further from the QPC as we are doing here. The details of where and exactly how many branches there are in each mode at large distances (greater than 500nm) from the QPC appears to be more dictated by the details of the donor and impurity configuration for that particular device than by the mode number.

It is interesting to note that in all of these images the current forms branches which quickly split into new branches even though the distance from the QPC is much less than a mean free path- the mean free path in this sample is 11μm, while the entire widths of these images is about 3 to 4μm. Another interesting experimental observation is that the branches seen in these images do not widen as one moves away from the QPC. Instead, new branches split off from the main branch, but the overall width of each branch stays quite narrow. It is also worth mentioning here that these patterns of electron flow, like the patterns of electron flow presented in Chapter 4, are completely reproducible during a cool down. We have left samples cold in the dewar for almost a month with absolutely no observed changes occurring in the flow pattern - they are completely steady (down to every last fringe) from scan to scan as long as the sample is kept cold and the tip doesn't come into physical contact with the surface. There are a few other traumatic events which can change the current pattern, such as using a large positive tip voltage, or using an extremely large drain-source bias voltage (greater than about 10mV or so).

5.3 Modeling Flow Far From a QPC

Prof. Eric Heller's group has performed detailed simulations and calculations aimed at understanding the surprising experimental observation of branched flow[2]. They have numerically calculated the set of conducting wavefunctions through a quantum point contact with a disordered background potential, and have also performed classical simulations of electron flow through that same potential. Their model for the potential landscape incorporates sources of disorder found in real-world GaAs/AlGaAs 2DEGs heterostructures and uses the known physical parameters of our sample. There are two contributions to the disordered background potential they use in their simulations: the donor dopant atoms located in a δ-layer set back 22nm from the 2DEG, and unwanted impurities sprinkled randomly throughout the crystal (a density of 1.25×10^{15} / cm^3 was found to give the appropriate mobility).

Figure 5.4 shows the results of classical and quantum mechanical simulations of electron flow through a QPC and the surrounding disordered potential. Figure 5.4a shows the potential used for the classical simulation (5.4b) as well as the quantum mechanical simulation (5.4c). The agreement between the classical and quantum results is very good, leading to the conclusion that the branched flow is essentially a phenomenon understandable in terms of classical electron motion. The "shadow" in Figure 5.4a, cast by the classical flux simulations from Figure 5.4b, demonstrates that channeling is not simply caused by large valleys in the potential. Bumps in the potential which cause channeling are well below the Fermi energy of the electrons, so the flow does not represent the only energetically available paths. The current paths do not simply

---

2.M. A. Topinka. et al., "Coherent branched flow in a two-dimensional electron gas." *Nature* **410**. 183 (2001)

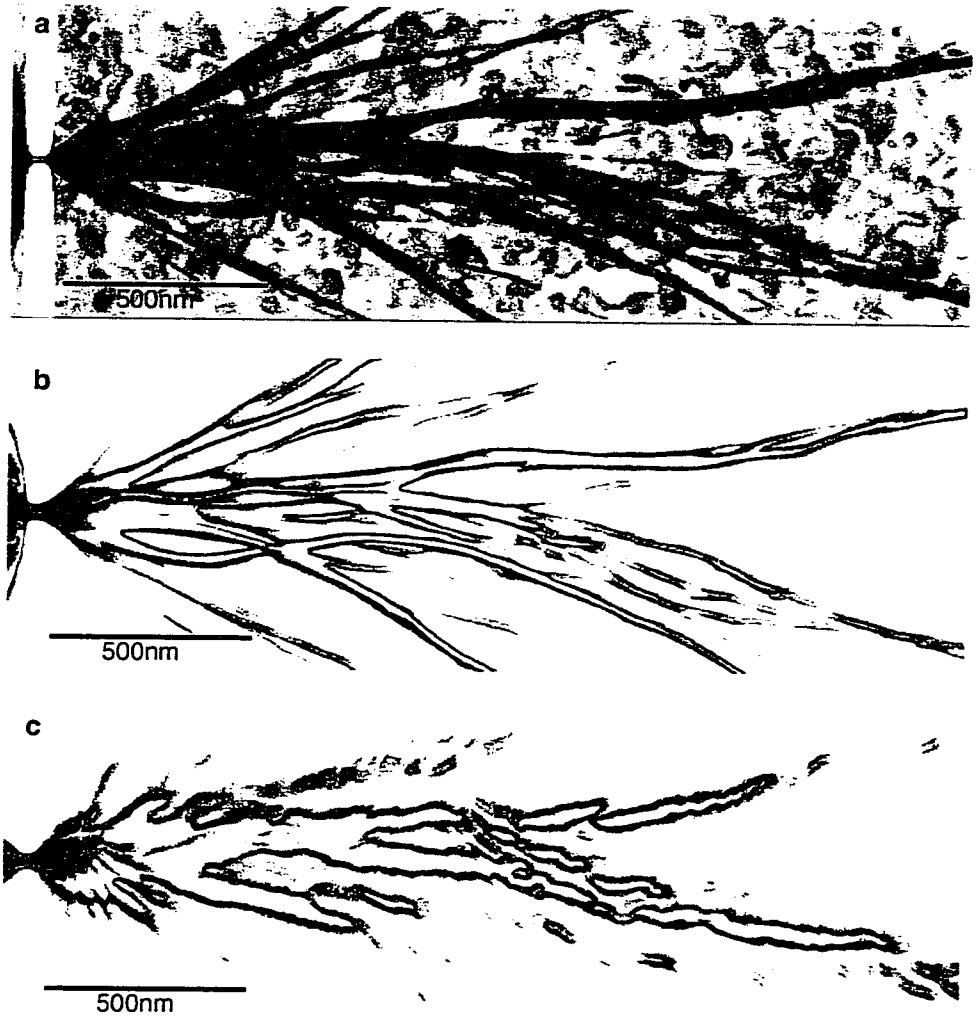

Figure 5.4 shows calculations done by Prof. Rick Heller's group for both classical and quantum mechanical electron flow through a QPC based in a realistic effective potential. a) shows the potential used in these simulations. A shadow of the classical flow is superimposed over the potential to emphasize that the electrons flow straight over bumps and dips in the potential. b) shows the classical simulations of electron flow, and c) shows the quantum mechanical simulation of electron flow.

follow low potential routes which guide the current as a valley would guide a river. The explanation for this striking branching behavior seen now in both experiment and theory is the subject of the next section.

5.4 Understanding Branched Flow

The mechanism (discovered by Eric Heller s group) behind the formation of branched flow seen in these long range scans has turned out to be essentially a classical one. The branches are formed by the cumulative effect of electron trajectories being slightly bent as they travel over many bumps and dips in the potential felt by the electrons in the 2DEG. These bumps and dips come from the ionized Si donor atoms located 22 nm above the 2DEG and also from impurities and defects located throughout the heterostructure. The size of the fluctuations in the potential is small relative to the Fermi Energy of the electrons. As mentioned in Section 5.3 and plotted in Figure 5.4a, calculations by Rick Heller s group have yielded potentials with ripples on the order 10% E_F. So these branches are not due to direct guiding of flow by corrugations in the potential as a valley might guide a river. Rather, the key to the formation of the branches lies in what happens as electrons pass over dips in the potential. As the electron trajectories pass over dips in the potential they are focused and two caustics appear downstream of the dip. These caustics are the reason for the observed branching behavior. They are stable features in the flow from that point on and remain narrow precisely because they are caustics.

The origin of these caustics can be illuminated by focussing on what happens in a particularly simple system shown below in Figure 5.5. In this system classical electron trajectories exit from a point contact at the far left (shown in Figure 5.5a) and pass over a single focussing potential dip downstream from the QPC (a potential plot of this focussing dip is shown in Figure 5.5b).

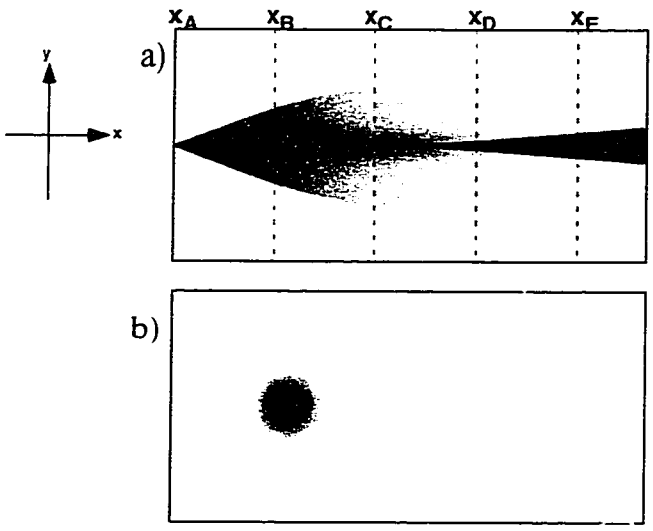

Figure 5.5 Classical electrons trajectories pass over a single focusing dip in the potential landscape. This is all that is needed for the formation of two caustics (infinitely thin lines of infinite trajectory density).

The origin of the caustics can be better understood by examining the time evolution of the trajectories in an appropriate subset of their 4-d phase space $(x(t),y(t),p_x(t),p_y(t))$. In Figure 5.6a-e we show five slices at different distances from the QPC of the electron trajectories' y-p_y phase space.

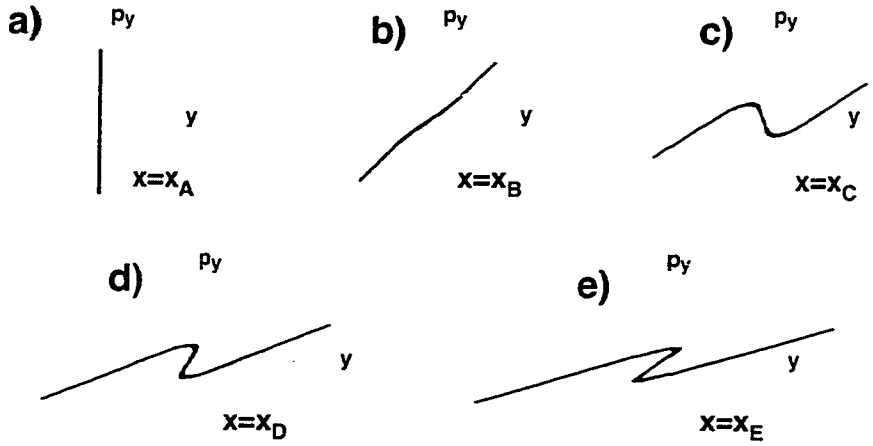

Figure 5.6 shows slices of the phase space evolution of the trajectories shown in Figure 5.5 at five different values of x. a) shows the initial distribution of trajectories, with all trajectories starting from y=0 with a spread in p_y. b) shows the trajectories as they pass over the potential dip. c) shows the trajectories after they have passed over the dip, but before they have actually formed two caustics. d) shows the onset of the two caustics. e) shows the caustics further downstream.

At position $x = x_A$ in Figure 5.5a, all the trajectories are at $y = 0$ with a wide spread in p_y (because of the roughly ±20° spread in their initial direction out of the QPC). Placing a point on the y-p_y phase space diagram in Figure 5.6a for each electron trajectory, we end up with what is shown- a line at $y = 0$ extending to $\pm p_{y0}$, the initial cutoff in the y momentum. If the electrons were traveling out over a perfectly flat potential, the time evolution of the phase space would simply be a tilting of this line, with trajectories with more positive p_y traveling to larger positive y values, and trajectories with more negative p_y traveling to larger negative y values.

Because the trajectories in this example are travelling over a dip in the potential, a very important difference emerges in their phase-space time evolution. At point x_B the electrons are travelling over the potential dip, and close to the $y = 0$ center line some of the trajectories are being drawn back towards the origin - focussed by the dip. At point x_C the electrons have passed over the dip, and some of the trajectories closest to the $y = 0$ line have actually been redirected, with the sign of their p_y reversed. At point x_D the two caustics have just formed, as trajectories that were focussed by the dip pass through the y=0 line. The reason for these caustics now becomes clear- they are folds in trajectory phase space, where for two specific y-values (the values at which the folds occur) there is an infinite density of trajectories. Point x_E illustrates the future time evolution of these caustics- they are stable features in the flow from this point downstream- precisely which trajectories make up the caustic will change slightly with x, but the double fold in phase space is a feature that will not "fade away" with distance from the QPC. The two key features of these caustics for our case are that they are formed by passing over dips in the

potential, and that once they are formed they are stable features of the flow from that point onwards.

The image to the right is a classical simulation of electron trajectories passing over a bumpy potential and illustrates what happens when instead of there being one focussing dip, there are many bumps and dips which the electrons pass over. A caustic traveling over a bumpy potential landscape is still a stable feature of the flow, so unless it hits precisely the right bump to "defocus" it, it will simply be bent and deflected by later bumps and dips. This can be seen in Figure 5.7, as numerous caustics can be seen to form, and then to be bent and deflected but not diffused as they propagate through the rest of the flow.

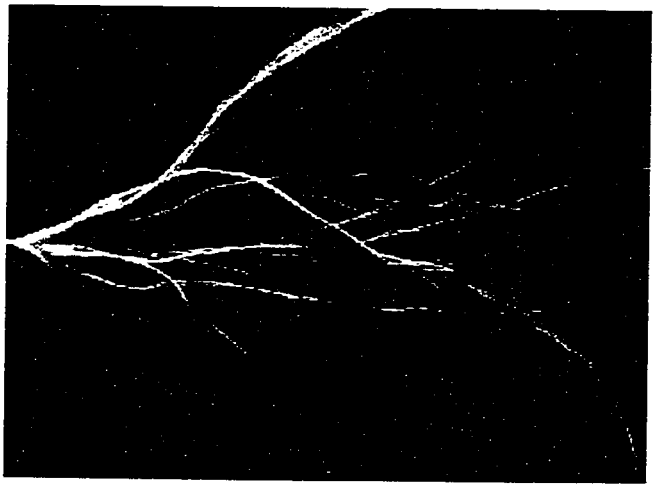

Figure 5.7 This figure shows a classical simulation of electrons passing over a bumpy potential. Many double caustics can be seen forming downstream from potential dips, and they are stable features of the flow from that point onwards.

There are several pieces of evidence which bolster the picture of caustic formation being centrally important to the observed branched flow. The images in Figure 5.8 illustrate one set of evidence- it is often possible to see what appear to be double caustics in our images of electron flow. This figure shows one image of electron flow that contains several examples of possible caustics. The top figure is free of any markings so as

to provide a clean reference scan to refer back to. Figures 5.8b through 5.8d show three specific places in this particular scan which seem to contain potential dips resulting in double caustics downstream from them.

Another observation that bolsters our theoretical understanding of the branch origins is that the branches of current we see in our images stay narrow for their entirety. It is not the case that the flow seems to narrows to a thin line at one point but then spreads out again to a widening fan downstream. This observation is in agreement with the behavior of caustics, which, while fading in intensity with distance, do not spread out.

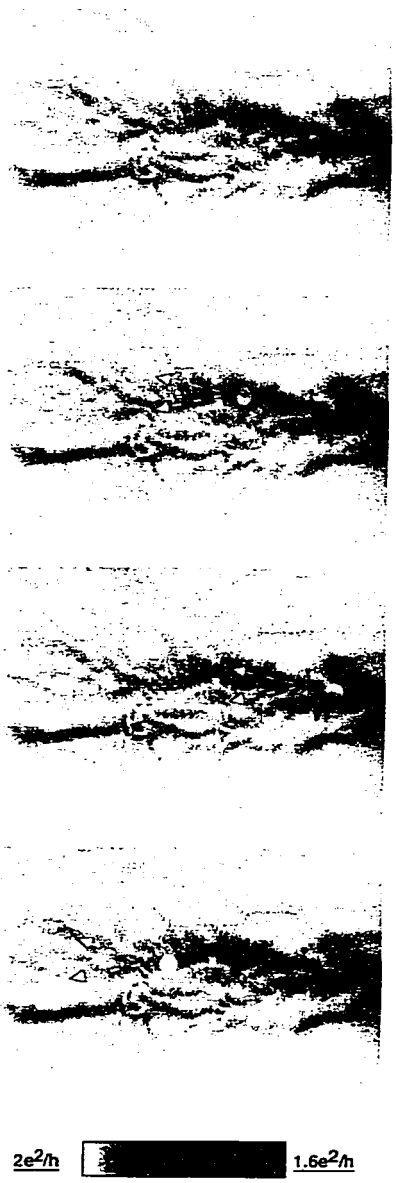

Figure 5.8 Several possible examples of caustics found in one current flow image. a) shows the image with no markings for easy reference. b), c), and d) show three examples of what might be the formation of caustics in the flow image. The two arrows denote the two arms of the caustic, and the light shaded circles represent possible potential dip locations

5.5 Branched Flow Statistics

The branches are an unpredicted feature in the electron flow through a 2DEG which were not understood before this series of measurements. A natural question to ask is: how does this new information fit in with the simpler, less complete picture of electron flow often used in the past?

Radial

A fundamental point in analyzing the statistical measures of the observed branching flow is the simple question: how does the observed signal fall of with distance from the QPC? A simple derivation for the expected average signal is shown below in Figure 5.9:

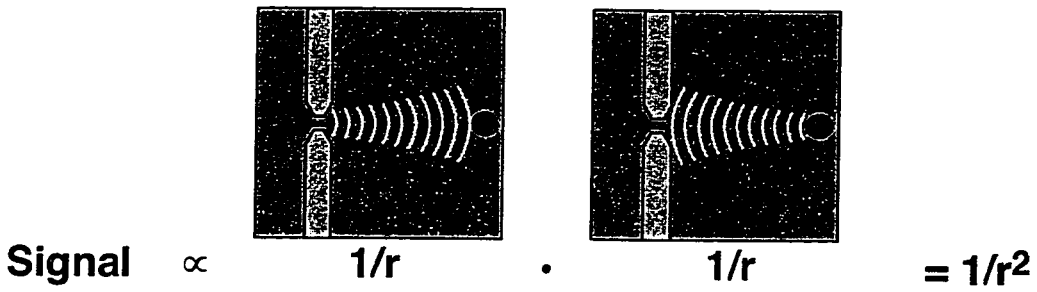

Figure 5.9 shows a simple model that predicts the average intensity of our measured signal to fall off as $1/r^2$. This picture is analogous to a 2-d version of the "radar problem". Here the signal falls of as 1/r on the trip out from the QPC. A small portion of that flux hits the tip and is reflected back towards the QPC. This backscattered flux then again falls off as 1/r. The total flux hitting the QPC, then is proportional to $1/r^2$. Finite mobility is expected to cause the actual signal to fall of at a slightly faster rate.

As shown in Figure 5.9, electrons travelling out from the QPC have a current density which falls off as 1/r. When part of that flow strikes the depletion region underneath the tip it is reflected in an outgoing circular wave back towards the QPC and this flux again

falls off as 1/r. The expected average signal is proportional to the amount of flux back-scattered from the tip through the QPC, and is therefore equal to the product of these two factors, $1/r^2$. Figure 5.10 shows the measured average signal as a function of radial distance from the QPC.

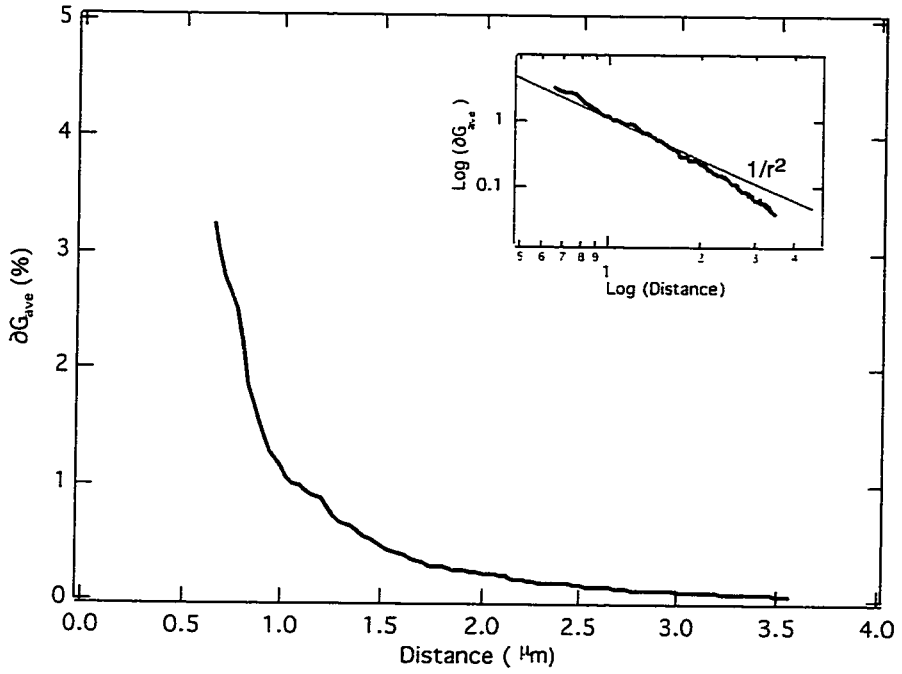

Figure 5.10 Shows the measured dependence of the average ΔG signal in a 20° cone in front of the QPC as a function of distance, r. The signal was averaged over four different QPC in an attempt to avoid any specific device dependencies. The measured falloff is quite close to $1/r^2$, as can be seen in the log-log plot in the inset.

Figure 5.10 confirms as expected that the average signal in our images falls off as $1/r^2$ with distance. The signal can be seen to fall of slightly faster than $1/r^2$ for the larger values of r. One possible source for this increased falloff is the finite mean free path of the sample, although more work, both theoretical and experimental, needs to be done to explore this further.

5.6 Persistent Coherent Fringe

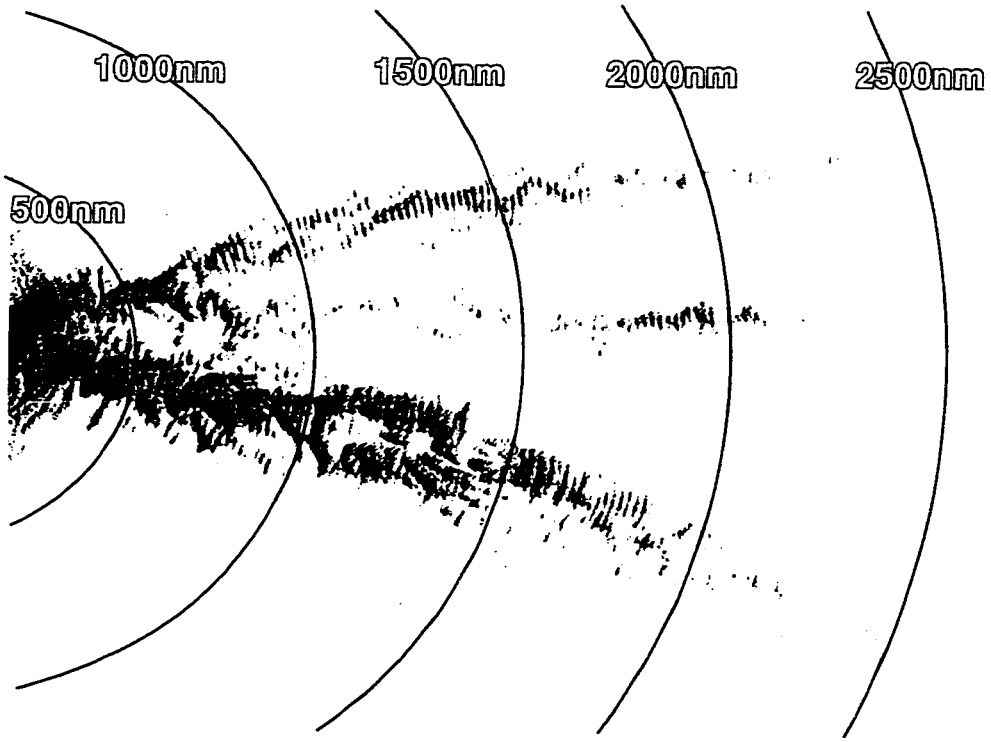

Figure 5.11 shows a details view of electron flow from a QPC emphasizing the coherent fringes spaced by $\lambda_F/2$ which are visible out to the edge of the scan range.

This section documents the survival of the $\lambda_F/2$ fringes which decorate our images throughout the entire scan range, up to distances from the QPC of 4μm and greater. The survival of these fringes is especially interesting because if the only mechanism for the coherent fringes was the one given in Section 4.2 (for the $\lambda_F/2$ fringes seen very close to the QPC), then the fringes would begin to be attenuated exponentially beyond a characteristic length, l_{th} = 650nm at 1.7K. The measured relative amplitude of these decorative fringes is shown n Figure 5.12.

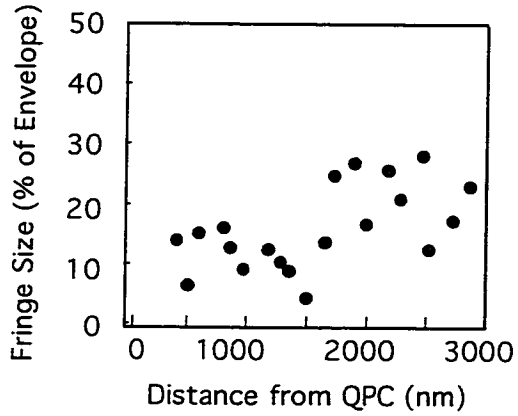

Figure 5.12 shows the measured relative fringe amplitude as a function of distance from the QPC. The relative amplitude is defined as the peak to peak distance over the max. Thus if the fringes were as large as the current envelope, their "relative amplitude" would be 100%. Fringes were measured from the image in Figure 5.11.

What is clear from this figure is that the fringes are not decreasing in relative intensity, and in fact seem to be growing slightly. The fact that the fringes survive past the thermal length is important, and mean that it might be possible in the future to use these fringes to measure aspects of phase coherence in 2DEG systems not easily accessible through transport measurements

5.7 Interesting or Unexpected Observations

Are Branches Fixed?

An additional question about the dramatic branching behavior seen in this chapter is the question of how fixed the locations of the branches are. How sensitive to small perturbations in the potential are the exact locations of the branches? This next measure-

ment investigates this question by moving the location of the center of the QPC channel slightly, and noting the effect on the branches downstream. Figure 5.13 shows the measured effects of this change. Moving the QPC channel was accomplished by putting unequal negative voltages on the two surface gates.

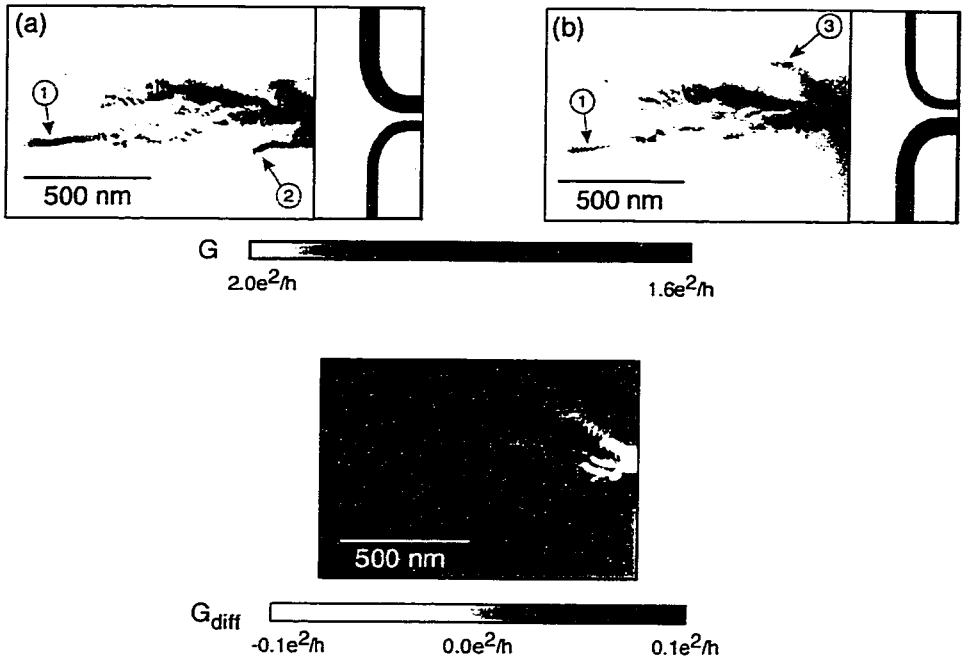

Figure 5.13 Images showing the center of the QPC channel being shifted up and down by using unequal gate voltages. (a) –0.3 Volts extra on the top gate, (b) –0.3 Volts extra on the bottom gate. The light gray areas indicate the outline of the QPC gates, while the darker gray regions show schematically the expected depletion regions underneath the gates. (c) Shows the difference between the scans in (a) and (b).

In Figure 5.13a there is -0.3 Volts more voltage on the top gate than on the bottom gate (note schematic depletion region size), which shifts the position of the QPC downward. Figure 5.13b has -0.3 Volts more on the bottom gate than the top, shifting the position of

the QPC upward. The current flow close to the QPC has also shifted upwards with branches appearing or becoming stronger in the top half of the image and branches disappearing or becoming weaker in the bottom half. Figure 5.13c shows Figure 5.13b subtracted from Figure 5.13a. We see that near the QPC the main change in flow is that the flow has shifted- less current flows in some branches and more flows in others (see arrows #2 and #3). However, farther away from the QPC, the branches themselves begin to move in unpredictable ways from the randomizing effect of passing over many bumps and dips. Arrow #1 points to a particular branch which appears to be pivoting downwards from 5.13a to 5.13b as the QPC channel is moved upwards. Directly above the circled #1 another branch can be seen possibly also pivoting downwards as the QPC is effectively moving upwards. This general movement upwards near the QPC combined with pivoting action farther from the QPC can be seen in Figure 5.13c by noticing that the white areas (indicating increasing flow from moving the QPC channel upwards) are on top of each branch near the QPC, but are on the bottom of each branch at the left of the scan, far from the QPC.

No Backscattering Means No Plateau Suppression

This next measurement shows images of current flow through one particular QPC out of the many studied so far which is an extreme example but which illustrates an important point. In order for an impurity, defect, or donor inhomogeneity to have an effect on the conductance trace of a QPC, it must not only bend electron waves, but actually backscatter them back through the QPC. An interesting implication of this fact is that nice QPC plateaus do not always guarantee a correspondingly well behaved current pattern. Figure 5.14a shows the conductance plot at 1.7K for one of the QPCs studied; each of the bottom five plateaus are quite close to the ideal values of N * $2e^2/h$. Figure 5.14b shows the measured current pattern for the QPC on the $G=6e^2/h$ conductance step. It appears in this case that there is a strong impurity located directly in front of the QPC. The perturbation from this impurity is either not quite strong enough or it is placed slightly off to the side of a main lobe of current, and instead of

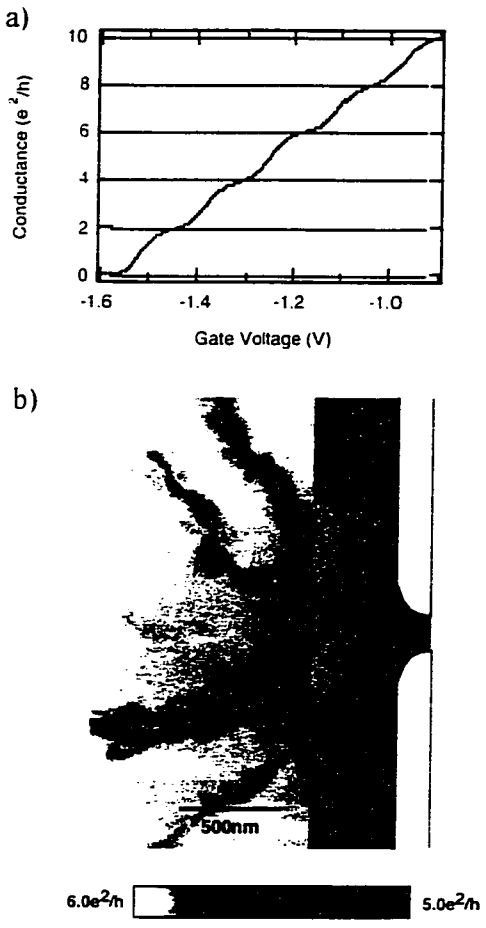

Figure 5.14. A surprising example of how an impurity must not only deflect, but backscatter a mode in order to affect it's transmission coefficient (and hence conductivity). a) shows the QPC conductance vs. Vgate plot with nicely quantized plateaus. b) shows the current at $G=4e^2/h$, which displays a surprisingly violent deflection of current upwards, presumably by a strong impurity.

backscattering that current in that branch back to the QPC, it only deflects the current strongly upwards.

As mention above, this QPC is an extreme example, but it is an important case nonetheless. It clearly demonstrates the concept that in order for an impurity (or a tip perturbation!) to affect the quantization of a plateau, it is not enough for it simply to strongly deflect the electrons flowing in that corresponding wave function; it must actually backscatter electrons through the QPC.

Chapter 6

Conclusions and Future Directions

6.1 Summary

This thesis has presented the results of developing new methods for directly imaging the coherent flow of electrons in two dimensional electron gas (2DEGs) nanostructures. 2DEGs have been the subject of an enormous number of ground-breaking experiments over the past two decades, but one thing that has been difficult to achieve has been the ability to correlate transport measurements with detailed information about the spatial flow of electrons through 2DEG devices. We have achieved this goal by using a low temperature scanned probe microscope in conjunction with low noise transport measurements[1,2,3]. The ability to collect spatial information in addition to the usual low-noise transport measurements on mesoscopic samples is a powerful new tool, and opens up many interesting and potentially important areas of research.

Chapters 2 presented the many experimental techniques and advances that were developed or improved in the course of this work. Particularly important to achieving these results has been coming up with a working procedure to reliably align the AFM and sample at both room-temperature and liquid-Helium temperatures (in Section 2.5), successfully cooling and shielding the sample at 1.7K (and , both in Section 2.3 Cryogenics), designing advanced electronics and software to simultaneously control and

---

1.M. A. Topinka, et al., "Imaging Coherent Electron Flow from a Quantum Point Contact," *Science* **289**, 2323-2326 (2000)

2.M. A. Topinka, et al., "Coherent branched flow in a two-dimensional electron gas," *Nature* **410**, 183 (2001)

3.M. A. Topinka, et al., "Imaging Coherent Electron Wave Flow in a Two-Dimensional Electron Gas", in press, Physica E (2002).

monitor both the AFM and the sample at relatively high speeds and low noise (Section 2.6 Electronics and 2.7 Control Software Overview), and identifying and solving the conducting tip problem (" Making a tip conduct electrically" on page 27 in Section 2.5 Advanced AFM Techniques).

Chapter 3 discussed the understanding we have developed of how our imaging techniques work. In this chapter we presented calculations and measurements which show that one very critical element of being able to image current is creating a backscattering depletion disc underneath the tip. Interesting things were learned both about the apparatus and technique (Sections 3.2 and 3.3) and about quantum point contacts (Section 3.4) by only weakly coupling the tip to the 2DEG and creating a perturbation that lenses and bends electron trajectories but does not backscatter them. By coupling the tip strongly to the 2DEG, however, and creating a depletion disc which could backscatter electrons through the QPC we showed we could directly image electron flow (Section 3.5).

Chapter 4 showed the first published series of spatial images showing coherent electron flow from a quantum point contact. Images of electron flow on different conductance plateaus were presented which agreed very well with theoretical predictions (Section 4.2). These raw images were then separated out into their constituent modes (Section 4.4), where the relationship between the mode number and number of lobes was confirmed in both theory and experiment. The appearance of coherent fringes spaced by $\lambda_F/2$ which decorate our images of flow was discussed in Section 4.3. Last, a different mode of operation which allows us to use the AFM to place a positionable artificial impurity at any point in the 2DEG near the QPC was discussed and conductance mea-

surements showing the selective scattering of individual modes from this artificial impurity were presented (Section 4.5).

In Chapter 5 we presented images over a much broader area than those presented in Chapter 4. These images show the electron flow forming striking and unexpected narrow branches at distances greater than about 500nm (Section 5.2). In Sections 5.3 and 5.4 we presented the latest understanding of the origins of this flow, which is that they are due to the formation of caustics from the cumulative effects of passing over many small bumps and dips in the potential. The bumps and dips are from impurities, and donor atoms, and are what give a 2DEG its finite mean free path. These branches are not simply due to deep "river valleys" through which the electrons flow in the 2DEG, but rather are dynamic channels which are sensitive to the indirect cumulative effect of many small angle scattering events along each electron's trajectory. This branching flow is an important aspect of electron flow in 2DEG nanostructures which was not known before the completion of these experiments. It is consistent with but not predicted by such statistical measures as mean free path and diffusion constants.

6.2 Future Directions

The work in this thesis has resulted in the creation of an exciting new tool with which to study two-dimensional electron gas nanostructures. The work with understanding our imaging technique (Chapter 3) and the images confirming theoretical expectations for the flow patterns through the modes of QPCs (Chapter 4) presented in this thesis have demonstrated that this new tool works very well. At this point there are

many intriguing possible future areas of research which would be exciting to explore using these techniques.

One possible future direction is to further investigate aspects of the branching of electron flow discovered and presented in Chapter 5. What occurs as the mean free path is decreased, (leading to more diffusive flow), or the electron sheet density in the 2DEG is lowered (causing a corresponding increase in electron-electron interactions, or even viscosity?) Do these channels persist out into the diffusive flow regime? Our current understanding of the dynamics indicates that the persistence of these channels can be understood in terms of classical dynamics, and that catastrophe theory, with it's abruptly forming phase-space caustics, plays a part in their formation. It would be interesting to investigate these caustics further in terms of their effect on quantum mechanical phase and their stability against slight perturbations.

Another promising direction of research is aimed at the detailed measurement and manipulation of electron spins in 2DEGs. An extremely active area of research in 2DEGs in the past few years has been the creation of sources of spin polarized electrons in 2DEGs, and the preliminary investigation of possible implementations of "spintronics", the use of spin instead of charge as a carrier of information in electronic circuits. An extension of our current imaging method could prove to be a valuable tool in working towards this goal. It may be possible to create a movable and tunable magnetic scatterer (i.e. a scanning nano-Stern-Gerlach apparatus) by coating the tip with a soft magnetic material (such as Permalloy) and applying an adjustable uniform magnetic field. By scanning the tip above a polarized beam of electrons (emitted from, for instance, a point contact bordering a region of highly spin polarized electron gas), the

spin lifetime and coherence time could be directly imaged. Beams of similarly or oppositely polarized electrons could be made to cross in directly imaged areas, and the effects of interactions between these electrons on flow could be spatially measured. What are the dominant spin-flip mechanisms in such interactions? Would oppositely polarized beams of electrons scatter off of each other less than identically polarized beams? Interference patterns involving both spatial and spin degrees of freedom of electrons could also be investigated- an area previously difficult to probe because of the lack of a good spatial imaging technique.

There is also the exciting possibility of extending our current technique for imaging envelopes of wavefunctions' flow through a QPC to imaging eigenstates in a quantum dot. A number of interesting investigations could result from the ability to spatially resolve wavefunction shapes inside a quantum dot. For instance, one could investigate recent evidence, which seems to show that the addition spectrum of laterally confined dots consists of alternating spin states, (similar to Hund's rule) causing an alternating total spin of the dot. What effect does this have on the spin states of the electron beams emanating into and out of the dot? What are the correlations and symmetries in the many-body wavefunction of the N electrons inside the dot? (where N can be varied anywhere from tens to thousands of electrons).

The development of this powerful new imaging technique opens up many interesting research possibilities: investigating the underlying dynamics of electron flow in 2DEGs, spatially imaging electron wave decoherence (a controversial issues in 2DEGs and metals recently), researching 2DEG spin physics and possible implementations of spintronics, mapping out many-body wavefunctions in quantum dots, and perhaps even

exploring ideas for solid state quantum computation. I look forward to seeing what directions Bob, Brian, Ania, Kathy, and other future group members decide to take this exciting project.

Appendix A

Perturbation To 2DEG From a Point Charge

A.1 Perturbation in 2DEG from the Tip as a Point Charge, Q

The basic problem to be solved is illustrated in Figure A.1. Here d can only be positive (to roughly model the effect of the AFM tip on our 2DEG). Negative d (to model the effect of a Si dopant on the 2DEG) requires a different placement of image charges. This problem can be solved by a clever application of the image charge method. The following arrangement of image charges (Figure A.1) will be used to give the exact analytic solution in this more complicated case:

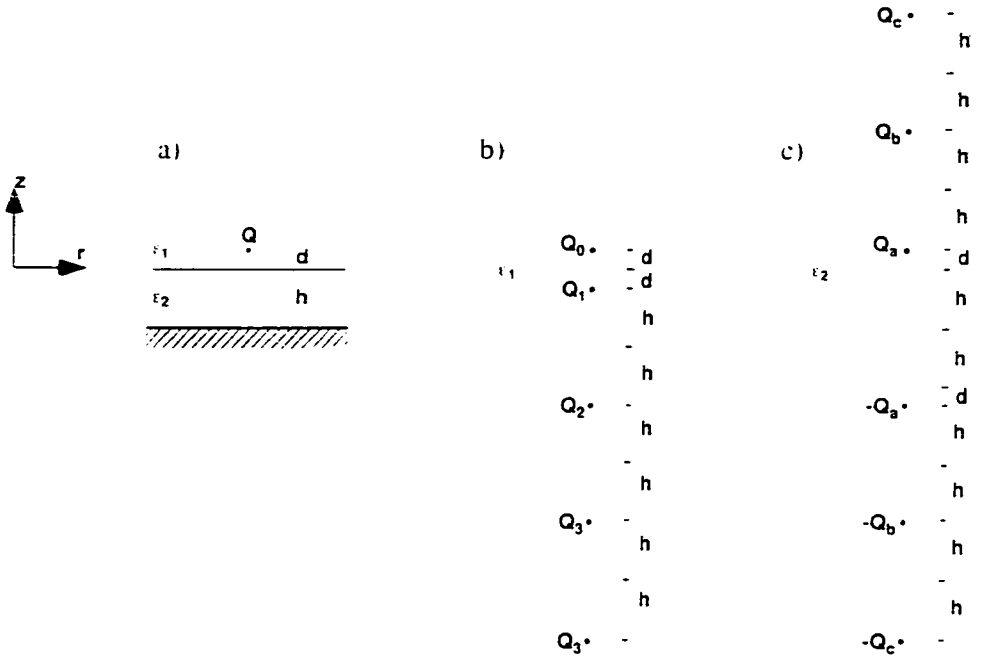

Figure A.1 a) shows the physical problem to be solved: a point charge Q located d above a dielectric interface with a ground plane (the 2DEG) distance h beneath. b) and c) show the series of images charges that will be used in Regions I and II. respectively.

Figure A.1b shows the series of charges that gives an appropriate form for the electrostatic potential in region I. The values of Q_0, Q_1, ... must be determined based on boundary conditions at z=0 (the dielectric interface). A.1c shows the series of charges for region II. Here the boundary conditions at z=-h have already been used to identify charges pairs, Q_a and $-Q_a$, Q_b and $-Q_b$, etc. The values for Q_a, Q_b,... must be solved again based on the boundary conditions at z=0

The fact that this is the proper arrangement of charges will be shown once it is demonstrated that it is possible to choose values of Q_0,Q_1,.... and Q_a,Q_b,... that cause Poisson's Equation to be satisfied in both Region I and Region II and that also cause all boundary conditions on the borders of Region I and Region II to be met. Continuing with the derivation, the potential inside of Regions I and II can be written down simply as

In Region I (inside dielectric ε_1)

Eq. A.1
$$\Phi(r,\theta,z\geq 0)=\frac{k}{\varepsilon_1}\left[\frac{Q_0}{\sqrt{r^2+(z-d)^2}}+\frac{Q_1}{\sqrt{r^2+(z+d)^2}}+\frac{Q_2}{\sqrt{r^2+(z+(2h+d))^2}}+\frac{Q_3}{\sqrt{r^2+(z-(4h+d))^2}}+\ldots\right]$$

In Region II (inside dielectric ε_2)

Eq. A.2
$$\Phi(r,\theta,-h\leq z\leq 0)=\frac{k}{\varepsilon_2}\left[\frac{Q_a}{\sqrt{r^2+(z-d)^2}}-\frac{Q_a}{\sqrt{r^2+(z+(2h+d))^2}}+\frac{Q_b}{\sqrt{r^2+(z+(2h-d))^2}}-\frac{Q_b}{\sqrt{r^2+(z+(4h-d))^2}}+\frac{Q_c}{\sqrt{r^2+(z+(4h+d))^2}}-\ldots\right]$$

First of all, we can observe immediately that $Q_0 = Q$, because this is the only choice of Q_0 which can give the proper potential in Region I. Next, in order to determine the values of $Q_1, Q_2, \ldots$ and $Q_a, Q_b, \ldots$ we must apply the boundary conditions for the dielectric interface ($z=0$). Across a dielectric interface at $z=0$ (see Figure A.1) the parallel electric field must satisfy the relationship $\varepsilon_1 E_{\parallel}|_{z=0+} = \varepsilon_2 E_{\parallel}|_{z=0-}$ and the perpendicular electric field must be continuous, $E_{\perp}|_{z=0+} = E_{\perp}|_{z=0-}$

Applying the boundary condition $\varepsilon_1 E_{\parallel}|_{z=0+} = \varepsilon_2 E_{\parallel}|_{z=0-}$

Eq. A.3

$$-Q_0 (r^2 + d^2)^{-3/2} d + Q_1 (r^2 + d^2)^{-3/2} d + Q_2 (r^2 + (2h + d)^2)^{-3/2} (2h + d) + Q_3 (r^2 + (4h + d)^2)^{-3/2} (4h + d) + \ldots$$

$$= -Q_a (r^2 + d^2)^{-3/2} d - Q_a (r^2 + (2h + d)^2)^{-3/2} (2h + d) - Q_b (r^2 + (2h + d)^2)^{-3/2} (2h + d) - Q_c (r^2 + (4h + d)^2)^{-3/2} (4h + d) - Q_c (r^2 + (4h + d)^2)^{-3/2} (4h + d) - \ldots$$

Because this must be true for all r, we can match the (r^2+d^2) terms, the $r^2+(2h+d)^2$ terms, and so on, to give us a series of equations...

Eq. A.4 $\quad Q_0 + Q_1 = -Q_a \qquad Q_2 = -Q_a - Q_b \qquad Q_3 = -Q_b - Q_c \ldots$

Likewise applying the boundary condition $E_{\perp}|_{z=0+} = E_{\perp}|_{z=0-}$ yields...

Eq. A.5

$$\frac{1}{\varepsilon_1}\left(Q_0(r^2+d^2)^{-3/2} + Q_1(r^2+d^2)^{-3/2} + Q_2(r^2+(2h+d)^2)^{-3/2} + Q_3(r^2+(4h+d)^2)^{-3/2} + \ldots\right) = \frac{1}{\varepsilon_2}\left(Q_a(r^2+d^2)^{-3/2} - Q_a(r^2+(2h+d)^2)^{-3/2} + Q_b(r^2+(2h+d)^2)^{-3/2} - Q_b(r^2+(4h+d)^2)^{-3/2} + Q_c(r^2+(4h+d)^2)^{-3/2} + \ldots\right)$$

And again, because this must be true for all r, we can match the (r^2+d^2) terms, the $r^2+(2h+d)^2$ terms, and so on, to give us a series of equations...

Eq. A.6

$$\frac{Q_0 + Q_1}{\varepsilon_1} = \frac{Q_a}{\varepsilon_2} \qquad \frac{Q_2}{\varepsilon_1} = \frac{-Q_a + Q_b}{\varepsilon_2} \qquad \frac{Q_3}{\varepsilon_1} = \frac{-Q_b + Q_c}{\varepsilon_2} \qquad \ldots$$

Combining Eqs. A.5 and A.6 we finally have our desired relations for $Q_0, Q_1, Q_2, \ldots$ and $Q_a, Q_b, \ldots$ For the solution of Φ in Region I we have...

Eq. A.7

$$Q_0 = Q$$

Eq. A.8

$$Q_1 = \left(\frac{\varepsilon_1 - \varepsilon_2}{\varepsilon_1 + \varepsilon_2}\right)Q_0 \qquad Q_2 = \left(\frac{\varepsilon_1 - \varepsilon_2}{\varepsilon_1 + \varepsilon_2}\right)Q_1$$

And likewise for the solution of Φ in Region II we have...

Eq. A.9 $$Q_a = \left(\frac{2\varepsilon_2}{\varepsilon_1+\varepsilon_2}\right)Q$$

Eq. A.10 $$Q_b = \left(\frac{\varepsilon_1-\varepsilon_2}{\varepsilon_1+\varepsilon_2}\right)Q_a \qquad Q_c = \left(\frac{\varepsilon_1-\varepsilon_2}{\varepsilon_1+\varepsilon_2}\right)Q_b$$

Using the fact that the induced charge on a conducting surface is $\sigma = \varepsilon E_{\perp}$ we can now write the induced charge on the metal surface beneath the charge, Q...

$$\sigma(r) = \varepsilon \frac{\partial}{\partial z}\Phi(r,\theta,z)\Big|_{z=-h}$$

Eq. A.11
$$= \varepsilon_2 \frac{\partial}{\partial z}\left[\frac{k}{\varepsilon_2}\left[\frac{Q_a}{\sqrt{r^2+(z-d)^2}} - \frac{Q_a}{\sqrt{r^2+(z+(2h+d))^2}} + \frac{Q_b}{\sqrt{r^2+(z+(2h+d))^2}} - \right.\right.$$
$$\left.\left.\frac{Q_b}{\sqrt{r^2+(z+(4h+d))^2}} + \frac{Q_c}{\sqrt{r^2+(z+(4h+d))^2}} - \ldots\right]\right]\Bigg|_{z=-h}$$

Appendix B

AFM Procedure Details

Upon First Cooling Down

The first thing to do once liquid-He and liquid-N have been added to the dewar and the temperature of the apparatus has stabilized (usually about an hour after the liquid-He is added), is to take a feedback contact mode scan to find out if we successfully aligned the apparatus as room-T so that the device of interest is now within the scan-range of the piezotube. Often this takes a bit of sleuthing to find an alignment marker and to calculate the distance to the device.

Assuming the device is within reach, the next step is to apply whatever offset high voltages are necessary to bring the tube within range of the +/-200V high-voltage op-amps. Often simply applying +/-200V to the X and Y quadrants of the piezotube is not sufficient to bring the tip to the sample. The solution we have arrived at for this which essentially more than doubles our scan range at low-T is to add the outputs of Kepco 325-0.8M power supplies to the outputs of our hi-voltage op-amps. By using four of these power supplies (one for each quadrant of the piezotube) any voltage between +500V and -500V can be applied to each of the quadrants[1]. This usually results in an expansion of the scan distance from about +/-7μm to about +/-18μm. This improvement is critical to being able to successfully align over the device, since it essentially means a 10-fold

1. This should probably not be done at room-T, since there is some chance of arcing between adjacent electrodes for such high voltages in ambient conditions.

improvement in the scan area and hence a 10-fold improvement in the chance to "hit" the device on each cooldown!

Correcting for Surface Tilt

Before precisely locating the device it is necessary to correct for misalignment between the scan plane and the plane of the surface. Both because of piezotube non-idealities and because of imperfect flatness of the sample and sample holder, the scan plane is almost never perfectly aligned with the plane of the surface. It is important to correct for this if "hover-mode" (the scanning mode used to image electron flow) is to be used. Figure B.1 shows the incorrect and correct scan planes.

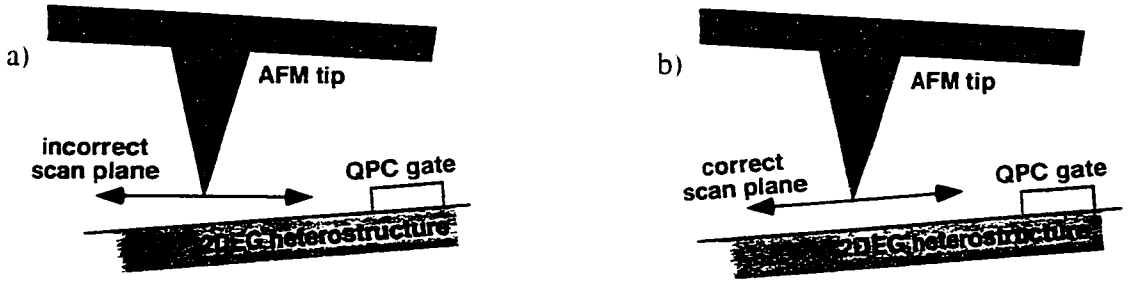

Figure B.1 shows the scan plane adjustment which must be made to compensate for the essentially inevitable tilt in the surface plane relative to the unadjusted scan plane. a) shows the incorrect (unadjusted) scan plane, where the tip-surface height changes with X-Y position. b) shows the correct scan plane, where an (X,Y) dependent voltage has been added to the Z-voltage and the tip-surface height is now constant and independent of X-Y location.

There are two adjustable potentiometers on the X-Y-Z low-voltage electronics which allow a variable slope plane to be added to the Z output voltage which depends on the X and Y voltages. Finding the correct settings for these potentiometers (and hence, the right X & Y slope) is usually the first adjustment that must be made in preparing to take data. The procedure for accomplishing this is fairly straightforward- topography

scans (typically with feedback ON) are taken repeatedly while adjusting the X&Y tilt-potentiometers until the scans appear flat. It is often helpful to have the audio feedback on when performing the rough flattening, because when the potentiometer is set correctly there will be no difference in pitch between the "scanout" and the "scanback". It is also useful to switch the "fast" scan axis between X and Y while performing this flattening to speed up the process. Make sure that "scan rotation" in the AFM program is off while performing flattening.

Precisely locating the device

After the surface plane has been properly set-up, we can begin to precisely locate the device. It is important that the tip not contact the GaAs surface in the immediate vicinity of the device, so simply performing feedback contact-mode scans until we precisely locate the device will not work. Instead, we locate the device with successively more precise, non-destructive methods. First we scan the tip far above the surface and look for an electrical signal indicating the tip is over the device. In the scan below (Figure B.2a), we have energized the QPC, and are scanning the tip far above the surface (about 50nm). From the scan we can guess the locations of the gates (shown as black dashed outlines).

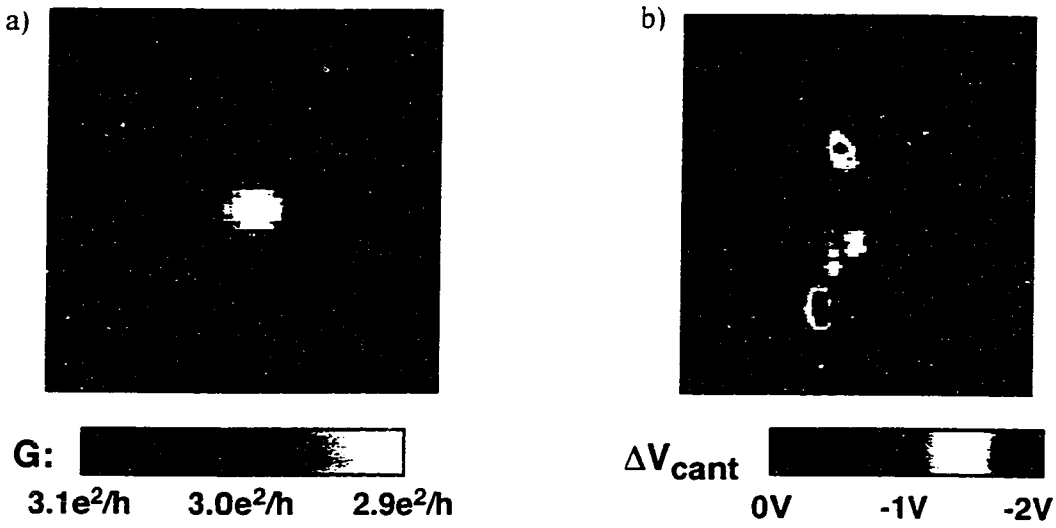

Figure B.2 shows the final steps in precisely determining the location of the QPC. a) shows an electrical scan taken 50nm off the surface with Vtip=-1V. b) shows a no-feedback contact mode scan taken with gates and tip grounded at a height of 25nm above the GaAs surface. The rough edges of the gate (perhaps from imperfect lift-off) which stick up further than the rest of the gate can be seen. The values plotted here is the voltage straight from the cantilever bridge circuit, and correspond to tip deflection.

The next step (see Figure B.2b) is to more precisely identify the location of the device so that we can later register the electrical scans precisely to the surface gate topography. This is done by grounding the gates and tip, and slowly bringing the tip closer to the surface, taking fixed height scans with the feedback turned off[2] until the tip barely skims the tops of the gates. Glancing contact between a grounded tip and grounded gates does not seem to hysteretically affect the device in any way.

2.With a recent improvement to the feedback box, it is now possible to take feedback scans at a fixed minimum separation from the distance.

Now that we now the precise location of the device, we choose an area we wish to scan. We then invoke the 'autoflatten' command from the script to more precisely identify the plane and location of the surface. This second more precise identification for the surface tilt is necessary because even a couple of nm of difference in tip height from one side of the scan to the other could potentially have significant effects on the strength of the observed signal. The 'autoflatten' command uses the routine described in Section 2.5 on page 36 to find the surface at N different points (X,Y locations passed to the command) and fits the best possible plane to those N points, throwing out the points highest above and furthest below the plane.

Characterizing The Device

The final step before actually taking an electron flow image is to take a conductance vs. gate voltage trace with all the settings (bias voltage, temperature, lock-in frequency, etc.) exactly as we plan to have them during the imaging measurements. If we plan on using a more exotic experimental setup (a finite bias DC measurement, for instance), it is of course important to characterize the device both in the simple mode described above as well as with the more complicated measurement setup.

At this point we are ready to begin taking data and imaging electron flow.